Photophysics and applications of organic semiconductors

Giulia Tregnago

London Centre for Nanotechnology

and Department of Physics and Astronomy

UCL

A dissertation submitted for the degree of Doctor of Philosophy

April 2015

I, Giulia Tregnago, confirm that the work presented in this thesis is my own. Where information has been derived from other sources and work which has formed part of jointly-authored publications has been used I confirm that this has been indicated in the thesis.

To the memory of my grandfather

To my family

To Umberto

Acknowledgments

My research was funded by the European Commission Seventh Framework Program (FP7/2007-2013) Marie Curie Initial Training Network under Grant Agreement No. 264694 (GENIUS).

First and foremost I want to thank my supervisor Prof. Franco Cacialli for inspiration and guidance. I would also like to express my gratitude to Prof. Neal Skipper, my secondary supervisor, for his support and to all the collaborators that made this project possible. In particular, a special thanks goes to Dr. Oliver Fenwick, Dr. Christopher Salzmann, Dr. Aurica Farcas, Dr. Timothy Steckler, Prof. Mats Andersson, Prof. Aurelio Mateo-Alonso, Dr. Hugo Bronstein, Prof. Vincenzo Palermo, Prof. Xinliang Feng, Dr. Karl Börjesson, Prof. Kasper Moth-Poulsen, Dr. Micheal Wykes, Prof. David Beljonne, Dr. Liisa Hirvonen, Prof. Klaus Suhling and all the people involved in the GENIUS project.

Finally, I would like to acknowledge past and present members of the Organic Semiconductors and Nanostructures group for the good time I had at UCL and the GENIUS fellows for the nice get-togethers.

Abstract

The work presented in this thesis is motivated by the great commercial impact of organic semiconductors especially in optoelectronics. In particular, we focus our attention on some of the current challenges in organic light-emitting diodes from the point of view of the photophysical properties of materials (i.e. via steady-state and time-resolved photoluminescence characterization) and the device physics.

In view of the interest in near-infrared emission, we propose two ways to obtain emission at long wavelength. Firstly, we report a new molecular design of one of the currently best performing polymer for near-infrared light-emitting diodes. We investigate the substitution of sulphur with selenium and find that it is more effective both in terms of photo- and electro-luminescence efficiency than by exploiting higher sulphur-chromophore loadings, while achieving a more important red-shift. Secondly, we explore the tuning of the energy gap through a careful choice of the relative positions of the frontier levels of two organic semiconductors. Following this strategy, we obtain a nearly pure near-infrared electroluminescence with essentially no emission from the single components at any operational voltage. We believe that results obtained are a valuable feedback as they suggest materials design criteria.

Given to the potential of phosphorescent materials for obtaining high efficiency OLEDs, we also consider the investigation of a novel emitter based on a wide-gap host co-polymerized with a low-gap phosphorescent emitter for efficient energy transfer.

Finally, we report a detailed investigation of the photoluminescence emission at low temperature of the fullerene derivative [6,6]-phenyl-C_{61}-butyric acid methyl ester (PCBM), widely employed as an electron acceptor in organic solar cells. Owing to the

availability of solvent-free single-crystals, whose growth has been recently reported by our group, we are able to investigate PCBM optical properties without solvent dependence. Our attempt is to provide significant information on the ordering and relative importance of the relevant excited states in PCBM.

Contents

List of Figures

List of Tables

List of Abbreviations

BHJ	Bulk heterojunction
CCD	Charge-coupled device
CT	Charge transfer
DAD	Donor acceptor donor
EET	Electronic energy transfer
EL	Electroluminescence
EQE	External quantum efficiency
ETL	Electron transport layer
FC	Franck Condon
FLIM	Fluorescence lifetime imaging microscope
FRET	Förster resonance energy transfer
HATNA	Hexaazatrinaphthylene
HOMO	Highest occupied molecular orbital
HT	Herzberg Teller
HTL	Hole transport layer
IRF	Instrument response function

ITO	Indium tin oxide
JLV	current density-luminance-voltage
JT	Jahn Teller
LUMO	Lowest unoccupied molecular orbital
MEH-PPV	2-methoxy-5-(20-ethylhexyloxy)-1,4-phenylene vinylene
MMP-Pt	Dimesityl diphenyl porphyryin platinium
NIR	Near infrared
OLED	Organic light-emitting diode
OPV	Organic photovoltaic
P3HT	poly(3-hexylthiophene-2,5-diyl)
PEDOT:PSS	Poly(3,4-ethylenedioxythiophene)-poly(styrenesulfonate)
PFO	poly(9,9-di-n-octylfluorenyl-2,7-diyl)
PL	Photoluminescence
PLED	Polymer light-emitting diode
PPV	poly(*p*-phenylene vinylene)
rpm	rounds per minute
SCLC	Space charge limited current
TCSPC	Time-correlated single-photon counting
TFB	Poly(9,9-dioctylfluorene-alt-N-(4-butylphenyl)diphenylamine)

List of publications

Publications included in the thesis

Part of the work presented in this thesis have been published or submitted for publication by the author:

- "Thia- and selena-diazole containing polymers for near-infrared light-emitting diodes"
  G. Tregnago, T. T. Steckler, O. Fenwick, M. R. Andersson, and F. Cacialli. *Journal of Materials Chemistry C* 3, (2015), 2792-2797

- "Virtually-pure near-infrared electroluminescence from exciplexes at polyfluorene/hexaazatrinaphthylene interfaces"
  G. Tregnago, C. Fléchon, S. Choudhary, C. Gozalvez, A. Mateo-Alonso, and F. Cacialli. *Applied Physics Letters* 105, no. 14 (2014): 143304

- "Deep-red electrophosphorescence from a Platinum(II)-porphyrin complex copolymerized with polyfluorene for efficient energy transfer – PF-MPP(Pt)"
  D. Freeman*, G. Tregnago*, S. Araguas Rodriguez, F. Cacialli, and H. Bronstein. *Submitted* - *Co-first authorship

- "Low-temperature photoluminescence spectroscopy of solvent-free PCBM single-crystals"
  G. Tregnago, M. Wykes, G. Paternó, D. Beljonne, and F. Cacialli. *Submitted*

Other publications

- "Geometric and Electronic Structures of Boron(III)-Cored Dyes Tailored by Incorporation of Heteroatoms into Ligands"
  L. Sun, F. Zhang, F. Qiu, M. Xue, G. Tregnago, F. Cacialli, S. Osella, D. Beljonne, X. Feng. *Chemistry – An Asian Journal* 10, no. 3 (2015), 709-714

- "Effect of permodified β-cyclodextrin on the photophysical properties of poly [2,7(9, 9 dioctylfluorene)-*alt*-(5, 5bithiophene)] main chain polyrotaxanes."
  A. Farcas, G. Tregnago, A. M. Resmerita, S. T. Dehkordi, S. Cantin, F. Goubard, P. H.i Aubert, and F. Cacialli. *Journal of Polymer Science Part A: Polymer Chemistry* 52, no. 4 (2014): 460-471.

- "Two dimensional array of photoluminescent light sources by selective integration of conjugated luminescent polymers into three dimensional silicon microstructures."
  G. Polito, S. Surdo, V. Robbiano, G. Tregnago, F. Cacialli, and G. Barillaro. *Advanced Optical Materials* 1, no. 12 (2013): 894-898.

- "Straightforward access to diketopyrrolopyrrole (DPP) dimers."
  S. Stas, J. Y. Balandier, V. Lemaur, O. Fenwick, G. Tregnago, F. Quist, F. Cacialli, J. Cornil, and Y. H. Geerts. *Dyes and pigments* 97, no. 1 (2013): 198-208.

Introduction

Nowadays, organic semiconductors are of great commercial interest especially in the optoelectronic field [1, 2]. In particular, organic light-emitting diodes (OLEDs) based displays and lighting panels are already available on the market, and other technologies (i.e. solar cells, transistors) are close to the market entry [3]. Yet, there is still room for improvement both on device fabrication techniques for large-scale production and on design of each component. In particular, great efforts are currently made to obtain control on the emission wavelength (i.e from near-infrared emission to white OLEDs), optimize the interface between device components, maximize the power efficiency, extend device lifetime and stability, and exploit phosphorescent emitters, to name a few. In this respect, the investigation of photophysical properties of organic semiconductors provides important information to address many of these open problems by giving valuable insight into their properties at the molecular scale [4, 5].

The work presented herein focuses on various aspects of optical and electronic processes occurring in organic semiconductors. In particular, our interest is concentrated on photo- and electrical- excitations and the relaxation of electronic excited states involving a change of multiplicity, or intra- and inter-molecular interactions, or vibronic couplings between two electronic excited states. We also study charge and energy transfer between donor and acceptor systems. We mainly look into these processes by means of steady-state and time-resolved photoluminescence techniques and photoluminescence spectroscopy at cryogenic temperatures. In adidition, we evaluate materials properties when incorporated into a lab-scale OLED device. Information gathered is useful to interpret device operation, obtain a better understanding of the nature of the electronic

processes and also as a feedback for the design of new devices and materials.

Overview of the thesis

This thesis is divided into six chapters. The first two chapters give a general introduction on organic semiconductors and experimental techniques used, while various issues of general interest in optoelectronics are being addressed in the following chapters. Detailed descriptions of the content of each section are given as follows.

Chapter 1 provides an introduction to the basic concepts of optoelectronics. We begin with a general description of an organic semiconductor discussing the principle of conjugation and the origin of semiconductor properties. This is followed by a general outline on the formation of neutral and charged excitations and their involvement in the charge transport and luminescence processes. In particular, we focus on the properties of radiative and non-radiative transitions as well as selection rules both for isolated and interacting molecules. Finally, the working principle and structure of an OLED are presented.

Chapter 2 gives a description of the basic techniques used to understand radiative and non-radiative transitions, i.e. steady-state and time-resolved spectroscopies. In the second half of the chapter, we provide an outline on the fabrication procedure and characterization of solution-processed OLEDs.

In chapter 3 we study the impact of chemical modifications in a well-known class of near-infrared (NIR) emitters, namely benzotriazolothiadiazole-based polymers. Given the general interest in NIR emission, we investigate the substitution of a sulphur for a selenium atom as a competing strategy to push emission further into the NIR. We also investigate whether the functionalization of the polymer backbone with a straight alkyl side chain compared to a branched chain has beneficial effects for the incorporation of these materials into OLEDs.

Chapter 4 provides another example of a strategy to achieve NIR emission by exploiting the interface of two organic semiconductors with a proper gap between their energy levels. We select a discotic electron-transporting molecule and a hole-transporting poly-

mer whose have been shown to support the formation of excited-state complexes at their interface. We characterize the nature of the radiative decay from such state upon photo- and electrical-excitations.

In chapter 5 we report the investigation of a phosphorescent emitter, namely a Pt(II)-porphyrin complex, incorporated in the backbone of a polyfluorene polymer. We explore various loadings of the porphyrin content and evaluate the impact on the co-polymer optical properties. Given the potential of phosphorescence emitters to achieve nearly 100% internal quantum efficiency, we also incorporated the materials into OLEDs.

Chapter 6 presents a detailed study of the photoluminescence emission of a small molecule widely used in organic optoelectronics, namely [6,6]-phenyl-C_{61}-butyric acid methyl ester (PCBM), a functionalized C_{60}-fullerene. The emission is studied at cryogenic temperatures to allow for a highly resolved spectrum and therefore a fine understanding of the optical transitions. Given the importance of the crystalline phase for PCBM, we also compare the photoluminescence emission for samples with different crystallinity, from the amorphous phase to a solvent-free single crystal, whose growth have been only recently reported.

Finally, a summary of the achievements obtained as well as an outlook on future work is given in chapter 7.

1 Organic semiconductors

Organic semiconductors are a wide class of carbon-based materials that comprise small molecules and polymers showing semiconductor properties. These materials have attracted considerable attention in the second half of the twentieth century after the discovery of their electrical conductivity and electroluminescence (i.e. light emission upon electrical excitation). The first was discovered in doped polyacetylene in 1977 by Shirakawa, MacDiarmid and Heeger [6]. The second was reported in 1963 by Pope *et al.* for anthracene single-crystals [7] and in 1990 by Burroughes *et al.* for poly(*p*-phenylene vinylene) [8], a small molecule and a polymer respectively. Consequently, organic semiconductors became promising candidates for optoelectronic devices, such as OLEDs [8–10], organic photovoltaic cells (OPV) [11–14] and field-effect transistors [15–17]. Besides their optical and electronic properties, they offer several advantages, e.g. fine tunability of their chemical structure, use of solution-processing techniques, low-cost manufacturing, structurally flexible and large area devices production [2, 18, 19]. Indeed, organic optoelectronics is an emerging technology that has recently reached the commercialization stage, e.g. from OLED-based displays for televisions and mobile devices [3] to transparent and coloured photovoltaic façades [20]. Along with great progress in the technological developments, fundamental material properties and underlying processes that govern devices operation have been extensively investigated, e.g. charge transport [21], energy and charge transfer [22] and optical properties [23–25].

Some of the most common organic semiconductor classes typically investigated for optoelectronic devices are shown in Fig. 1.1. Widely studied fluorescent polymer emitters are poly(*p*-phenylene) [26], poly(*p*-phenylene vinylene)s (PPV) [27], polyfluorenes

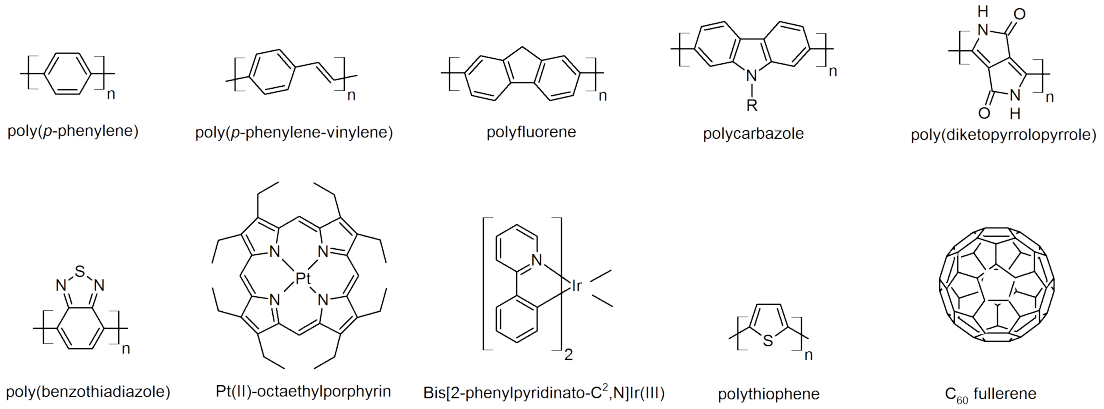

Figure 1.1: Chemical structure of representative organic semiconductor classes commonly used in optoelectronics and relevant for this thesis.

[4, 28], polycarbazoles [29], diketopyrrolopyrroles [30], benzothiadiazoles [31]. Among phosphorescent emitters, organometallic complexes based on iridium and platinum(II)-porphyrins have been demonstrated to show high electroluminescence efficiency [32, 33]. For organic photovoltaics, particularly important semiconductors are polythiophenes as donors and fullerene derivatives as acceptors [2, 34].

1.1 Electronic properties

1.1.1 π-conjugated system

The electrical conductivity in organic semiconductors results from the properties of the carbon atom when in a π-conjugated system [35]. The electronic configuration of a carbon atom in the ground state is $1s^2\ 2s^2\ 2p^2$. However, in order to explain the structure of carbon-based compounds, the concept of orbital hybridisation is introduced. By mixing *s* and *p* orbitals to form new hybrid orbitals with different shape, energy and spatial orientation than the unhybridized counterparts we can better describe carbon bonding.

In the case of conjugated systems, carbon is sp^2 hybridised (see Fig. 1.2a). The 2s orbital is mixed with two 2p orbitals, out of three 2p orbitals available, forming

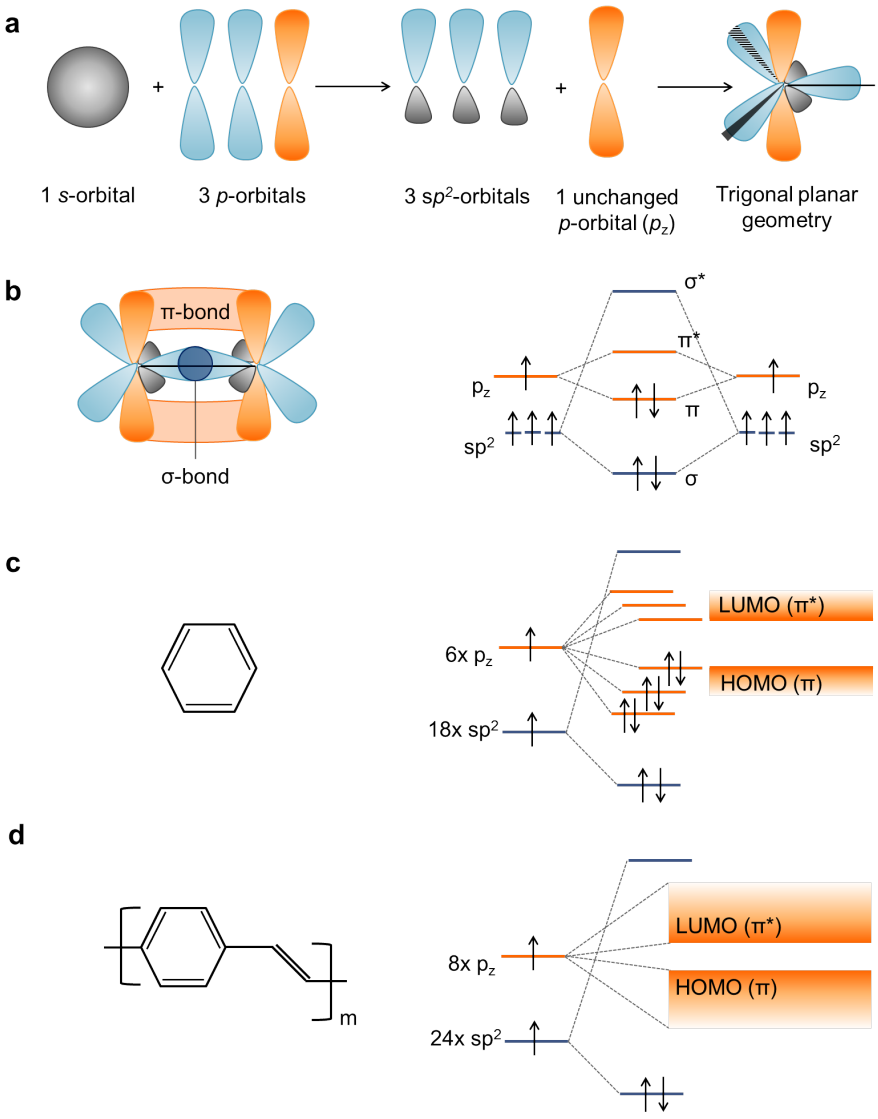

Figure 1.2: **a**, Representation of the sp^2 hybridisation for a carbon atom. Two 2p-orbitals and the 2s-orbital take part in the hybridisation process. This results in the formation of three sp^2-hybrid orbitals and one unchanged p-orbital that lies at right angles to the plane of the hybrid orbitals. Revised from the Nottingham Trent CELS resource. **b**, σ- and π-bonds formation for two sp^2-hybridised carbon atoms and the energy diagram showing the bonding and antibonding molecular orbitals. **c**, Chemical structure of benzene and its energy diagram. **d**, Chemical structure of PPV and its energy diagram. Increasing the number of carbon atom results in quasi-continuous bands of occupied and unoccupied states. Revised from orgworld.de

a total of three sp^2 orbitals containing one electron each. These three equivalent sp^2 orbitals are coplanar, with an angle of 120° between them, and form three *σ-bonds* with neighbouring atoms. The third 2p orbital, $2p_z$, contains one electron, does not take part in the hybridization and is perpendicular to the sp^2 plane. When a $2p_z$ overlaps with a $2p_z$ of another sp^2-carbon atom a *π-bond* (or double bond) is formed, as in ethene (see Fig. 1.2b). The region of overlapping extends above and under the σ-bond plane. The overlap of two $2p_z$ leads to the formation of a molecular bond and to the subsequent splitting into a bonding molecular π-orbital and an anti-bonding molecular π*-orbital. The π orbital is lower in energy than the original p_z orbital while the π*-orbital is higher in energy than the atomic orbital. Thus, in the ground state, the two electrons coming from the p_z orbitals of two carbon atoms will occupy the π-orbital. Similarly, the overlap of two sp^2 orbitals gives rise to the formation of a bonding σ-orbital and an anti-bonding σ*-orbital respectively lower and higher in energy compared to their respective π-orbitals.

Increasing the number of sp^2 hybridised carbon atoms results in quasi-continuous bands of occupied and unoccupied states where the highest bonding π-orbital is referred to as the *highest occupied molecular orbital* (HOMO) and the lowest anti-bonding π*-orbital as the *lowest unoccupied molecular orbital* (LUMO), i.e. as in benzene or PPV (see Fig. 1.2c-d). The energy difference between LUMO and HOMO, termed *energy gap* (E_g), defines some of the semiconductors properties. E_g reduces as the alternating single and double bound system extends affecting the HOMO/LUMO positions. For organic conjugated molecules, E_g is typically between 1.5 and 3 eV leading to optical transitions in the visible and near-infrared region of the electromagnetic spectrum.

Finally, we define a *π-conjugated system* an organic small molecule or polymer with alternating single and double bonds and characterized by the spatial extension of the π-orbitals over the carbon atoms backbone allowing delocalization of the electrons (conceptually described as a *resonance* bonding). Examples of π-conjugated systems are benzene and PPV, Fig. 1.2c-d. Note that the single and double bond alternation is a schematization as we know that the bond lengths between carbons are equal and,

specifically, intermediate between that of a single and a double bond. The electrical conductivity arises from the electron delocalization, in fact electrons are free to move along the carbon backbone as long as such resonance interaction between the π-bonds subsists. It is therefore evident that the conjugation length (that is, the extention of the π-electron delocalization) affects both the electrical conductivity and the optical properties. However, in polymers it is often disrupted because of intrinsic or dynamical defects as discussed in section 1.2.4. The conjugated segment of an organic semiconductor is referred to as *chromophore*. We can describe a polymer as a sequence of chromophores of a certain conjugation length with strong intramolecular electronic interaction (the resonant bonding) but weakly coupled one another.

1.1.2 Electronic excited state complexes and charge transport

In the previous section we said that conjugated polymers have strong intramolecular electronic interactions, arising from the resonance interaction between the π-bonds, and weaker intermolecular electronic interactions because of poor overlap of the electronic wavefunctions between adjacent chains or chromophore segments [36]. In the ground state, electronic wavefunctions are therefore usually localized on a single chromophore. Also, electron-electron interactions are not effectively screened because of a low dielectric constant and electron-lattice interactions are relevant. It follows a peculiar behaviour of the conjugated systems upon photo- and electrical- excitations. As a consequence, either charged or neutral excited state complexes (or electronic excitations) can be formed and because of their coupling with the environment they are referred to as quasi-particles [1] (see Fig. 1.3). These excitations are involved in the charge transport and luminescent properties of organic semiconductors.

An excess of charge in a conjugated polymer may be due to oxidation or reduction, charge injection or photoinduced charge transfer. The presence of a net charge locally modifies the ground-state equilibrium geometry (typically a benzenoid-like geometry for a non-degenerate ground-state system) with respect to the sense of bond alternation, i.e. it adopts a quinoid-like geometry (see Fig. 1.3). We define *polaron* a charged

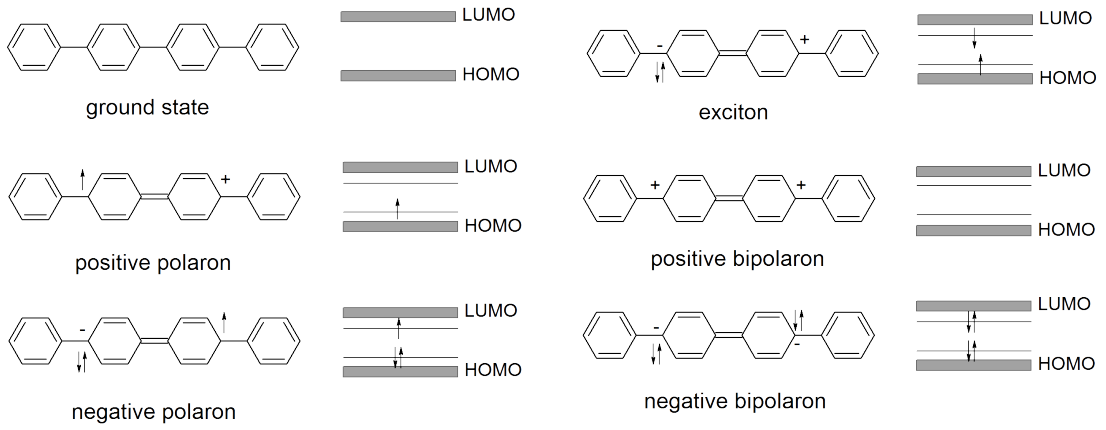

Figure 1.3: Structural changes of poly(*p*-phenylene vinylene) and the energy levels indicating the occupation of the midgap state upon neutral (exciton) and charged (polaron and bipolaron) excited state complexes. The presence of an excess of charge distorts the conjugated system from a benzenoid-like to a quinoid-like geometry. Revised from [37, 38]

.

quasi-particle (electron or hole) plus the distortion of the charge's surroundings, i.e. local rearrangement of bond alternation. The polaronic deformation can be seen as a lattice polarization that tends to localize the charge. However, polarons can move across the polymer chain and between chains influencing the charge transport as discussed below. Also, they create mid-states in the energy gap. Polarons can be either positive or negative depending on the charge carrier. Two polarons of the same sign weakly bounded are termed *bipolarons* for which the lattice deformation is the attracting force that counterbalances the Coulombic repulsion [5, 37].

As mentioned, polarons are typically localized states that prevent coherent charge transport since the charge is self-trapped by the distortion it creates in the system. Charge transport in organic semiconductors is still actively debated [21, 39, 40]. Band-like transport has been reported for highly purified pentacene and rubrene samples where electrons delocalization over different molecules is possible because of intermolecular electronic coupling. However, in presence of localized states, transport occurs via hopping mechanism between these states upon thermal activation or phonon-assisted tunneling

(emission/absorption of a phonon to overcome energy barriers). Room temperature charge mobilities (expressed as velocity over electric field) range from 10^{-6} up to 10^{-3} $cm^2 \cdot V^{-1} \cdot s^{-1}$ for disordered polymers and up to 0.1-1 $cm^2 \cdot V^{-1} \cdot s^{-1}$ for ordered structures [16, 41].

Given the low dielectric constant, i.e. typical values 2-4 [14, 42], the coulombic attraction between two opposite charges, a hole and an electron, is weakly screened. That is, the opposite charges still feel mutual attraction and as a consequence they can form electron-hole pair with relatively large exciton binding energies of ∼0.5-1.5 eV [43, 44]. Such electron-hole pairs are termed *Frenkel exciton*. Exciton diffusion or transport is usually described with Föster and Dexter energy transfer models (see section 1.2.3). Excitons are neutral quasi-particles that can be generate via photoexcitation, i.e. by promoting an electron to an excited state, or via electrical excitation, i.e. by mutual capture of free charges that come within close proximity. Depending on the total spin S, excitons can be singlets (S=0) or triplets (S=1). Upon photoexcitations, singlets are primary formed due to selection rules [23]. A photogenerated exciton can decay radiatively (i.e. photoluminescence) or non-radiatively, undergo charge separation, etc. Under electrical excitation, instead, injected charges interact forming either a singlet or a triplet state following a 1:3 ratio [45]. Again, excitons can then undergo a radiative (i.e. electroluminescence) or non-radiative deactivations. Further details on radiative and non-radiative exciton deactivation processes will be given in section 1.2.

In donor and acceptor systems, another state that plays a major role for the function of optoelectronic devices is the *charge transfer state* (CT state). The CT state is an intermediate state between the exciton and the charge separation at the donor/acceptor heterojunction. It is therefore relevant in solar cells for efficient generation of free charges [46]. It is characterized by both a ionic and an excitonic character and may have a weak optical coupling with the ground state [47].

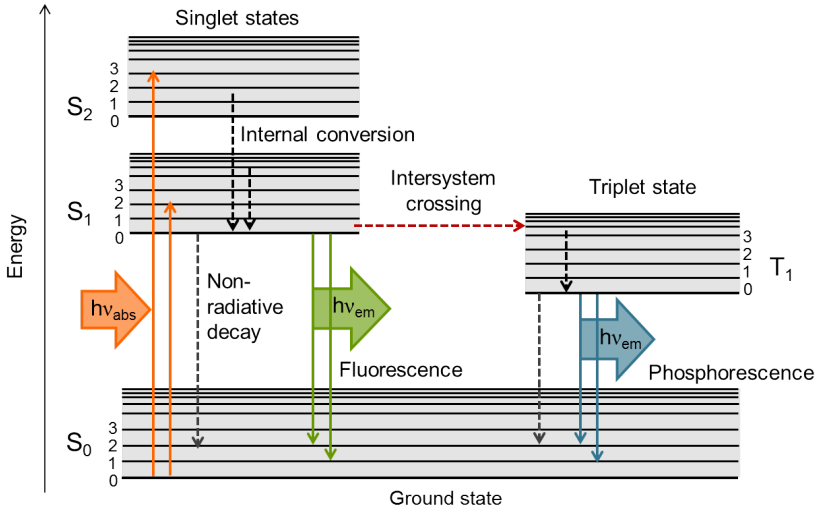

Figure 1.4: Jablonski diagram: S_0, S_1 and S_2 are the ground state, the first and second excited state respectively. T_1 indicates a triplet state. Radiative decays are represented with solid lines, non-radiative decays with dashed lines. Details on processes depicted in the diagram are reported in the text.

.

1.2 Optical properties

1.2.1 Jablonski diagram

In the previous section, we mentioned the formation of an exciton upon light absorption and its radiative decay, i.e. with emission of a photon. Here we illustrate the processes that occur between the absorption and the emission of light [48]. These processes are often visually described using a Jablonski diagram (see Fig. 1.4).

In Fig. 1.4, the electronic energy levels are indicated as S_0, S_1 and S_2, i.e. the ground state, the first and second excited state respectively. The states are arranged vertically by energy. For each electronic level, the vibrational levels are also shown, i.e. depicted by 0, 1, 2, 3 for S_0. Vibrational levels have a smaller spacing in energy ($\sim$0.1 eV) than electronic levels. Radiative processes, namely processes that involve the emission of a photon, are indicated with solid lines whereas non-radiative processes with dashed lines. States with different spin multiplicity are displayed horizontally.

The absorption is described as a vertical transition from S_0 to S_1 or S_2 ($h\nu_{abs}$ in Fig. 1.4) and occurs in about 10^{-15} s. Both S_1 and S_2 are excited singlet states, that is the electron is paired by opposite spin with the ground-state electron (spin angular momentum = 0). Usually, electrons promoted to S_2 relax to S_1 by *internal conversion* within 10^{-12} s. As stated by Kasha's rule, return to the ground state is most likely to take place from the lowest vibrational level of the first excited state, i.e. S_1. The return to the ground state can occur to higher vibration levels of S_0; electrons will then relax to the lowest vibrational level of S_0 within 10^{-12} s by internal conversion. The emission of light, or radiative decay, from an excited singlet state is called *fluorescence* and occurs in the nanoseconds time scale.

From S_1, conversion to a triplet state (T_1) may occur by *intersystem crossing*. In the triplet state, the electron has the same spin orientation as the one in the ground state (spin angular momentum = 1), the return to the ground state from T_1 is therefore spin-forbidden. Organic semiconductors are usually characterized by a weak spin-orbit coupling hence emission from triplet states is unlikely. Emission from triplet states occurs typically over milliseconds to seconds and is referred to as *phosphorescence*. Fluorescence and phosphorescence initiated by photoexcitation are generally termed *photoluminescence* (PL).

The *Franck-Condon principle* states that electronic transitions occur without changes of the nuclei position because the timescales of the two processes are significantly different, namely $\sim 10^{-15}$-10^{-16} s for the electronic transitions and $\sim 10^{-13}$-10^{-14} s for the nuclear vibrations to occur [49]. Also, the electronic transition will be more likely to happen between two vibrational levels whose wavefunctions overlap more significantly, see Fig. 1.5a. Usually the 0-0 transition is not the most probable one because the equilibrium geometry in the excited state is generally different to that of the ground state, this displacement in the nuclear coordinates is indicated as q_{01} in Fig. 1.5a. Given the energy diagram in Fig. 1.5a, the most intense transition is the vertical one as shown in Fig. 1.5b. Theoretically, emission and absorption are the mirror images of one another although many exceptions may occur.

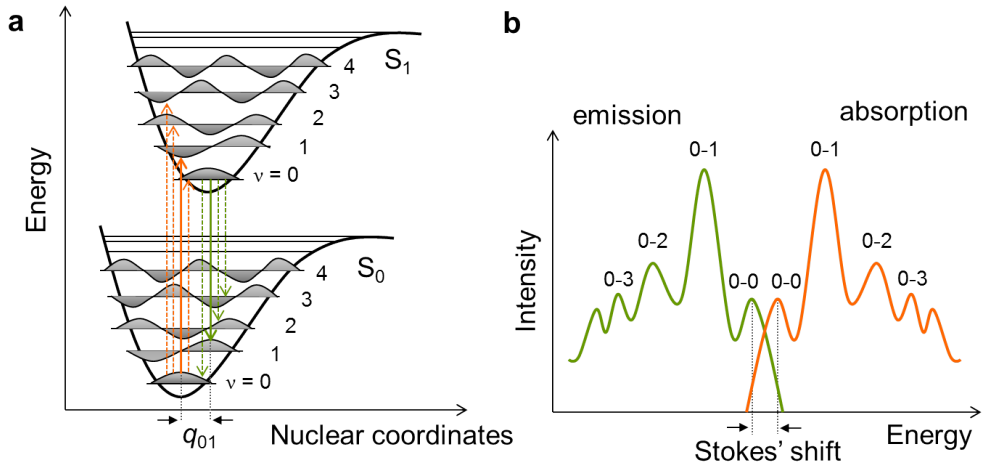

Figure 1.5: **a**, Morse potential energy curves for S_0 and S_1 of a diatomic molecule. The vibrational wavefunctions for each state are depicted in gray. The digram shows the Franck-Condon principle. The most probable transition is indicated with a vertical solid line: in this case the most favourite absorption/emission transition is between $\nu = 0$ and $\nu = 1$. **b**, Schematic representation of the absorption and fluorescence spectra corresponding to the energy diagram shown on the left and the mirror-image rule.

We define *Stokes' shift* the difference in wavelength between the 0-0 electronic transition positions of the absorption and emission spectra. In general, conjugated polymers show a broad absorption and emission spectra and a large Stokes' shift. The energy breadth of the spectra is given by defects along the polymer chain (i.e. conjugation breaks, chemical defects or conformational disorder). The absorption spectrum is usually more featureless; in fact it consists of absorption of chromophores with different conjugation lengths. The longer conjugation segments will have a lower π-π^* energy gap whereas the energy gap of the shortest segments will be much higher. On the contrary, the emission spectrum usually displays a structured band, the vibronic (combined electronic and vibrational) features, and is Stokes-shifted. The reason is that excitons on shorter conjugation segments (high energy) will relax by energy transfer to longer conjugation segments (low energy), so that the emission mainly comes from low energy states [24]. Vibrational relaxation (i.e. torsional relaxation) and electronic energy transfer to lower energy sites are the main causes of the Stokes' shift [50, 51].

The ratio between the number of photons emitted relative to the number of photons absorbed is a crucial parameter to describe the optical properties of a chromophore and it is defined as photoluminescence quantum efficiency, η_{PL}. It can be expressed in terms of the radiative and non-radiative rate according to the formula:

$$\eta_{PL} = \frac{k_{\mathrm{r}}}{k_{\mathrm{r}} + k_{\mathrm{nr}}}, \tag{1.1}$$

where k_r is the radiative rate of the fluorophore for $\mathrm{S}_1 \rightarrow \mathrm{S}_0$ and k_{nr} its non-radiative decay [48]. These processes are relevant in determining the limits to the efficiencies of optoelectronic devices such as OLEDs. An experimental method to determine η_{PL} is reported in section 2.1.1. In this context, the PL lifetime (τ) is a fundamental parameter to investigate excited state dynamics. It can be written as,

$$\tau = \frac{1}{k_{\mathrm{r}} + k_{\mathrm{nr}}}, \tag{1.2}$$

τ describes the average time a molecule stays in the excited state before returning to the ground state and it is particularly sensitive to the environment [48]. A method to investigate the PL lifetime is described in section 2.1.2. Combining eq. 1.1 and eq. 1.2 we can determine the radiative and non-radiative decay constants.

1.2.2 Selection rules

A more detailed description of absorption and emission of photons is given by quantum mechanics. By means of mathematical functions termed *wavefunctions*, we can describe electronic, vibrational and spin energies for a molecular system and therefore give a rigorous interpretation of allowed and forbidden processes mentioned in section 1.2.

The probability $P^2_{\Psi' \rightarrow \Psi''}$ for a molecule of a transition between two electronic states, i.e. the initial state Ψ' and the final state Ψ'', depends on the nature of the initial and final state wavefunctions and the strength of the interaction between incident photons and states [52]. In quantum mechanics, such probability is given by the square modulus of the electronic transition dipole moment, $|\vec{\mu}|^2$.

In mathematical form we can write the probability amplitude $P_{\Psi' \to \Psi''}$,

$$P_{\Psi' \to \Psi''} = \int \Psi''^{*} \cdot \vec{\mu} \cdot \Psi' d\tau = \langle \Psi'' | \vec{\mu} | \Psi' \rangle \tag{1.3}$$

Within the Born-Oppenheimer approximation, the wavefunction of a molecule can be described as a product of the electronic and the nuclear wavefunctions, ψ_e and ψ_n respectively. Therefore, the transition dipole moment can be writen,

$$\langle \Psi'' | \vec{\mu} | \Psi' \rangle = \langle \psi''_e \psi''_n | (\vec{\mu_e} + \vec{\mu_n}) | \psi'_e \psi'_n \rangle \tag{1.4}$$

Furthermore, the nuclear wavefunction ψ_n is further separated into vibrational and rotational contributions,

$$\Psi = \psi_e(r, R_{eq}) \cdot \psi_v(R) \cdot \psi_r(R) \tag{1.5}$$

where ψ_v is the vibrational component and ψ_r the rotational component. ψ_e depends on the nuclear positions but not on nuclear velocities. In fact, nuclei are seen as fixed in a position (R_{eq}, the equilibrium position) on the timescale of electrons motion given that nuclei are several thousand times heavier than electrons (the proton, itself, has a mass of $\mathrm{m}_p \simeq 1.7 \cdot 10^{-27}$ kg whereas an electron has a mass of $\mathrm{m}_e \simeq 9.1 \cdot 10^{-31}$ kg). Rotational and vibrational wavefunctions only depend on the nuclear coordinates R. Since the electronic spectra considered are not rotationally resolved, this contribution is not discussed any further.

Furthermore, ψ_e can be written as the product of the individual electronic spatial and spin wavefunctions,

$$\psi_e = \psi_{el} \cdot \psi_s \tag{1.6}$$

assuming that the interaction between the two components is negligible.

Combining Eq. 1.3, Eq. 1.5 and Eq. 1.6, we can write,

$$\begin{aligned}\langle \Psi'' | \vec{\mu} | \Psi' \rangle &= \int {\psi_v}''^* {\psi_s}''^* {\psi_{el}}''^* (\vec{\mu_{el}} + \vec{\mu_n}) \psi_v' \psi_s' \psi_{el}' d\tau \\ &= \int {\psi_v}''^* \psi_v' d\tau_v \int {\psi_s}''^* \psi_s' d\tau_s \int {\psi_{el}}''^* \vec{\mu_{el}} \psi_{el}' d\tau_{el} + \\ &+ \int {\psi_v}''^* \vec{\mu_n} \psi_v' d\tau_v \int {\psi_s}''^* \psi_s' d\tau_s \cancel{\int \psi_{el}''^* \psi_{el}' d\tau_{el}}\end{aligned} \tag{1.7}$$

Given the orthogonality of the electronic wavefunctions, the $\int {\psi_{el}}''^* \psi_{el}' d\tau_{el}$ term vanishes.

The probability for the transition $\Psi' \rightarrow \Psi''$ can finally be written,

$$P^2_{\Psi' \rightarrow \Psi''} \propto \underbrace{|\langle {\psi''}_v | \psi'_v \rangle|^2}_{\text{Franck-Condon factor}} \cdot \underbrace{|\langle {\psi''}_s | {\psi'}_s \rangle|^2}_{\text{Spin selection rules}} \cdot \underbrace{|\langle {\psi''}_{el} | \vec{\mu_{el}} | {\psi'}_{el} \rangle|^2}_{\text{Orbital selection rules}} \tag{1.8}$$

The first term of the right-hand side determines the overlap of the two vibrational wavefunctions, defined as *Franck-Condon factor*. The intensity of a vibrational transition is proportional to the square of the overlap integral between the vibrational wavefunctions of the two electronic states involved. A qualitative description of the Franck-Condon principle has been discussed in section 1.2 and depicted in Fig. 1.5a.

The second term states that spin-allowed transitions do not involve a change of the spin angular momentum, that is $|\langle {\psi''}_s | {\psi'}_s \rangle|^2 \neq 0$. Relaxation of this rule occurs through spin-orbit coupling which can be induced by the presence of heavy metals such as Pt in porphyrins.

The third term indicates that the incident photon should induce a large transition dipole moment for the transition to occur, even if there is a significant orbital overlap. If the orbital symmetry of the initial and final states is similar, the transition dipole moment will be negligible. Relaxation of this rule occurs through vibronic coupling. We point out that the Franck-Condon principle states that an electronic transition happens in a timescale short enough for the nuclear positions and velocities not to be changed by the molecular vibrations. Indeed, the electronic transition dipole moment is a function of the nuclear coordinates and it can be expanded as a Taylor series about the equilibrium energy of a particular state (say ψ'') for small displacements,

$$\vec{\mu_{el}}(Q'') = \vec{\mu_{el}}(Q_0{}'') + \sum_{k=1}^{N} \left(\frac{\partial \vec{\mu_{el}}}{\partial Q''_k} \right)_0 Q''_k + \text{higher order terms} \tag{1.9}$$

where Q''_0 is the equilibrium geometry of ψ'' (the final state) and N is the number of normal modes [53].

Truncation of the series to the zeroth order term is referred to as the *Franck-Condon approximation* (FC) and the electronic transition dipole moment is considered static. Strongly orbitally-allowed transitions have $|\vec{\mu_{el}}(Q_0{}'')| \gg 0$ and are well-described using this approximation. Consideration of the first order term of the series is referred to as the *Herzberg-Teller approximation* (HT) that describes weakly-allowed ($|\vec{\mu_{el}}(Q_0{}'')| \sim 0$) and orbitally-forbidden ($|\vec{\mu_{el}}(Q_0{}'')| = 0$) electronic transitions. The transition dipole moment varies linearly with the nuclear displacements. HT effects are relevant in many cases, i.e. C_{60}-fullerene [54] and cyclic porphyrins [55].

Concepts introduced in this section will be of use in chapters 5 and 6.

1.2.3 Energy and electron transfer

Photoexcitation results in an electronic excitation localized on a chromophore and can be transferred to other chromophores via electronic energy (or electron) transfer (EET) [49]. Important EET mechanisms are the Förster fluorescence resonance energy transfer (FRET) and the Dexter energy transfer. In both cases, the EET occurs between a donor in the excited state (D*) and an acceptor in its ground state (A) and the transfer is non-radiative. The process can be expressed as,

$$D^* + A \rightarrow D + A^* \tag{1.10}$$

where the * indicates the electronic excited state.

In FRET, the donor transfer energy to the acceptor through a resonant dipole-dipole interaction between dipole transition moments $\boldsymbol{\mu_1}$ and $\boldsymbol{\mu_2}$ (Fig. 1.6a). When the donor releases energy to return to its ground state it excites the acceptor via a non-radiative resonance energy transfer. The FRET efficiency is proportional to the overlap of the

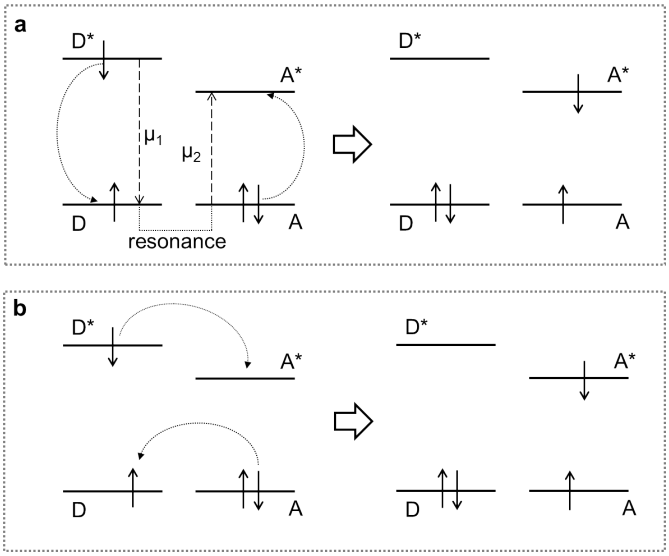

Figure 1.6: **a**, Förster fluorescence resonance energy transfer. **b**, Dexter energy transfer. Adapted from [56]

emission spectrum of the donor and the absorption spectrum of the acceptor and inversely proportional to the sixth power of the distance between donor and acceptor. The rate of energy transfer K_{et} can be written as,

$$k_{et}(dipole - dipole) \propto \frac{\boldsymbol{\mu_1^2} \cdot \boldsymbol{\mu_2^2}}{R_{DA}^6} \tag{1.11}$$

where $\boldsymbol{\mu_1}$ and $\boldsymbol{\mu_2}$ are the electronic transition dipole moments corresponding to the D* $\rightarrow$ D and A $\rightarrow$ A* respectively, and R_{DA} is the distance between the donor and the acceptor.

The Dexter energy transfer is induced by the electron exchange interaction (Fig. 1.6b). The electron in the excited state of the donor transfers to the excited state of the acceptor and concomitantly an electron in the ground state of the acceptor transfers to the donor ground state. The efficiency of this process decreases exponentially with the distance between donor and acceptor as this process needs the overlap of their wavefunctions to occur. The Dexter energy transfer may involve either singlet or triplet states.

The rate of energy transfer K_{et} can be written as,

$$k_{et}(exchange) \propto J \cdot \exp\left(\frac{-2R_{DA}}{L}\right) \tag{1.12}$$

where J is the spectral overlap, R_{DA} is the distance between the donor and the acceptor, and L is the sum of the Van der Waals radii of the donor and the acceptor.

An additional EET mechanism involves a radiative emission of the donor and the subsequent absorption of the emitted photon by the acceptor. In this case, no dipole-dipole interaction or electron exchange is needed. Such EET mechanism is favoured by donors with high PL efficiency and a good overlap between donor emission and acceptor absorption spectra.

1.2.4 Intra- and inter-molecular interactions

Conjugated polymers in solid-state typically show conformational disorder as schematically shown in Fig. 1.7a. Small-angle rotations around bonds break the conjugation length forming individual chromophore subunits along the polymer chain. Neighbouring subunits are strongly coupled one another and allow intrachain transfer. Interchain interactions happen between polymer chains in close proximity or chromophore subunits coupled through space (e.g. not adjacent) when the polymer is in a tightly coiled conformation [57].

The primary photoexcitation in organic semiconductor is an intrachain singlet exciton. However, intra- and inter-molecular interactions affect greatly the optical properties even when the photophysics of the conjugated systems is still governed by intrachain excitons [23].

Until now we have considered absorption and emission of a single chromophore but two or more chromophores can interact and absorb or emit light in a co-operative manner. If the interaction between two chromophores occurs in the ground state we refer to such molecular complex as an *aggregate* (or ground-state complexes) whereas if the interaction takes place only when one of the molecule is in the excited state (i.e. the donor) we call it an *excimer*, if the two chromophores are identical, or *exciplex*, if the two chromophores are chemically different.

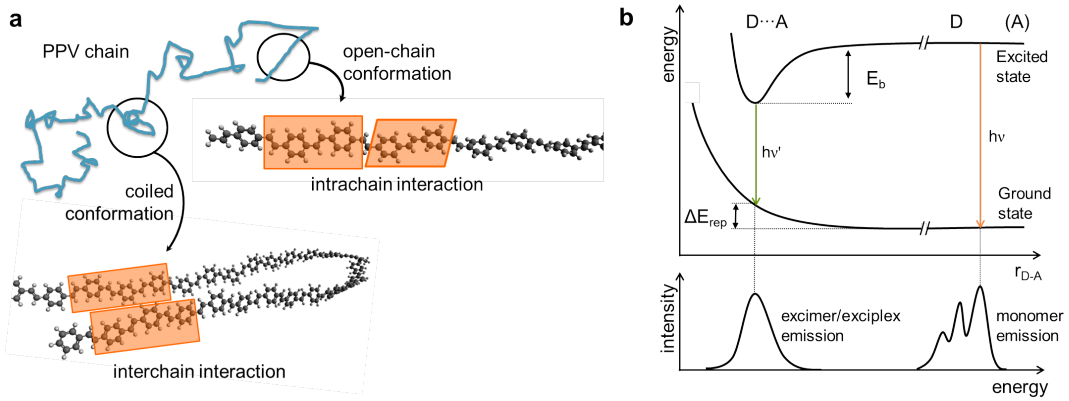

Figure 1.7: **a**, Conformational disorder in a poly(*p*-phenylene vinylene) polymer chain. The chromophore subunits are highlighted with orange boxes. Revised from [57, 58]. **b**, Potential energy diagram describing the excimer (if D=A) or exciplex (if D≠A) formation and emission with respect to a monomer (either D or A). See text for details. Revised from [49, 59].

Excimers (or excited dimers) are unstable in the ground state but not in their excited state and result from the interaction of one chromophore in the excited state, the donor (D), with another one in the ground state, the acceptor (A). Excimers have a partial charge transfer character. Exciplexes present similar characteristics; in fact they are analogous to excimers in which the excited state extends over a neighbouring molecule of a different chemical nature.

The distinctive optical feature of the excimer (or exciplex) is a structureless emission band red-shifted with respect to the exciton emission as schematically depicted in Fig. 1.7b. The difference between the monomer emission (isolated chromophore) and the excimer (or exciplex) emission, that is $h\nu$-$h\nu'$, is called spectral shift. Such spectral shift is related to the stabilization energy (or binding energy, E_b) of the excimer/exciplex and the ground-state repulsion energy, ΔE_{rep} (or energy of geometrical relaxation).

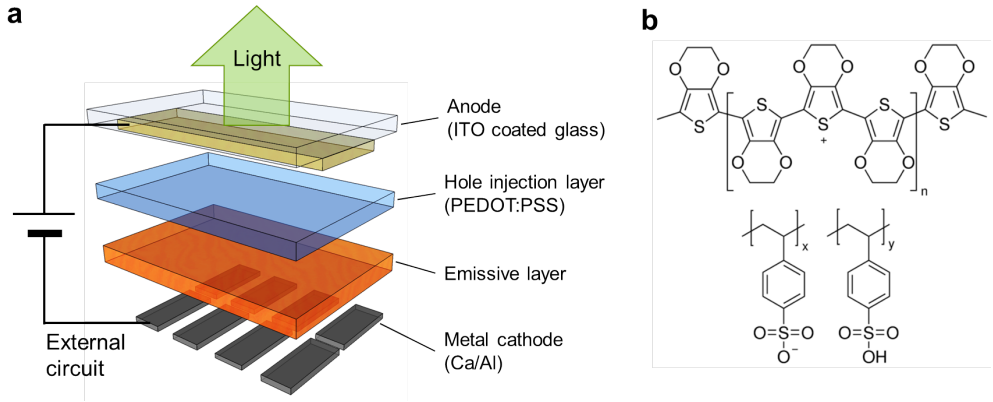

Figure 1.8: **a**, Basic OLED device structure. **b**, Chemical structure of PEDOT:PSS

1.3 Organic light-emitting diodes

1.3.1 Device structure

A well-established structure for an OLED consists of a thin film of an organic semiconductor, i.e. the emissive layer (∼100 nm), sandwiched between two electrodes. Typically a hole transporting layer is inserted between the anode and the emissive layer. A schematic representation of the device is reported in Fig. 1.8a.

The anode is usually made of indium-tin-oxide (ITO), In_2O_3 (90 wt%) and SnO_2 (10 wt%), that has a good transparency (up to 90% at 550 nm), a low sheet resistance (∼20 Ω/□) and a high work function (∼4.6 eV). The latter provides a low barrier for hole injection given that the HOMO of the emissive layer is typically 5-6 eV. Oxygen plasma treatment has been reported to increase the work function (∼4.7-4.8 eV), lower the sheet resistance (∼15 Ω/□) and decrease surface roughness (from 2.6 nm to 1.4 nm rms) [60].

Hole transporting layers (HTL) and/or an electron transporting layers (ETL) may be necessary to improve charge injection. In particular, poly(3,4-ethylenedioxythiophene)-poly(styrenesulfonate) (PEDOT:PSS, see Fig. 1.8b) is commonly used as HTL because lowers further the barrier for hole injection at the anode interface (∼5.2 eV) and acts as a hole transport layer [61].

Low work function materials are chosen for the cathode in order to reduce electron

injection barriers given that the LUMO of the emissive layer is typically 2-3 eV. A thin layer of calcium (∼30 nm), capped with aluminium (∼150 nm) to prevent degradation, is commonly used. Ca has a work function of ∼2.8 eV whereas Al of 3.7-4.2 eV [62].

1.3.2 Device operation

When a potential is applied, electrons and holes are injected in the emissive layer from the cathode and the anode respectively. Charges are transported through the emissive layer and when an electron and a hole capture each other via Coulomb interaction they form a bound excited state termed exciton. The exciton can then radiatevely recombine, this phenomenon is called *electroluminescence* (EL).

The energy level diagram for individual components of an ITO/emitter/metal OLED is reported in Fig. 1.9a. As mentioned in the previous section, a careful choice of electrodes with a proper work function, Φ_{metal} for the cathode and Φ_{ITO} for the anode, is needed in order to minimize energy barriers for holes (Φ_h) and electrons (Φ_e), respectively. Also, it follows that it is unlikely for electrons to be injected from the anode and holes from the cathode because of the high energy barriers. Φ_h and Φ_e are defined as the difference between the electrode work function and the relevant molecular energy levels,

$$\begin{aligned} \Phi_h &= E_{HOMO} - \Phi_{ITO} \\ \Phi_e &= \Phi_{metal} - E_{LUMO} \end{aligned} \tag{1.13}$$

Given that $\Phi_{ITO} \neq \Phi_{metal}$, when the materials are brought into contact there is a charge migration from the cathode towards the anode leading to the creation of a built-in voltage (V_{BI}), see Fig. 1.9b. This arises from the equilibration of the Fermi level (E_f or μ) throughout the structure (*vedi infra*). The electronic structure of the OLED can be described with the rigid band model because the depletion region in conjugated polymers (hundreds of micrometers) is greater than the thickness of the polymer layer (∼100 nm) [1]. Bands are therefore rigidly tilted by the built-in field with negligible band bending. We define V_{BI} the difference between the electrodes work function, V_{BI}=Φ_{ITO}-Φ_{metal}. It is also related to the energy gap by the following equation,

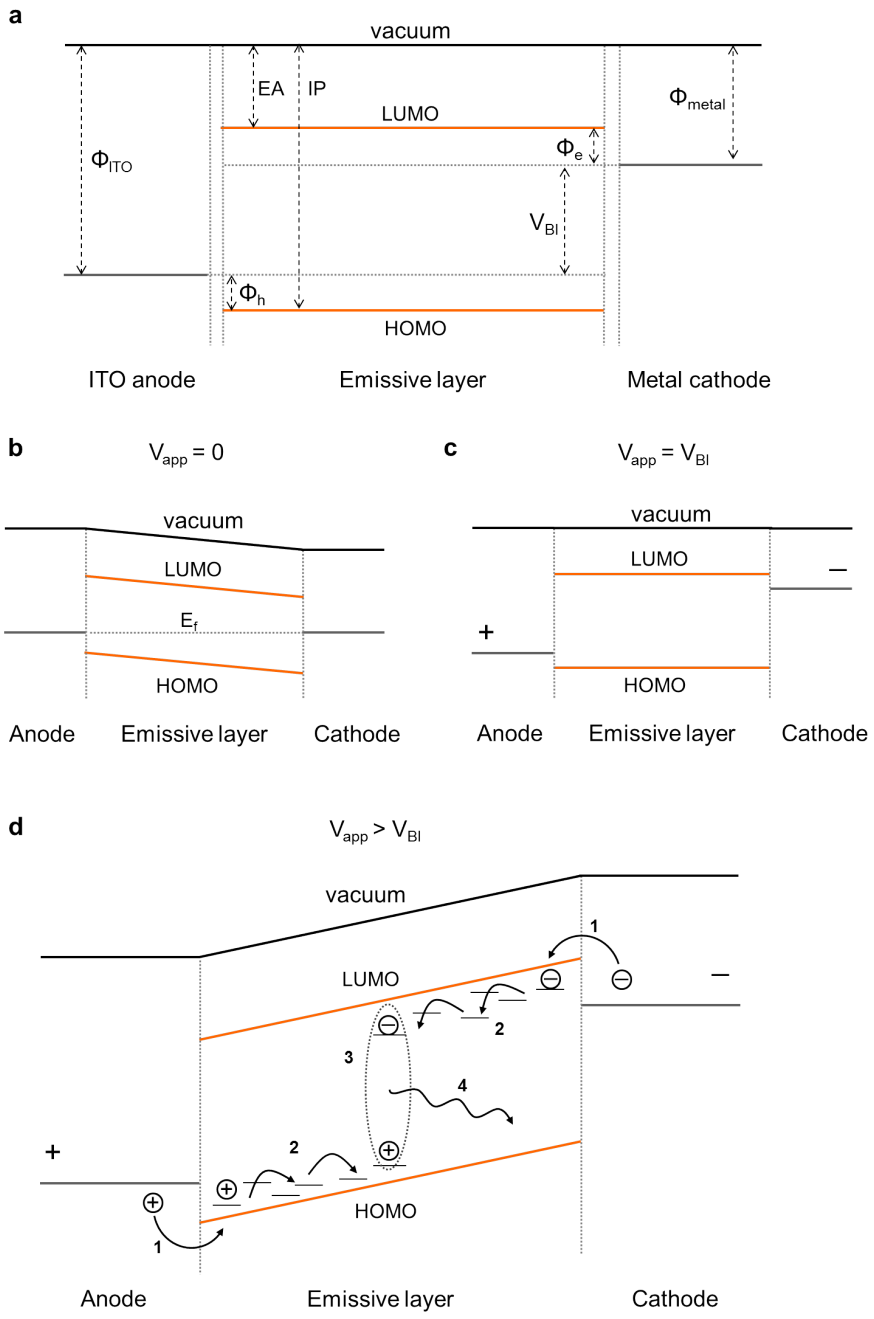

Figure 1.9: Energy level diagrams for an OLED (ITO/emitter/metal): **a**, before contact (isolated materials), **b**, after contact, **c**, flat band condition (V_{app}=V_{BI}) and **d**, under forward bias (V_{app}¿V_{BI}). The cathode and anode work function, Φ_{metal} and Φ_{ITO} respectively, the electron affinity (EA) and ionization potential (IP) of the organic semiconductor are reported with respect to the vacuum level. The built-in voltage (V_{BI}), the Fermi energy (E_f), the energy barriers for holes (Φ_h) and electrons (Φ_e). **d**, The fundamental processes of LED operation: electrons/hole injection (1), charge transport (2), exciton formation (3), radiative recombination and light emission (4). Adapted from [63].

$$E_g = eV_{BI} + \Phi_e + \Phi_h \tag{1.14}$$

In a band structure picture, when the applied voltage (V_{app}) is zero, the E_f is constant across the device. In a conjugated polymer, E_f does not correspond to an actual energy level and it is across the energy gap as in Fig. 1.9b. At thermodynamic equilibrium the Fermi-Dirac distribution f(ϵ) gives the probability for an electronic level of energy ϵ of being occupied at a given temperature and at any given time.

$$f(\epsilon) = \frac{1}{e^{(\epsilon-\mu)/(kT)} + 1} \tag{1.15}$$

with an occupancy of 50% when ϵ=μ, such level is then called the Fermi level.

When a forward bias is applied, the band slope decrease and cancels when V_{app} equals V_{BI}. This situation is referred to as flat-band condition and the voltage applied is the minimum bias required for charge injection (Fig. 1.9c).

The basic operation of an OLED at voltages V_{app}>V_{BI} is shown in Fig. 1.9d [64]. First, charges are injected into the organic semiconductors. For low energy barriers between the electrode and the polymer, the current that flows in the device is not injection limited and the charge carrier injection can be described with the Richardson-Schottky model. In this model, charges with enough thermal energy can overcome the potential barrier and being injected into the polymer. In this description the effective energy barrier is lowered due to the potential of image charge. In fact, a fraction of electrons in the delocalized state of the metal at the metal/polymer interface can diffuse into the polymer states leaving a positive image charge behind. Also, to have a complete description of the phenomenon, one should consider that injected charges may flow back to the metal and recombine with their image charges. When the energy barriers are relatively higher, the current is injection limited and the Fowler-Nordheim model describes better the charge injection. In this model, charge carriers are injected through a field-induced tunneling across a triangular potential barrier.

Upon injection, charge transport occurs by hopping, a thermally assisted tunneling of carriers between localized sites [41], see also section 1.1.2. Indeed, charges are localized in

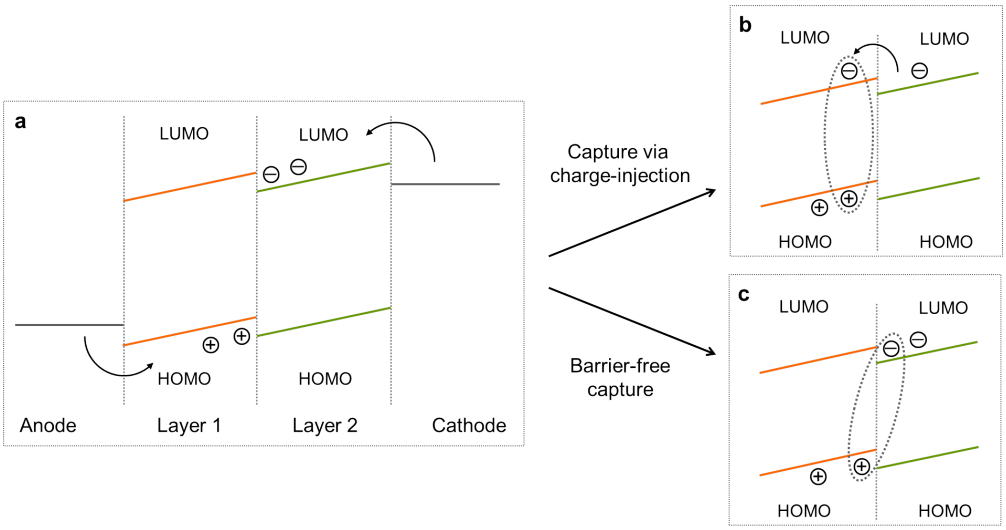

Figure 1.10: Electron-hole capture mechanism at the organic semiconductor heterojunction: **a**, electrons and holes accumulate at the opposite sides of the heterojunction, **b**, formation of an exciton, **c**, formation of an exciplex. Adapted from [4].

states that have a random spatial distribution and are energetically disordered. For low energy barriers, hole current can be space charge limited (SCLC) and electron current can be trap limited. SCLC originates because the hole mobility is low and charges can accumulate close to the anode interface and generated an electric field that opposes to the injection of other charge carriers. Electron transport, instead, is mainly affected by traps which are consequence of defect states. Injection from the cathode is generally less efficient leading to an imbalance in the charge carriers concentration.

Free charge carriers of opposite sign can recombine and form an exciton. Such recombination in polymers, that are low mobility materials, is often described as a bimolecular Langevin process for which the recombination rate is limited by diffusion of holes and electrons towards each other [65].

When two or more organic semiconductor layers are inserted in a LED, we also need to consider the electronic processes at their heterojunction [4]. We call type-II heterojunction a system where the HOMO and the LUMO levels of the one semiconductor are higher in energy than those of the other semiconductor (Fig. 1.10a). Such heterojunction is often exploited in OPV to efficiently dissociate the exciton formed upon light absorp-

tion. In OLEDs, charges are injected from the electrodes into the organic semiconductors so that electrons and holes accumulate at the opposite sides of the heterojunction. If a charge overcomes the energy barrier and transfers to the other semiconductor, electrons and holes can capture into an exciton (Fig. 1.10b). If electrons and holes capture prior to charge injection, an exciplex is generated (Fig. 1.10c). This mechanism is referred to as barrier-free capture. The exciplex can either decay radiatively or transfer to a bulk exciton upon thermal activation to overcome the energy barrier between the exciplex and exciton states.

Given a pair of spin-$^1/_2$ charges, excitons can be either a singlet (S=0) or triplet (S=1) in a ratio of about 3:1, i.e., 75% triplets and 25% singlet assuming that the formation probability is the same for singlets and triplets [45]. Radiative transitions are fully spin-allowed from the singlet states only. Usually the exchange energy, i.e. the energy between singlet and triplet states, is large and intersystem crossing from triplet states is unlikely; in some cases triplet states may participate directly in the emission as discussed in section 1.2.

The parameters that affect the efficiency of a LED are expressed in the external quantum efficiency (EQE). The EQE is generally defined as the ratio between the photons emitted and the charges injected and can be written as follows,

$$EQE = \eta_{PL} \cdot r_{st} \cdot \gamma \cdot \eta_{out} \tag{1.16}$$

where η_{PL} is the photoluminescence quantum efficiency; r_{st} is the ratio between singlets and triplets, i.e. 0.25; γ is the charge balance factor, i.e. how many excitons are generated per electrons injected in the device; and η_{out} is the light out-coupling efficiency, i.e. the amount of internally generated light that escape from the device that is limited by the difference in the refractive indices between layers, total internal reflection at the glass/air interface, etc.

The experimental setup to characterize electrical and optical properties of LEDs is described in section 2.2.

2 Experimental Techniques

2.1 Optical properties

2.1.1 Time-correlated single-photon counting

Time-correlated single-photon counting (TCSPC) is a technique for PL lifetime measurements [66, 67]. The principle of TCSPC is schematically depicted in Fig. 2.1.

The sample is repetitively excited with a short excitation light pulse (e.g. pulsed laser or LED) with high repetition rate. The conditions of TCSPC is the detection of a single photon per pulse and the measurement of its arrival time to the detector with respect to a reference, i.e. the excitation pulse. This means that the photons detected are time correlated to the excitation pulse.

TCSPC is a statistical method, the arrival times of photons are collected over multiple cycles and a probability histogram is built representing the PL intensity versus time. If for each pulse the probability to detect one photon is less than one, i.e. typically one photon per 100 excitation pulses, then the histogram represent correctly the time decay of the PL. If more than one photons arrive at the detector, the histogram is biased to shorter times (pulse pile-up problem) since only the first photon can be detected with this technique. To avoid the pulse pile-up, counting rates as low as 5% compared to the rate of the excitation light pulse are recommended.

The experiment begins when a pulse of light is simultaneously sent to the sample and the electronics. A constant fraction discriminator (CFD) measures precisely the arrival time of the two signals. After that the signal coming from the electronics (START) activates the time-to-amplitude converter (TAC) which generates a voltage that linearly

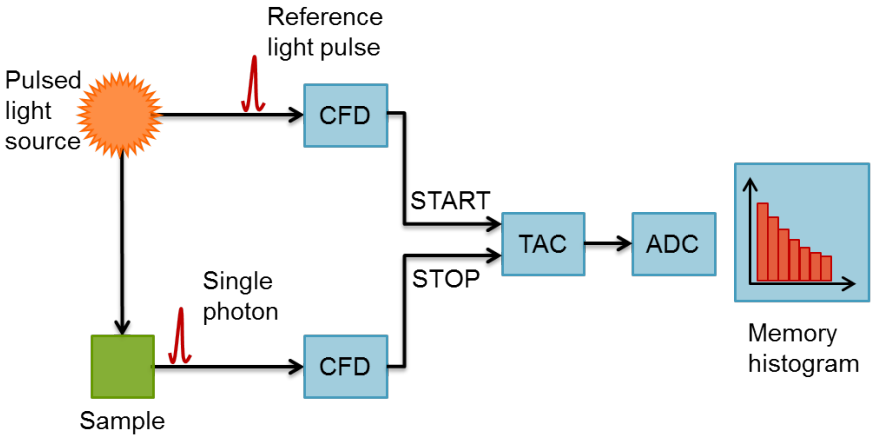

Figure 2.1: Schematic electronics for a time-correlated single-photon counting spectrometer. Revised from [66, 68].

increases with time. The TAC is stopped when the first photon is emitted by the sample (STOP). The time delay between the two signal is converted to a numerical value by the analog-to-digital converter (ADC) and registered in a time bin of the memory histogram. The probability histogram is built summing over a sufficient number of START-STOP cycles and represents the time decay of the PL.

To correctly examine the lifetime data, it is important to consider the instrument response function (IRF). The IRF is defined as the response of the instrument at zero lifetime sample. The width of the IRF arises from the excitation pulse width and the timing accuracy of the detector and the electronics. To measure experimentally the IRF, a scattering medium is placed in the sample holder. The parameters of the actual decay are extracted from the data after performing a reconvolution fit that considers the IRF.

The PL decay can be fitted using exponential functions of the form:

$$R(t) = A + \sum_{i=1}^{n} B_i e^{(-\frac{t}{\tau_i})} \tag{2.1}$$

Where n is the number of decay times, B_i are the pre-exponential factors, τ_i the lifetimes and A a constant that takes into account the background. In addition, the quality of the fit is assessed with a least-squares analysis where the value χ^2 gives the

goodness-of-fit.

Time-resolved PL measurements presented in this thesis were carried out with a TCSPC using a pulsed diode laser (Edinburgh Instruments-EPL-375, with a pulse width (FWHM) at 10 MHz of 55 ps and average power at 20 MHz of 0.10 mW) at 371 nm (or 405 nm) as excitation source and a cooled microchannel plate photomultiplier (Becker and Hickl PMC-100-1, with a spectral range of 200-850 nm, and dark count rates of 50 cps at -20°C) coupled to a monochromator and TCSPC electronics (Edinburgh Instrument Lifespec-ps TCC-900 PC card). The temporal resolution of the instrument is ∼150 ps.

2.1.2 Photoluminescence quantum efficiency

A method to evaluate the PL efficiency, η_{PL}, in the solid state for thin films of polymeric semiconductors has been reported by de Mello *et al.* [69]. The experimental set up involves a laser as excitation source, an integrating sphere whose inner surfaces are covered with a diffusively reflecting coating for the light to be isotropically redistributed in the sphere, and a detector.

The three set-up configurations required for the measurement are depicted in Fig. 2.2a-c. In experiment (a), the sample is not placed inside the chamber so that the detector registers the spectrum of the laser light. In experiment (b), the sample is hit by the laser beam and the detector measures both the laser light and the PL of the sample. Compared to case (a), the laser peak will be attenuated of a certain quantity that is equal to the amount of absorbed light by the sample. In experiment (c), the sample is placed inside the sphere but not in the laser path to take into account the fraction of diffuse laser light absorbed by the sample.

The area under the laser signal is denoted as L and the area under the PL emission as P. We can therefore calculate the η_{PL} as:

$$\eta_{PL} = \frac{P_c - (1 - (1 - \frac{L_c}{Lb}))P_b}{L_a - (1 - \frac{L_c}{Lb})} \tag{2.2}$$

where the subscritps a, b and c refer to the experiment a, b and c, respectively, as

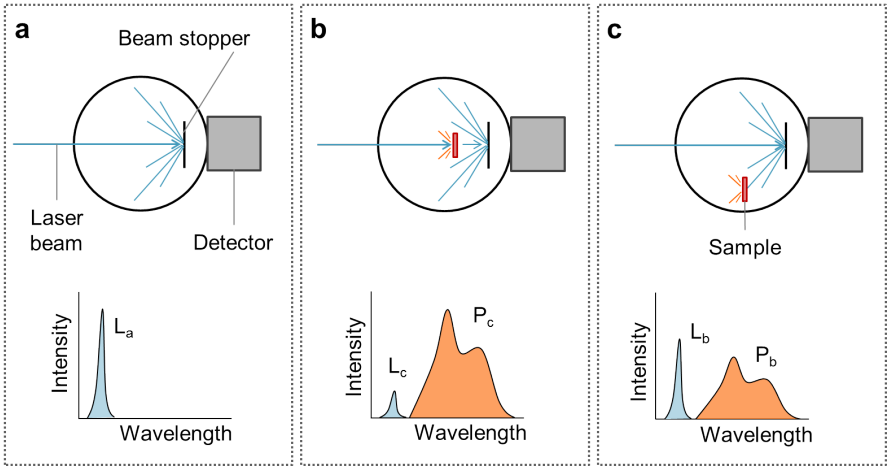

Figure 2.2: Schematic representation of the PL efficiency measurement.The black circle represents the integrating sphere. The experiment required three configuration: **a**, the sample is not placed into the sphere; **b**, the sample is placed in the laser beam path; and **c**, the sample is placed inside the sphere and hit by the laser light reflected by the sphere walls, not by the laser light directly. Revised from [69].

described in Fig. 2.2.

2.2 Organic-light emitting diodes

2.2.1 Fabrication

OLEDs reported in this thesis were prepared as follows. The thickness of the organic layers is measured using a Dektak profilometer.

Commercially available ITO substrates are cleaned with a sonication bath in acetone (for 15 min, to remove the protective layer) and subsequently in isopropanol (for 15 min) and finally blow dried. The thickness of the ITO layer is ∼100 nm. The substrates are then placed inside an oxygen plasma cleaner (Harrick PDC-002), with oxygen pressure of $\sim 1 \cdot 10^{-1}$ mbar, for 10 min.

Soon after the oxygen plasma cleaning, the hole injection layer (PEDOT:PSS) is deposited onto the substrate. In fact, the coating of ITO with a polymeric layer preserves the modification of the workfunction due to the oxygen plasma treatment [70]. A 2.8

%wt PEDOT:PSS dispersion in water is filtrated through a 0.45 μm filter and spin-coated at 4000 rounds per minute (rpm) for 60 s and 5000 rpm for 10 s to obtain a ∼80 nm thick film. A thermal treatment in nitrogen atmosphere at 180°C for 10 min removes residual water.

The following fabrication steps and the device characterization are performed in nitrogen atmosphere to prevent oxygen degradation.

Organic semiconductors are usually soluble in organic solvents. A proper choice of solvent and concentration is necessary to obtain a smooth layer with a thickness of ∼100 nm. The emissive layer is deposited on top of the PEDOT:PSS layer via spin-coating.

The cathode is deposited via thermal evaporation. The devices are placed inside an evaporator chamber. A piece of metal (calcium or aluminium) is placed in a crucible and heated. The process is held in vacuum ($\sim 10^{-6}$mbar). A 30 nm of Ca is evaporated at a rate of 0.4 Å$\cdot$ s^{-1} and 150 nm of Al at a rate of 2.0 Å$\cdot$ s^{-1}.

2.2.2 Characterization

The measured values of light emitted from OLEDs can be expressed either in radiometric or photometric units. Radiometric units express the number of photons emitted by the device whereas photometric units weight the light emission to the sensitivity of the human eye giving the actual brightness perceived by the eye. Photometry is restricted to the visible part of electromagnetic spectrum, from about 400 nm to 700 nm. Light emission in the near-infrared (from about 700 nm to 1400 nm) is therefore expressed in radiometric units.

In radiometric units, the emission intensity is measured as *radiance* (W$\cdot$sr$^{-1}\cdot$m^{-2}). The OLED is approximated to a Lambertian light source, that is a surface that have the same radiance in any direction. The corresponding photometric unit is the *luminance* (cd$\cdot$m^{-2}). Luminance values for commercial applications range from 300 cd$\cdot$m^{-2} for mood lighting up to thousand cd$\cdot$m^{-2} for illumination. The candela (cd) is the unit of measure for the luminous intensity according to the SI. The NIST gives the following definition:

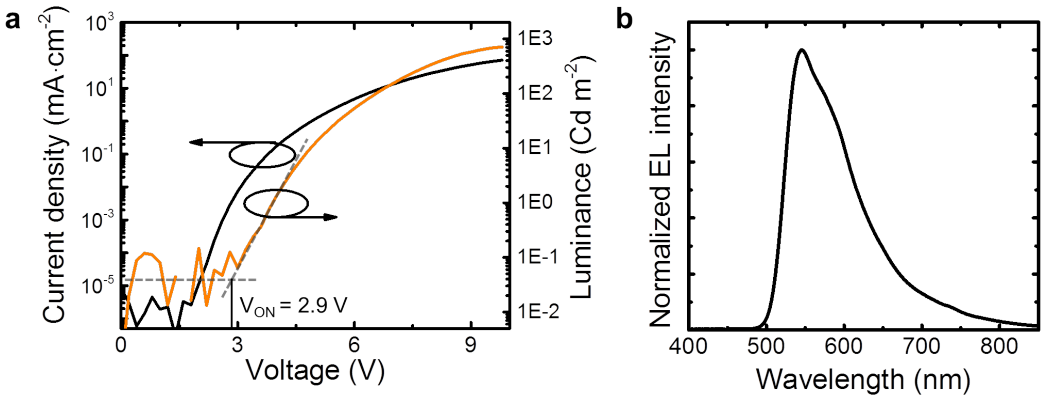

Figure 2.3: Example of ITO/PEDOT:PSS/F8BT/Ca/Al LED characteristics. **a**, Semi-log plot of the current-voltage-luminance characteristics. The turn-on voltage (V_{ON}) is indicated. Current below 1.85 V is due to micro short circuits and imperfections (residual leakage curreny), **b**, Normalized electroluminescence spectrum at taken 8 V.

"The candela is the luminous intensity, in a given direction, of a source that emits monochromatic radiation of frequency 540·10^{12} hertz and that has a radiant intensity in that direction of $^{1}/_{683}$ watt per steradian"

where the frequency chosen corresponds to 555 nm, that is the wavelength at which the human eye is most sensitive, and steradian (sr) is the SI unit for the solid angle (Ω). For a sphere of radius r, the solid angle is given by:

$$\Omega = \frac{A}{r^2} \tag{2.3}$$

where A is the surface area of the spherical cap. When $A = r^2$, the subtended solid angle is 1 sr.

The current density and luminance versus voltage (JLV) characteristics is measured with a Keithley 2004 source-meter and a calibrated Si photodiode coupled to a Keithley 2000 multimeter. As an example, the JLV characteristics for an OLED based on poly[(9,9-di-n-octylfluorenyl-2,7-diyl)-alt-(benzo[2,1,3]thiadiazol-4,8-diyl)] (F8BT) as emissive layer is reported in Fig. 2.3a.

A unified model has been recently proposed to interpret the current-voltage (I/V)

characteristic in the SCLC regime [71]. The initial region at low voltages can be described with the Ohm's law. For higher voltages, the curve is fitted by a quadratic function called Child's law and, finally, the last region is described with a higher than quadratic relation where mobility is dependent on temperature, electric field and/or charge carrier concentration. The charge injection occurs at the flat band condition. Any current below this voltage threshold is due to micro short circuits and imperfections and referred to as residual leakeage current.

A Si photodiode, with an area of 100 mm^2, detect photons emitted by the device (the emitting device area is 3.5 mm^2). The turn-on voltage (V_{ON}) is the minimum bias at which light is emitted from the device above the background noise. We arbitrarily defines the V_{ON} as the value of bias at which the current density is above $\sim$5 times the noise level or as the intercept of the I-V curve (in the linear range) with the noise level in the semi-log plot (i.e $\sim 5 \cdot 10^{-5}$ $Cd \cdot cm^{-2}$ in Fig. 2.3a). The light output intensity is directly proportional to the current flowing through the LED.

The emission intensity versus wavelength, i.e. the EL spectrum (Fig. 2.3b), is measured with an ANDOR-Shamrock spectrograph coupled with an ANDOR-Newton charge-coupled device (CCD) unit.

3 Near-infrared emitters based on thia- and selena-diazole

We report the optical characterization of NIR emitters for polymer LEDs (PLEDs) applications based on the copolymerization of a phthalimide-thiophene host polymer with a low-gap emitter based on containing the bisthienyl(benzotriazolothiadiazole) unit. We investigate different loadings of the low-gap emitter (in the range 1-3% by weight) and the substitution of a sulphur atom with a selenium atom to further extend the emission in the NIR up to 1000 nm. PLEDs based on copolymers with 1% loading give the best efficiency (0.09%) and show an almost pure NIR EL (95% in the NIR) peaking at 895 nm.

Materials were received from Dr. Timothy Steckler of the Prof. Mats Andersson's group (Chalmers University of Technology) who also determined the HOMO/LUMO levels for the materials. The following chapter is reproduced by permission of The Royal Society of Chemistry (see Ref. [72]).

3.1 Strategies and material design to achieve near-infrared emission

Over the last few years NIR OLEDs have generated considerable interest for their potential application in the medical, telecommunication and defence fields [73, 74]. Interestingly, the peculiarity of light emission in the NIR region (700-2500 nm) can be combined with the major advantages of OLEDs such as the solution processing, the low-cost fabrication and the possibility of using flexible, conformable or even stretchable

substrates [18, 75].

Given the importance of NIR optoelectronics, different organic compounds have been explored as red and NIR emitters, such as small molecules, [76–78] metal-organic complexes, [79, 80] conjugated polymers [81, 82] and recently perovskites [83]. Furthermore, different strategies have been employed to reduce emission quenching and aggregation effects of low-gap emitters and/or promote energy transfer to NIR moieties, e.g. by blending the NIR emitters with wider gap polymers, [80, 84], by diluting them in a matrix by co-evaporation, [85, 86], by exploiting cyclic or linear molecular π-system with appropriate ligands to inhibit aggregation [87] or via excited charge-transfer excitons at the organic semiconductors heterojunction with a proper gap between the energy levels for the emission to fall in the NIR [88] (see chapter 4).

Among these strategies, inclusion of donor-acceptor-donor (DAD) low-gap units in wider gap host polymer via copolymerization has been demonstrated as a valid approach [89,90]. In particular, benzothiadiazole and both its homo- and hetero-annulated derivatives have been extensively investigated [91, 92] in conjunction with different host polymers for efficient NIR LEDs emission [31, 90, 93–95]. A promising route to extend further the emission in the near-infrared region is the replacement of the sulphur atom in the benzothiadiazole unit with selenium. In fact, benzoselenodiazole units have been reported to reduce the polymer energy gap and lead to a red-shift of the absorption and emission spectra compared to the sulphur-containing unit [96–100].

The efficiency of NIR emitters is generally lower than that of visible emitters, owing to more efficient non-radiative quenching of the excited states which follows from a generally smaller exchange energy, and the smaller number of vibrational quanta needed to dump the energy of excited states in vibrational deactivation processes. Polymers for LEDs with emission beyond 850 nm have been reported with EQEs of only 0.02-0.05% [94,101], although recently we reported an EQE of 0.27% for a NIR PLED emitting at 885 nm [93]. In this and earlier reports we found that using ambipolar host polymers such as phthalimide-thiophene [93] and F8BT [84, 87, 102] can yield high EQEs for NIR emission. Following from the success of using pthalimide-thiophene host polymers, in

this study we look at modifications to the NIR emitting moiety to shift the emission further into the NIR whilst maintaining high EQEs.

We present NIR emitters (see Fig. 3.1a) based on a phthalimide-thiophene host polymer (**P1**) copolymerised with a low-gap DAD moieity based on the bisthienyl(benzotriazolothiadiazole) unit at different loadings, 1% and 3% (**P2** and **P3**, respectively) calculated with respect to the host polymer portion for the initial ratio of reactants. To lower the energy gap, we also exchanged a sulphur atom in the thiadiazole for a selenium atom (**P4**). Note that the branched alkyl side chains of the DAD unit for the **P4** copolymer are longer than those of the **P2** and **P3** copolymers.

It should also be noted that the phthalimide-thiophene host polymer used in this study has a straight alkyl chain ($C_{16}H_{33}$) as the solubilizing group whereas a phthalimide-thiophene host with branched side-chains ($CH(C_8H_{17})_2$) was used by Steckler and co-workers for NIR OLEDs in a previous study [93]. In the past study Steckler *et al.* showed that a straight side-chain phthalimide thiophene copolymers showed higher and more balanced ambipolar field-effect mobilities, increased order and higher photoluminescence quantum efficiencies than its branched side-chain analogue, but here we report the use of these straight-chain phthalimide thiophene copolymers as host materials for OLEDs for the first time.

In particular, we found a relatively high EQE (0.09%) for **P2** with an EL at 895 nm characterized by a high spectral purity (>95% in the NIR). We also show that the substitution of the sulphur atom in the thiadiazole unit of the DAD with a selenium atom (**P4**) red-shifts the emission to a band peaking at 990 nm, also yielding one of the most efficient PLEDs reported to date at such a long wavelength [94].

3.2 Experimental details

All the optical measurements reported are taken in the solid state. We prepared thin films (100 nm) of polymers by spin-coating (2 krpm) a 1.5 wt.% chloroform solution over a Spectrosil fused silica substrate. The steady-state PL spectra were recorded after exciting the PL with a 405 nm diode laser with an ANDOR Shamrock spectrograph

coupled with an ANDOR Newton CCD unit. Time-resolved PL measurements were carried out with a TCSPC spectrometer as described in section 2.1.1. The PL efficiency was measured using an integrating sphere method (see section 2.1.2) [69].

The polymers were also tested in PLED devices as the active layer. PLEDs were fabricated by spin-coating (4 krpm) a 2.8 wt.% dispersion in water of PDEOT:PSS [62] (Sigma Aldrich) to a thickness of a 80 nm over an ITO-coated glass pre-treated with oxygen plasma (10 min at 10.2 W) [60]. The substrates were then baked at 150°C for 10 min in a nitrogen atmosphere to remove residual water. The active layer was deposited by spin-coating (2 krpm) a 1.5 wt.% chloroform solution to obtain a thickness of 100 nm. Ca/Al electrodes (30 nm/150 nm respectively) were thermally evaporated under vacuum, at 10^{-6} mbar) on top of the active layer. We fabricated eight devices per polymer. Current-voltage-radiance characteristics were measured with a Keithley 2004 source meter and a calibrated Si photodiode (wavelength range of 200-1100 nm) coupled with a Keithley 2000 multimeter, EL spectra were taken with the ANDOR spectrometer described above (see section 2.2).

Square-wave voltammetry was used to determine the HOMO/LUMO levels of the polymers (Chalmers University of Technology. We thank T. Steckler for the measurement). **P1** has a HOMO of -6.05 eV and a LUMO of -3.45 eV. These values are very similar to what has been reported previously for the same polymer with either a different end-capping unit or no end-capping [93]. Due to the small loadings of the NIR-emitting segments, square-wave voltammetry of polymers **P3**-**P4** showed no signal from the low gap segments as it has been reported previously for polymers with similar loadings [93]. Likewise, based on previous studies of similarly structured compounds in the literature, we estimated the HOMO/LUMO levels of the NIR-emitting segments to be $\sim$ - 5.1/- 4.0 0.1 eV for segment of **P2** and **P3** [92] and a slightly narrow HOMO/LUMO gap for segment of **P4**. Since the HOMO/LUMO levels of these segments lie within the HOMO/LUMO levels the host polymer **P1**, this ought to allow for charge and energy transfer to the NIR-emitting segments. [103–105]

3.3 Optical characterization

We report the absorption spectra of the polymer films in Fig. 3.1b, in which we note that the host polymer (**P1**) absorption band is centred at 470 nm. As expected, all the copolymers display the host polymer absorption peak. In addition, **P3** (the copolymer with 3% b.w. content of DAD) clearly shows a band at 790 nm that is not visible in the host polymer, and that we thus assign to the DAD moiety. The DAD absorption is not clearly distinguishable in the other copolymers (**P2** and **P4**) due to the lower content (1% b.w.) of such a moiety. However the solution spectra show the absorption feature of the DAD unit peaking at 756 nm, 767 nm and 859 nm for **P2**, **P3**, and **P4** respectively (see Fig. 3.1c).

We report the PL spectra of the polymers in Fig. 3.1d. Emission from the host polymer (**P1**) features a band at 605 nm, whereas, as intended, the copolymers also show an emission band in the NIR region, peaking at 895 nm (**P2**), 927 nm (**P3**) and 1000 nm (**P4**), respectively. We attribute such bands to states delocalised over the DAD segments. Emission from the host polymer is still visible in the PL spectra of the copolymers, however, thereby suggesting that energy transfer from the host segment to DAD is not complete. This is consistent with the fact that the spectral overlap between the host polymer emission and the DAD unit absorption is not optimal as the emission of **P1** in not centred on the DAD unit absorption (this is detailed by the shaded area in Fig. 3.2a). We also expect a red-shift of the lower energy band when increasing the DAD loading [90] as a result of aggregation. Similarly, we expect an even more significant red-shift when substituting S with Se, owing to a lower LUMO level as suggested from the solution spectra in Fig. 3.1c. Whereas this is appealing for the purpose of achieving an as pure as possible NIR emission, any red-shift should also lead to a less efficient energy transfer from **P1**, which is undesired. Both expectations (red-shift and less-efficiency energy transfer, leading to lower NIR intensity) are confirmed by the trends observed in Fig. 3.1d. In fact, we observe that the percentage of the PL in the NIR (i.e. taken for wavelengths > 700 nm) are 31% (**P2**), 24% (**P3**) and 21% (**P4**), respectively. Upon increasing the DAD loading from 1% (**P2**) to 3% (**P3**), we notice a red-shift of the

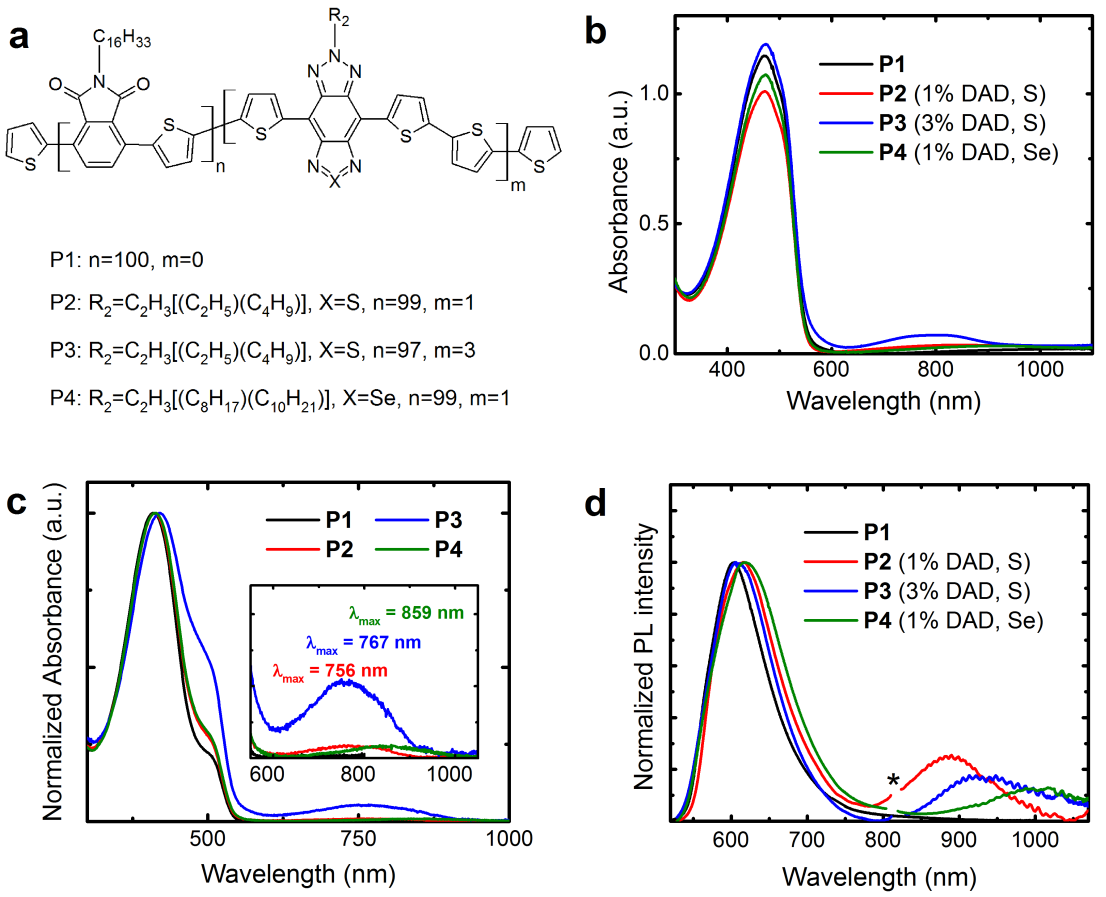

Figure 3.1: **a**, Chemical structure of the wide-gap host polymer (**P1**) and the copolymers (**P2**, **P3** and **P4**). **P2** and **P3** differ in the DAD loading (1% and 3% respectively). The DAD unit in **P2** and **P4** differs in the substitution of a sulphur atom for a selenium atom to lower the energy gap. **b**, Absorption spectra of the polymers thin films (100 nm) over fused silica glass. We report in the legend the percentage of DAD moieties and the type of atom (S or Se) in the DAD segment. **c**, Absorption spectra for polymers **P1** – **4** in $CHCl_3$ solution. We thank T. Steckler for the data. **d**, PL of polymers thin films, the * indicates the monochromator 2nd-order transmission of the excitation wavelength. Adapted from Ref. [72] with permission from The Royal Society of Chemistry.

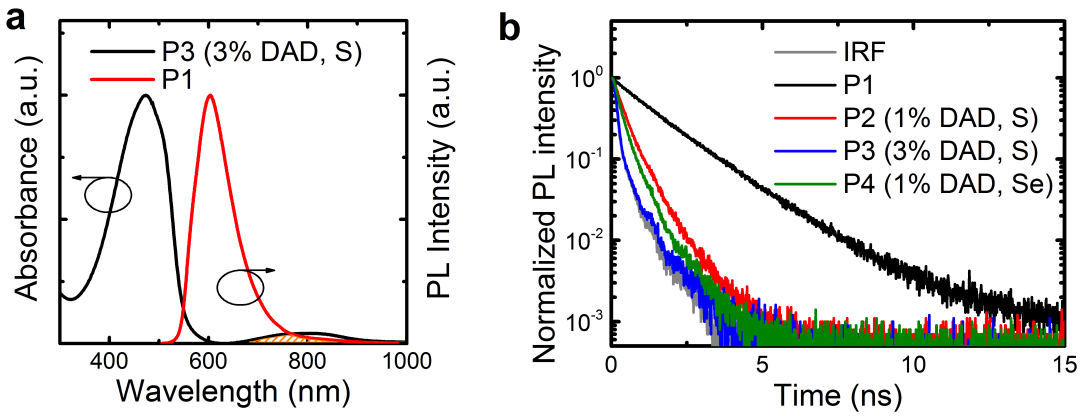

Figure 3.2: **a**, Normalized absorption spectrum of **P3** superimposed on the normalized emission spectrum of **P1**. The overlap between the absorption of the DAD unit and the **P1** emission is highlighted in orange. **b** PL time decay for thin films (100 nm thick on fused silica glass) of polymers **P1**, **P2**, **P3** and **P4** taken at 610 nm, following excitation at 371 nm. The IRF is also reported. Ref. [72] - Reproduced by permission of The Royal Society of Chemistry.

DAD unit PL emission from 895 nm (**P2**) to 927 (**P3**). We attribute such a red-shift to aggregation of the DAD moieties [90]. The exchange of sulphur with selenium in the benzothiadiazole also shifts the DAD unit emission further from 895 nm (**P2**) to 1000 nm (**P4**). Indeed, the introduction of benzoselenadiazole moieties is thus confirmed as a successful approach to lower the polymer energy gap and enable emission up to 1000 nm.

We also found the films PL efficiency (in the 500-1100 nm range) to drop from 14.8% for the host polymer **P1**, to 1.4% for **P2**, 1.0% for **P4**, and below our 1% sensitivity limit for **P3**. As mentioned, such a reduction is entirely expected as a result of both the reduction of the energy gap, and because of quenching/aggregation (e.g. in the comparison **P2** vs. **P3**). To investigate further the energy transfer between the host polymer and the DAD unit, we measured the PL lifetime decays of the host polymer emission (at 610 nm) for all the samples, and we report the results in Fig. 3.2b. The lifetimes of the host polymer **P1** can be fitted with a mono-exponential that returns a 1.65 ns time constant. The copolymers show a drop in the lifetime to 0.50 ns for **P2**

and to 0.32 ns for **P4** whereas the lifetime of **P3** is below the detection limit of the apparatus [106]. We note that such reduction in the lifetime follows the PL quenching of the host polymer by the presence of the DAD unit. The quenching is stronger when using Se instead of S and when increasing the concentration of the DAD unit.

3.4 Impact on electroluminescence

We also incorporated the copolymers into PLEDs with ITO/PEDOT:PSS anodes and Ca/Al cathodes. We report the EL spectra of the devices above in Fig. 3.3a. Whereas the host polymer shows essentially a single band (albeit with a main peak at 560 nm and a shoulder at 605 nm), the EL from the copolymers is predominantly in the NIR and peaking at 895 nm for **P2**, 939 nm for **P3** and ∼990 nm for **P4**. Although relatively noisy, it is possible to note that the emission of **P4** shows a shoulder at 807 nm. The percentage of NIR ($>$ 700 nm) EL is 95% (**P2**), 87% (**P3**) and 88% (**P4**), respectively. Even though the host polymer emission is also present to some extent in the EL of the copolymers, it is largely suppressed in EL compared to the PL (and in fact nearly completely suppressed in **P2** devices). Such suppression (compared to the PL) is due to the energy-selective injection, trapping and transport of charges via the NIR moieties, and subsequent formation of excitons at such sites (which effectively act as traps). Residual visible EL from **P3** is thus easily reconciled by taking into account the relatively high voltage needed for such a spectrum (60 V) that would also enable some degree of charge injection and transport via the host. Additionally, we note that spectra in Fig. 3.3b are normalised, thereby amplifying the visible spectral region for those devices that are less efficient in the NIR (as suggested by the higher noise levels of **P3** and **P4** spectra compared to that of **P2**).

Finally, we report a summary of the PLEDs characteristics in Table 3.1 and Table 3.2, and the current-radiance-voltage characteristics in Fig. 3.3b. We find that the best results are obtained for the devices incorporating the low-content S-based DAD units (1%, **P2**), for which we achieve a maximum EQE of 0.091%, an irradiance of 291 $mW \cdot m^{-2}$ (measured at 20 $mA \cdot cm^{-2}$), and most importantly, with nearly pure NIR emission peak-

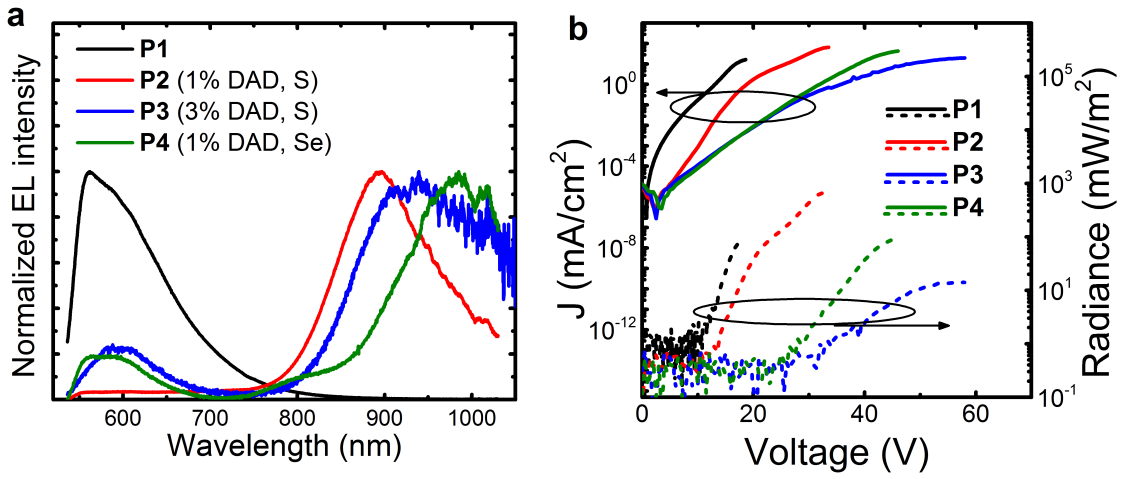

Figure 3.3: **a**, EL of the polymers taken at 20 V (**P1**), 33 V (**P2**), 60 V (**P3**) and 42 V (**P4**). **b**, PLEDs characteristics: current density and radiance versus voltage. The active layer thickness is ∼100 nm and the device area is 3.5 mm^2. Ref. [72] - Reproduced by permission of The Royal Society of Chemistry.

Table 3.1: Summary of PLEDs performance. [a]Intercept of the I-V curve with the x-axis in a semi-log plot. [b]Measured at 20 mA/cm^2.

Polymer	Max EQE (%)	V^a_{on} (V)	Radiance[b] (mW/m^2)
P1	0.037 ± 0.008	9.0 ± 0.8	98 ± 13
P2	0.091 ± 0.004	14.3 ± 2.9	291 ± 9
P3	0.006 ± 0.002	28.1 ± 1.1	16 ± 2
P4	0.018 ± 0.004	23.5 ± 1.5	58 ± 10

Table 3.2: Summary of PL and EL emission. [a]Defined as λ>700 nm.

Polymer	NIR PL peak (nm)	% PL in NIR[a]	NIR EL peak (nm)	% EL in NIR[a]
P1	-	-	-	-
P2	890	31	895	95
P3	927	24	939	87
P4	1000	21	990	88

ing at 895 nm (95% >700 nm). These results are among the best reported in the literature for a single active layer NIR PLED at such a long wavelength [84, 87, 90, 93, 94]. Regrettably, although perhaps not surprisingly, at 3% DAD loading the external quantum efficiency decreases significantly (from 0.09 to 0.006%), whereas the turn-on voltage (V_{on}) increases from 14.3 V for **P2** (1% DAD) to 28.1 V for **P3** (3% DAD). The increased driving voltage is easily attributed to an increased number of traps, related to the higher concentration of DAD units, which have lower energy gap compared to **P1**. In addition we attribute the EQE reduction to the expected aggregation of the DAD units, which is also corroborated further by the previously-discussed PL red-shifts. A similar trend has also been reported for other low-gap polymers copolymerized with a wide-gap host. [90, 102] Interestingly by comparing **P2** and **P4**, we are also able to get an insight into the influence of the exchange of a sulphur atom for selenium as a strategy to achieve NIR emission at longer wavelengths. We notice again that such a substitution leads to a decreased EQE and an increased V_{on}. However we point out that despite the V_{on} is disappointing, not only is Se substitution a better approach for increasing the wavelength of the emission than increasing DAD loading, but it also gives one of the most efficient devices at $\sim$1 μm reported to date for a polymer.

We can also compare **P2** to a similar and previously reported polymer, where the only difference is that in the previous study a branched alkyl chain (-$CH(C_8H_{17})_2$) was used on the host polymer whereas in this thesis we used the straight alkyl chain ($C_{16}H_{33}$) [93]. We can see that in this study, NIR PLEDs constructed from **P2** suffer from slightly higher turn-on voltages, and a factor of 3 lower EQE (0.09 % vs. 0.27 %). Thus, in comparing these two host polymers, it is surprising that the increased order, luminescence and higher (and more balanced) mobility provided by the straight alkyl chain ($C_{16}H_{33}$) on the host polymer, as characterized previously [93], did not result in the best host polymer for NIR PLEDs. Interestingly, the emission for the PLED based on **P2** is at 895 nm, which is red-shifted 10 nm compared to the previous study using the branched alkyl chain (885 nm). This supports the idea that lower order in the previous system likely prevented some aggregation of the NIR-emitting segments, resulting in

higher performance. Even though the lower and unbalanced mobilities of the branched alkyl side-chains would have suggested higher resistance in the devices, we observe no significant differences in the operating voltages of devices when compared to the devices using linear side-chain host polymers [93]. This suggests that charge trapping on the low gap DAD segments is the dominant source of resistance in these devices.

3.5 Conclusions

In summary, we have characterised the NIR emission of low-gap DAD units copolymerized with a wider gap phthalimide-thiophene polymer. PLEDs based on copolymers with 1% DAD loading give the best efficiency (∼0.09%) and EL peaking at 895 nm. We show that the copolymerization is a successful strategy to obtain almost pure NIR EL (up to 95% of the overall emission) for benzothiadiazole-based polymers.

By varying the loading of the DAD moieties it is possible to shift the emission further into the NIR however at a cost of lowered PLED efficiency because of increased aggregation. As an alternative and effective approach to shift the emission into the NIR (up to 1000 nm) we report the use of Se containing materials, that produce a lower impact on PLEDs EQE and driving voltage when compared to S-based copolymers with a higher DAD loading.

We have also demonstrated that in using the phthalimide-thiophene copolymer as a host polymer for NIR PLEDs, the more disordered system using the branched alkyl chain (C_8H_{17} vs. $C_{16}H_{33}$) results in better performing NIR PLEDs.

In addition, we consider that there should be significant margins of improvements for the spectral purity by further engineering the chemical design of these copolymers so as to provide lower-energy-gap host units, and thus ensure better spectral overlap, and more efficient energy transfer to the NIR moieties.

4 Near-infrared electroluminescence from exciplexes

Electronic processes at the heterojunction between chemically different organic semiconductors are of special significance for devices such as LEDs and OPV cells (see section 1.3.2). Here, we report the formation of an exciplex state at the heterojunction of an electron-transporting material, a functionalized hexaazatrinaphthylene, and a hole-transporting material, poly(9,9-dioctylfluorene-alt-N-(4-butylphenyl)diphenylamine) (TFB). The energetics of the exciplex state leads to a spectral shift of ∼1 eV between the exciton and the exciplex peak energies (at 2.58 eV and 1.58 eV respectively). LEDs incorporating such bulk heterojunctions display complete quenching of the exciton luminescence, and a nearly pure near-infrared electroluminescence arising from the exciplex (at ∼1.52 eV) with >98% of the emission at wavelengths above 700 nm at any operational voltage.

Material were received from Dr. Sunil Choudhary in the group of Prof. Aurelio Mateo-Alonso (formerly at Freiburg Institute for Advanced Studies and now at Polymat University of the Basque Country) who also estimate the HOMO/LUMO levels. The following chapter is reprinted with permission from ref. [88].

4.1 Exciplexes in organic semiconductors

The electronic processes at organic semiconductor heterojunctions exploited in LEDs and photovoltaic cells are of crucial importance for the operation of such devices, and

have therefore been widely discussed in the literature [25, 107, 108]. In particular, excited states with charge-transfer character localized at the heterojunction, traditionally termed exciplexes (see section 1.1.2), have been exploited in white LEDs [109, 110], and exciplex/charge-transfer excitons energetics has been correlated specifically with the open-circuit-voltage in bulk heterojunction photovoltaic cells [111], and more generally with the device performance [47]. The nature of the exciplex state has also been extensively investigated for type-II heterojunctions incorporating a variety of polyfluorenes, and the tendency to form such exciplexes proposed as a general property of these systems [4,112]. Another conjugated semiconductor system that has been shown to support exciplexes [113] is the combination of 5,6,11,12,17,18-hexaazatrinaphthylene (HATNA) with TFB (Fig. 4.1a).

HATNA derivatives are promising electron-transport materials that have shown mobilities of up to 0.9 cm^2/Vs depending on substituents [114]. Recently, Choudhary *et al.* have reported a successful strategy to twist the otherwise planar structure of HATNA and to influence their properties by means of such distortions [115]. Distorted polycyclic aromatic hydrocarbons [116–121] have emerged as promising materials for OLED applications [95,122–124] since the twisted conformation substantially reduces intermolecular π-π interactions, leading to enhanced solubility and to a reduction of aggregation-induced quenching in the solid state.

Here, we focus our attention on one of such twisted derivatives of HATNA, that carries six (triisopropylsilyl)-acetylenyl substituents (HATNA*, Fig. 4.1b) [115]. The presence of rigid acetylenes with such large triisopropylsilyl (TIPS) groups in confronting positions forces the aromatic core to deviate from planarity, and to adopt a symmetrical propeller-like structure (Fig. 4.2a).

Interestingly, we find that HATNA* forms an exciplex at the interface with TFB (see Fig. 4.2b for the energy levels), which emits with a broad unstructured spectrum peaking at 1.58 eV, i.e. with a spectral red-shift of about 1 eV with respect to the exciton emission energy. In view of the growing interest in NIR materials and devices [84,87,90,102,125–127] along with the interesting optoelectronic properties of HATNA*,

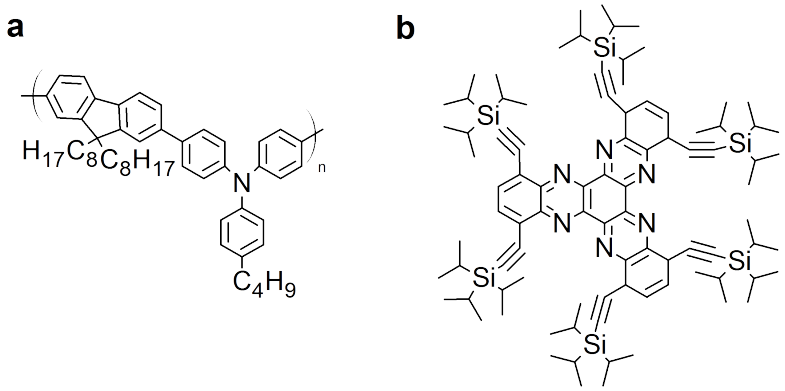

Figure 4.1: Chemical structure of TFB **a** and HATNA with TIPS substituents **b**.

we tested the HATNA*-TFB system in LEDs and found a nearly-pure NIR EL arising from the exciplex with >98% of the emission at wavelengths above 700 nm.

4.2 Experimental details

We looked at both blends and neat materials, starting our investigations with preparation of thin films (∼90 nm thick) of HATNA* by spin-coating (at 1.8 krpm for 120 s) a 2.5 wt.% toluene solution on a spectrosil substrate and, following the same procedure, of a thin film of TFB (American Dye Source, $M_w = 68000$ g·mol^{-1}) from a 2 wt.% p-xylene solution. To investigate the photophysics of the HATNA*-TFB heterojunction, we also prepared blends (1:1 weight ratio in toluene) thin films with the same solution concentrations and spin-speed (HATNA*:TFB). The steady-state PL spectra were recorded after exciting at 325 nm with a continuous wave He-Cd laser by means of an ANDOR-Shamrock spectrograph coupled with an ANDOR-Newton CCD unit. Time-resolved PL measurements were carried out with a TCSPC spectrometer as reported in section 2.1.1.

The LEDs were fabricated by spin-coating (4 krpm for 60 s and 5 krpm for 10 s) a 2.8 wt% of PEDOT:PSS (Sigma Aldrich) [61] water dispersion to a thickness of ∼80 nm over an ITO-coated glass pre-treated with oxygen plasma [62, 128]. The substrates were then baked at 150 °C for 10 min in a nitrogen atmosphere to remove residual water. The active layer, HATNA*:TFB 1:1, was deposited by spin-coating (1.8 krpm for 120

s) a 2.5 wt% toluene solution so as to obtain a thickness of ∼90 nm. Ca/Al electrodes (30 nm/150 nm respectively) were thermally evaporated under vacuum (∼10^{-6} mbar) on top of the active layer. The current-voltage-luminance characteristics were measured with a Keithley 2004 source-meter and a calibrated Si photodiode coupled to a Keithley 2000 multimeter. EL spectra were taken with the same ANDOR spectrometer described above (see section 2.2)).

4.3 HATNA/TFB exciplex characteristics

We report the absorption and emission spectra of HATNA*, TFB, and of the blend in Fig. 4.2c. We find that the absorption of the blend can essentially be reproduced by the superposition of the absorption spectra of the single components with little or no evidence of additional bands due to ground-state interactions between HATNA* and TFB.

The PL from HATNA* neat films (top panel of Fig. 4.2c) is clearly structured with vibronic peaks at 2.58, 2.38 and 2.18 eV (ΔE = 0.20 eV), and, interestingly, a 0-1 transition slightly more intense than the 0-0 one ($PL_{0-0}/PL_{0-1} \approx 0.99$). The latter suggests emission from weakly-bound excimers or aggregates [129] whose presence is also corroborated by the TCSPC data discussed below. Emission from TFB, which we report in the middle panel of Fig. 4.2c, is consistent with previous literature, confirms the slightly higher value of the energy gap of TFB compared to HATNA* (emission peak at 2.82 eV), and do not show any sign of aggregation in the form of a weaker 0-1 transition compared to the 0-0 one. Finally, we report the PL spectrum of the 1:1 blend in the bottom panel of the same figure (Fig. 4.2c). Remarkably, this displays a featureless emission band centred at 1.58 eV (λ_{max} = 785 nm) in addition to the emission of neat HATNA* (2.0-2.8 eV) and a residual TFB emission. We note that the HATNA* emission in the blend is characterized by a much stronger 0-0 transition ($PL_{0-0}/PL_{0-1} \approx 1.06$) than in the neat HATNA* thin film, consistently with the expected suppression of aggregation as a result of embedding HATNA* in TFB [130,131]. Emission from TFB is nearly completely suppressed, as expected, as a result of efficient energy transfer from

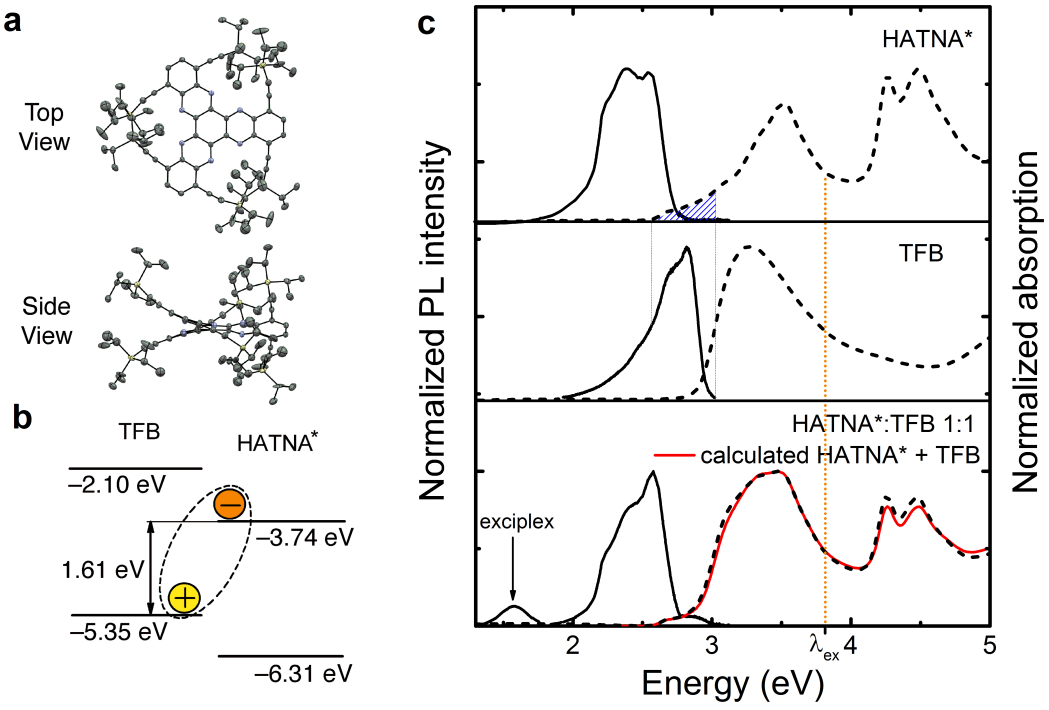

Figure 4.2: **a**, Top and side views of the crystal structure of HATNA* (A. Mateo-Alonso). **b**, Energy levels of the HATNA* (HOMO=6.31 ± 0.10 eV, LUMO=3.74 ± 0.10 eV) and TFB (HOMO=5.35 ± 0.11 eV, LUMO=2.11 ± 0.20 eV) estimated by cyclic voltammetry and optical absorption. The exciplex formation and binding energy is also schematically shown. **c**, Absorption (dashed line) and emission (solid lines) spectra of thin films of TFB, HATNA* and HATNA*:TFB 1:1 weight ratio normalized to the maximum value. The linear combination of the TFB and the HATNA* spectra (red solid line) is superimposed to the blend absorption spectrum. The PL is excited with a 3.8 eV (325 nm) He-Cd laser. The shaded area (blue) indicates the spectral overlap between TFB emission and HATNA* absorption. Reprinted with permission from ref. [88]. Copyright 2014, AIP Publishing LLC.

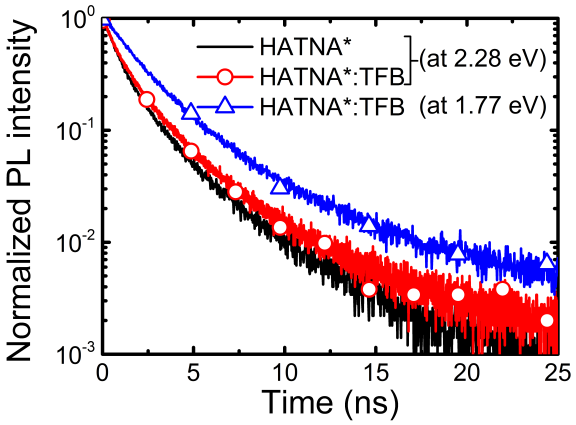

Figure 4.3: Photoluminescence temporal decays of thin films of HATNA* (black curve) and HATNA*:TFB blend (red curve with empty circles) taken at 2.28 eV (545 nm) and HATNA*:TFB blend (blue curve with empty triangles) taken at 1.77 eV (700 nm). Reprinted with permission from ref. [88]. Copyright 2014, AIP Publishing LLC.

TFB to HATNA* (note that, although HATNA*s absorption spectrum is not very strong at low energies, this does extend so as to provide a significant overlap with emission from TFB).

We assign the emission at 1.58 eV to an exciplex state formed between the HATNA* and TFB and confirm via TCSPC (Fig. 4.3) that luminescence from such a state is indeed much longer-lived (∼15 ns) than from the individual compounds (3 ns or less though non mono-exponential). More precisely, we report in Table 4.1 the results obtained when fitting the characteristics of Fig. 4.3 with a bi-exponential function (for the emission in the 2.0-2.8 eV region) and three-exponential function (for the emission at 1.58 eV). For HATNA* neat films we find time constants of 0.9 and 3.0 ns, respectively, and we assign them to an exciton and an excimer/aggregate state respectively. The relative weight of the excimer/aggregate lifetime decreases in favour of the exciton when HATNA* is blended with TFB, consistently with the observation and interpretation of the higher PL_{0-0}/PL_{0-1} ratio found in the spectra (Fig. 4.2c). The blend shows an additional long-lived component in the fluorescence decay taken at 1.77 eV, with a lifetime of 14.7 ns that we attribute to the exciplex state at the HATNA*:TFB interface.

Table 4.1: PL lifetimes for TFB, HATNA* and HATNA*:TFB for the emissions in the visible and near-infrared regions. Relative weight for the lifetimes is also reported. Reprinted with permission from ref. [88]. Copyright 2014, AIP Publishing LLC.

Compound	λ_{em}	τ_1 **(ns)**	τ_2 **(ns)**	τ_3 **(ns)**	**Relative weight** (τ_1:τ_2:τ_3)
TFB	2.70 eV	0.3	1.2	-	50:50:0
HATNA*	2.28 eV	0.9	3.0	-	47:53:0
HATNA*:TFB	2.28 eV	0.9	2.9	-	54:46:0
HATNA*:TFB	1.77 eV	1.6	3.7	14.7	43:45:11

4.4 Exciton-exciplex spectral shift

Remarkably, we observe a significant spectral shift between the 0-0 transition of the exciton (E_{0-0}) [59] and the exciplex emissions (E_x), of approximately 1 eV. Note that this value significantly exceeds those reported previously for a slightly different variant of HATNA-TFB (∼0.45 eV) [113] and for polyfluorenes heterojunctions (∼0.15-0.35 eV) [42].

Such a spectral shift (E_{0-0}-E_x) may be due to a substantial difference in either: (i) the relative positions of the frontier levels of the materials in agreement with our estimations (Fig. 4.2b, but note the large uncertainties on the energy levels) or, (ii) the stabilization energy (E_b) of the exciplex arising from the Coulombic attraction energy at the equilibrium distance and the ground-state repulsion energy [49], as well as from structural relaxation effects (see Fig. 1.7b). In regard of (i) we note that the TFB levels as measured in our laboratory are slightly different from those reported by Clark and collaborators [113], possibly due to differences in suppliers, molecular weights and other experimental details. Similarly, we expect even more significant differences between the energy levels of HATNA* and HATNA [113], owing to functionalization with TIPS-acetylenyl instead of dodecylthioethers. The extended conjugation with six acetylenes and their moderate electron withdrawing nature (in comparison to the electron donating nature of thioethers) shifts downwards the HOMO/LUMO levels of HATNA* with

respect to the vacuum level (albeit the energy gap is similar, ∼2.6 eV).

Indeed we note that control of chain microstructure is well known to influence the optical properties of conjugated semiconductors [132]. We can tentatively estimate the stabilization energy by subtracting the exciplex emission energy to the energy gap between the LUMO of the acceptor and the HOMO of the donor, to yield B=0.23 ± 0.16 eV. This value is comparatively high, e.g. in relation to binding energies of 0.07 eV previously estimated for the polyfluorenes and HATNA-TFB heterojunctions mentioned above, however we note the relatively large error bar. Indeed, given the large uncertainties generally affecting electrochemical measurement of the frontier levels (typically ±0.1 eV or so), we are not able to quantify with great accuracy the relative contribution of such effects to the shift [133], but we note that both are of the same sign. This is because a downward shift of the levels reduces E_{0-0}, and because the twisted conformation should increase the configurational relaxation energy. We can nevertheless speculate that the coulombic contribution should be similar for HATNA and HATNA*, as both materials are remarkably similar in their chemical make-up (no metallic or heavy atoms), and therefore dielectric properties and charge-screening should be similar. A strong correlation between geometry and electronic structure of conjugated polymers is both notorious and well-illustrated by a number of cases, such as in the case of substituted PPV derivatives carrying substitutions in the 2-3 positions [134–136].

4.5 Exciplex-based LEDs

The EL spectrum of the LEDs incorporating the blend as emissive layer and the device structure are reported Fig. 4.4a and the current and radiance versus voltage characteristics of a similar device are shown in Fig. 4.4b. Interestingly, the EL spectrum displays an emission at 1.52 eV (EL in the NIR > 98%) arising uniquely from the exciplex state whereas the emissions from the HATNA* and TFB excitons are completely suppressed at any operational voltages. This is in line with expectations, owing to the energy-selective nature of the charge transport processes in organic semiconductor, and the very nature of the exciplex/CT state that in EL has to form from combination of electrons travelling

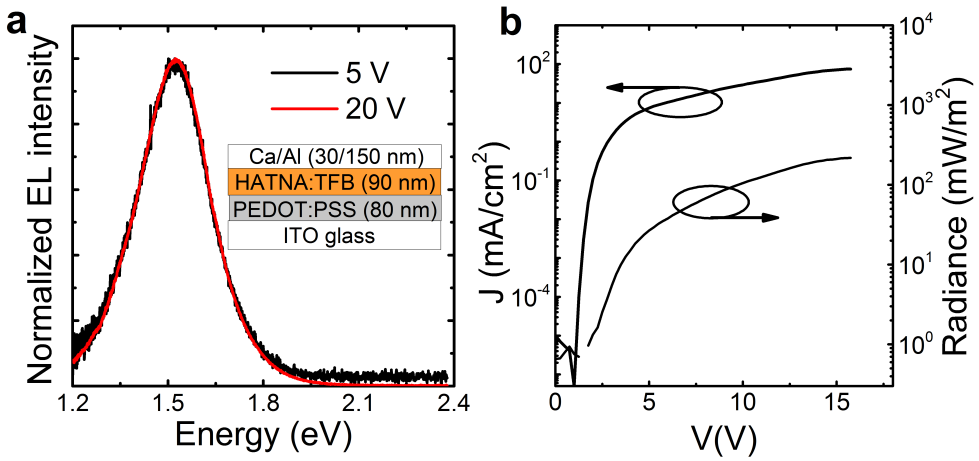

Figure 4.4: **a**, Electroluminescence spectrum of HATNA*:TFB 1:1 LED taken at 5 V (black curve) and 20 V (red curve) **b**, Current-voltage-luminance characteristics of HATNA*:TFB 1:1 LEDs. The LED structure is reported in **a**. Reprinted with permission from ref. [88]. Copyright 2014, AIP Publishing LLC.

(preferentially) in the HATNA* phase and holes in the TFB phase. Purity of the NIR EL emission provides good evidence of both the existence of percolating phases of either components, and of the preferential transport of oppositely-signed charge carriers in each of them. Importantly, it also provides excellent confirmation of the good stability of the exciplex at the interface.

The LEDs show a relatively low turn-on voltage of 2.0 ± 0.3 V (defined as the intercept of the I-V curve with the x-axis in the semi-log plot) and a radiance of 0.041 ± 0.003 mW·cm^{-2} (measured at 100 mA·cm^{-2}). The EQE for the device is 0.035 ± 0.005%. Although this might seem low compared to state-of-the-art visible LEDs, it is in fact within expectations, owing to the general increase of the non-radiative rate for decreasing energy gaps (the energy-gap law) [137]. EQEs of 0.02-0.05% have in fact been reported for polymer-based LEDs with emission at 1.48 eV (850 nm) and lower energies [101,138].

4.6 Conclusions

In conclusion, we have demonstrated the formation of an exciplex state at the HATNA*/TFB heterojunction that emits at 1.58 eV with a lifetime of 14 ns. NIR emission is achieved thanks to a large spectral shift of ∼1 eV between the exciplex and the exciton emissions. We observed NIR-pure and voltage-independent exciplex EL with >98% of the emission in the NIR with a EQE of 0.035% in line with best performing polymer-based LEDs with exciton emission in a similar wavelength range.

We demonstrate that exciplexes are also a viable route to obtain NIR emission. With a careful choice of the relative positions of the frontier levels of two materials that support exciplex it is possible to tune to emission wavelength.

5 Electrophosphorescence from a polyfluorene-Pt(II)porphyrin copolymer

A series of polyfluorene based polymers with a range of weight percentages of a platinum(II) containing porphyrin, **MPP**(**Pt**), were synthesized and incorporated into OLEDs. All polymers showed emission predominantly in the red/NIR region with only those polymers with porphyrin of less than 2 wt% showing residual tails at wavelengths lower than 600 nm, indicating increased emission from the porphyrin as the loading increases. The 2 wt% loading of **MPP**(**Pt**) gave the highest efficiency LED (0.48%).

Materials were received from David Freeman from the group of Dr. Hugo Bronstein (University College London).

5.1 Phosphorescent emitters

Phosphorescent emitters are of great interest in OLEDs due to their potential to achieve near 100% internal quantum efficiency [56]. Upon incorporation of heavy metal atoms with strong spin-orbit coupling such as platinum (II) or iridium (III), radiative transitions from triplet states become feasible. Since the first investigation of the EL from Pt(II)-porphyrin complexes [33] and $Ir(ppy)_3$ [139], many groups have reported the use of such complexes in blend with a polymer host. However, phosphorescent dopant aggregation and phase separation are disadvantages of blend architecture, due to the increased phosphorescent quenching rate [140, 141]. While synthetically more challenging, copolymerization overcomes these disadvantages [142, 143]. Having the dopant covalently bonded to the polymer will both increase the rate of energy transfer and reduce

loss processes by maintaining the absorbing and emitting moieties at fixed distance, thus preventing intermolecular interaction between dopant molecules. Solubility of the whole system is also increased facilitating low-cost solution-processed device fabrication. In particular, the incorporation of Pt(II) complexed porphyrins, promising candidates for deep-red phosphorescent OLEDs [144], into host polymers has been demonstrated to be a viable route, i.e. as a side chain in 2-methoxy-5-(20-ethylhexyloxy)-1,4-phenylene vinylene (MEH-PPV) [145–147]. Still few investigations have been reported for the incorporation of the Pt(II)-porphyrin directly in the polymer backbone [148–150]. Of the few previously reported polymers, porphyrins are generally incorporated by the β-pyyrollic position [148, 150]. Meso incorporation into a polyfluorene polymer has previously been achieved by Xiang but was studied only in the context of oxygen sensing and was synthesized via a less controlled (compared to Suzuki) Yamamoto reaction [149]. Here we investigate the electroluminescence and the steady-state and time-resolved photoluminescence of a Pt(II)-porphyrin, dimesityl diphenyl porphyrin platinium (**MPP(Pt)**) incorporated in a polyfluorene host polymer, poly(9,9-di-n-octylfluorenyl-2,7-diyl), (PFO). The phosphorescent dopant is covalently linked to the fluorescent host via phenyl groups (**PF − MPP(Pt)**).

5.2 Experimental details

The synthesis of the polymer has been reported elsewhere [151]. **MPP(Pt)** was incorporated with weight percentages of 0.5%, 1.0%, 2.0% and 5.0% into **PF − MPP(Pt)** and labeled **P1**, **P2**, **P3** and **P4** respectively), see Fig. 5.1a.

The optical properties of the copolymers have been investigated in the solid state. We deposited a 100 nm thick film for each compolymer via spin coating (1.8 krpm) a 2 wt% toluene solution over a Spectrosil fused silica substrate. The steady-state PL spectra were recorded after exciting the PL with a 405 nm diode laser with an ANDOR Shamrock spectrograph coupled with an ANDOR Newton CCD unit. Time-resolved PL measurements were carried out with a TCSPC spectrometer as described in section 2.1.1.

The PL efficiency was measured using an integrating sphere method (see section 2.1.2).

The copolymers **P1**, **P2**, **P3** and **P4** were also tested in PLED devices as the active layer (see section 2.2). OLEDs were fabricated by spin-coating (4 krpm) a 2.8 wt% dispersion in water of PEDOT:PSS (Sigma Aldrich) to a thickness of a 80 nm over an ITO-coated glass pre-treated with oxygen plasma (10 min at 10.2 W). The substrates were then baked at 150°C for 10 min in a nitrogen atmosphere to remove residual water. The active layer was deposited by spin-coating (2 krpm) a 2 wt% toluene solution to obtain a thickness of 100 nm. Ca/Al electrodes (30 nm/150 nm respectively) were thermally evaporated under vacuum, at 10^{-6} mbar) on top of the active layer. Current-voltage-radiance characteristics were measured with a Keithley 2004 source meter and a calibrated Si photodiode (wavelength range of 200-1100 nm) coupled with a Keithley 2000 multimeter, EL spectra were taken with the ANDOR spectrometer described above.

5.3 Deep-red phosphorescence

We report the absorption and emission spectra for the copolymers thin films **P1-P4** in Fig. 5.1b and Fig. 5.1c respectively. The copolymers show an intense featureless band at 380 nm due to the absorption of the PFO host polymer. In addition, the samples show two features at about 512 nm and 540 nm that we attribute to the Q-bands of the metalloporphyrin [152]. These bands increase in intensity as the concentration of **MPP**(**Pt**) increase and are clearly distinguishable for loadings as low as 1%.

Interestingly, given the small dopant loading, the PL spectra show a dominant emission in the red and NIR region with three components at about 665 nm, 735 nm, 805 nm and an emission shoulder at 645 nm that we assign to the **MPP**(**Pt**) segment. The copolymers also present a lower intensity emission at lower wavelength at about 442 nm, 467 nm and 497 nm that is attributable to the PFO. Interestingly, when increasing the porphyrin content, the intensity of these peaks reduces relative to the porphyrin emission, therefore suggesting an efficient energy transfer from PFO to the porphyrin. Indeed, the good spectral overlap between the **MPP**(**Pt**) absorption and the PFO emission (Fig. 5.2a) corroborates this hypothesis: both the Soret band (peaking at 402 nm) and the Q-band of the Pt(II)-porphyrin significantly overlap with the PFO emission. We

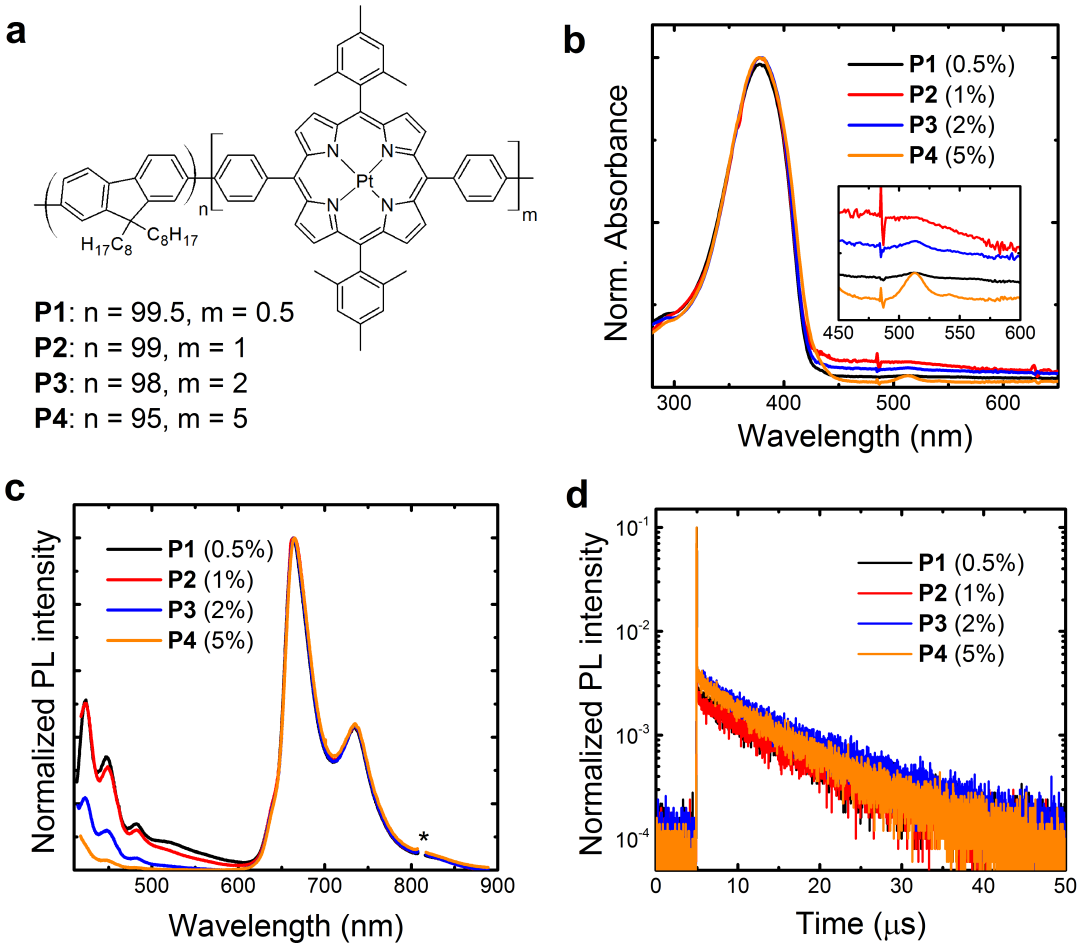

Figure 5.1: **a**, Chemical structure of the **PFO** − **MPP**(**Pt**) copolymers with different MPP-Pt loading: 0.5% for **P1**, 1% for **P2**, 2% for **P3** and 5% for **P4**. **b**, Normalized absorption spectra of the copolymers film on fused silica glass. The inset shows **MPP**(**Pt**) absorption features. **c**, Normalized PL spectra of the copolymers films. The * indicates the monochromator 2nd-order transmission of the excitation wavelength. **d**, PL time decay taken at the most intense peak emission wavelength of the **MPP**(**Pt**) (665 nm) following excitation at 371 nm.

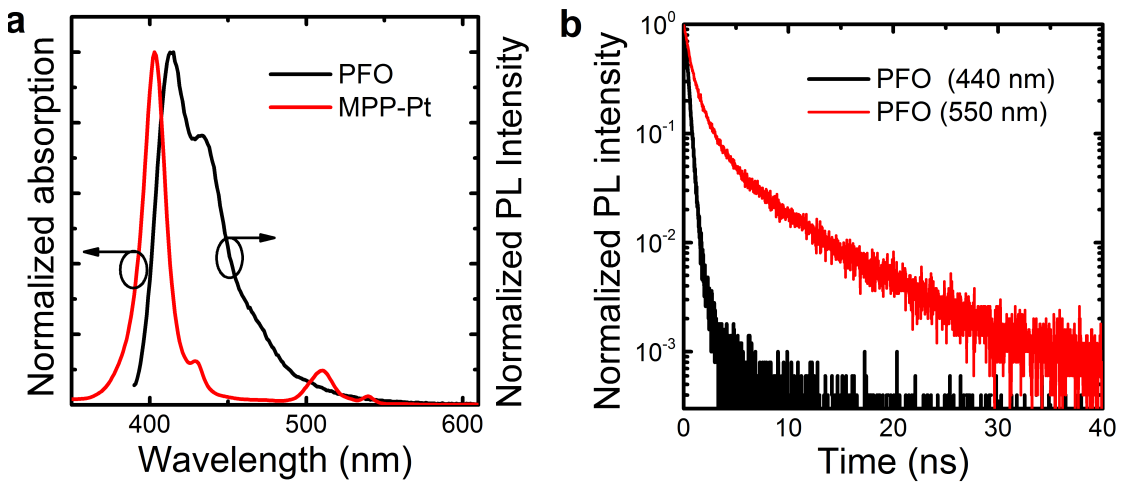

Figure 5.2: **a**, Spectral overlap between PFO fluorescence emission (in $CHCl_3$, black curve) and **MPP**(**Pt**) absorption (in toluene, red curve). **b**, PL time decay for the PFO host polymer taken at 440 nm (black curve) and 550 nm (red curve).

also note in Fig. 5.1c a weak fluorescence emission band between 500 and 600 nm that can be related to the presence of fluorenone defects or aggregates/excimers [153], whose presence is further validated by the TCSPC data.

In fact, the radiative lifetime of PFO taken at 550 nm (Fig. 5.2b) can be fit with a bi-exponential function yielding time constants of ∼400 ps and 6.6 ns that are consistent with PFO exciton and fluorenone excimer respectively [154]. The radiative lifetime taken near the peak emission wavelength of the PFO (440 nm) also confirms the presence of efficient energy transfer from the PFO to the porphyrins. In fact, the lifetime of the neat PFO of about ∼400 ps is reduced upon loading with the **MPP**(**Pt**) and drops below the instrument detection limit (∼150 ps). The PL lifetime taken at the emission wavelength of the **MPP**(**Pt**) emission (665 nm) are reported in Fig. 5.1d. The copolymers show lifetime decays in the microsecond scale indicating the triplet nature of the emissive state. Specifically, we found time constants of 9.3 μs (**P1**), 9.2 μs (**P2**), 9.2 μs (**P3**) and 8.6 μs (**P4**).

The PL efficiency is around 4.9% for the **MPP**(**Pt**) loading of 0.5% (**P1**) and slightly

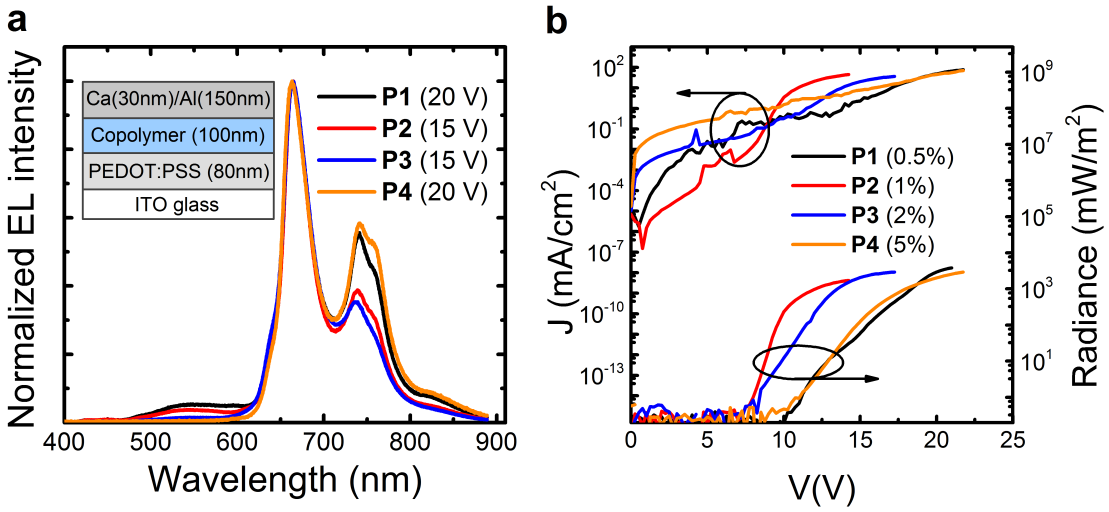

Figure 5.3: **a**, Normalized EL spectra for the copolymers. The LED structure is reported. **b**, LEDs characteristics: current density and radiance versus voltage. The active layer thickness is ∼100 nm and the device area is 3.5 mm^2.

decreases (to 4.5%) upon increasing the amount of porphyrin up to 2% (**P2** − **3**). A drop to a PL efficiency of 2.5% is seen for higher porphryin content. The trend is consistent with the lifetime values suggesting an increase of the non-radiative deactivation of the exciton for porphyrin concentrations higher than 2%. Note that although these values may appear relatively low in absolute terms, they are comparable to values reported in the literature for similar polymers [150].

5.4 Electrophosphorescence

We also incorporated the copolymers in LEDs with ITO/PEDOT:PSS as anode and Ca/Al as cathode. We report the EL spectra in Fig. 5.3a in which we note that the copolymers display an emission predominantly in the red and NIR region.

In particular, the EL of **P1** peaks at 665, 736 and 818 nm with a shoulder at 642 nm. We do not observe any shifts of the EL for higher **MPP**(**Pt**) loadings nor compared to the PL spectra. For copolymer **P1** and **P2**, however, we note a weak EL emission at

Table 5.1: Summary of PLEDs performance. [a]Intercept of the I-V curve with the x-axis in a semi-log plot. [b]Measured at 30 mA/cm^2.

Polymer	**EQE**^{a} **(%)**	$\mathbf{V}_{on}^{a}$ **(V)**	**Radiance**^{b} **(mW/m**^{2}**)**
P1	0.17 ± 0.01	10.7 ± 0.2	986 ± 61
P2	0.28 ± 0.04	7.6 ± 0.2	1486 ± 221
P3	0.48 ± 0.01	8.3 ± 0.3	2630 ± 38
P4	0.28 ± 0.04	9.3 ± 0.4	1390 ± 56

wavelength below 600 nm. When increasing the content of porphyrin the intensity of the emission tail decreases with little or no intensity left for loading above 1%. Such emission may be related to oxidative defects on the PFO [153] and to the emission from **MPP**(**Pt**) singlet state, as reported for similar Pt(II)-porphyrin complexes at 580 nm [155]. For MPP(Pt) loadings above 1%, copolymers show a pure electrophosphorescence (**P3** and **P4**).

The current-voltage and radiance-voltage characteristics are shown in Fig. 5.3b, and a summary of the LEDs performance is reported in Table 5.1. The 2% loading of **MPP**(**Pt**) (**P3**) gives the highest efficiency LED (0.48%) and light output (2630 mW·m^{-2}). The result is particularly promising compared to what has been reported in literature up to now, especially when taking into account that the LEDs are not optimized for charge collection and extraction [148, 150]. We note an overall increase of the performance (i.e. lower turn-on voltage, higher efficiency and light output) increasing the porphyrin loading up to 2%. However, the LEDs performance lowers when the loading exceed 5%. Given the partial overlap of the **MPP**(**Pt**) absorption with the PFO emission we speculate that the EL emission at low voltages is mainly due to charge trapping in the **MPP**(**Pt**) segment rather than energy transfer. However, upon a further increase of the applied voltage, charges can be injected directly into the PFO levels and can subsequently migrate to the **MPP**(**Pt**) moiety and contribute to the phosphorescence emission.

5.5 Conclusions

We have studied a series of conjugated copolymers containing **MPP**(**Pt**), a platinum(II) complexed porphyrin, directly into the PFO backbone. Emission of the polymers at 665 nm was shown to have a lifetime decay on the microsecond scale, indicating phosphorescence for all porphyrin containing polymers, with decreased fluorescence from the PFO backbone as the loading of **MPP**(**Pt**) was increased. The polymers were incorporated into OLEDs, and 2 wt% of **MPP**(**Pt**) was shown to have an efficiency of 0.48% and a light output of 2630 $mW \cdot m^{-2}$. Pure **MPP**(**Pt**) electrophosphorescence is achieved for loading as low as 2%.

6 Photophysics of PCBM single-crystals

PCBM ([6,6]-Phenyl C_{61} butyric acid methyl ester) is a highly soluble C_{60} fullerene derivative that is extensively used as electron acceptor in highly efficient bulk heterojunction solar cells. Here we report the PL of high-quality solvent-free PCBM crystals between room temperature and 4 K. Contrary to the PL spectra of amorphous of polycrystalline PCBMs, that of the single-crystals becomes very structured as the temperature is lowered disclosing several emission lines extremely well-resolved (minimum linewidth of $\sim$1.3 meV).

Crystals were grown in our group by Giuseppe Paternò. Quantum-chemical calculations supporting our experimental data were provided by Dr. Micheal Wykes (IMDEA, Spain) and Prof. David Beljonne (University of Mons). The fluorescence lifetime images of the single-crystals were taken in the frame of a collaboration with Dr. Liisa Hirvonen and Prof. Klaus Suhling (King's College London). Part of this chapter is reprinted with permission from [185]. Copyright 2015 American Chemical Society.

6.1 Crystalline PCBM

PCBM is currently the most important C_{60} derivative [156, 157], owing to the efficiency of charge transfer from nearby photoexcited molecular states, and therefore as the elective electron acceptor in highly efficient bulk heterojunction (BHJ) solar cells [158]. In spite of its relevance to organic optoelectronics, little attention has been dedicated up to now to PCBM's luminescent properties [159, 160] although they can provide a crucial insight into the fundamental energetics of this material, especially in its crystalline phase. Both the molecular packing and the details of the nanostructure of fullerene-based BHJs

have been shown recently to have a crucial impact on the device efficiency [161, 162]. OPV devices based on poly(3-hexylthiophene-2,5-diyl) (P3HT) and PCBM blends show better performance upon formation of aggregated phases in either components following thermal annealing [163]. In particular, PCBM aggregates have been recently proven to assist ultrafast long-range charge separation [164, 165]. However, the crystal structure of PCBM turns out to be strongly dependent on the solvent from which the crystals are grown and that is present in the latter as an inclusion [166–168]. Only recently, solvent-free PCBM single-crystals were reported with a monoclinic structure following solvent extraction in vacuum [169] or via a thermal treatment, [170] thereby allowing fundamental structure-property investigations without the solvent dependence [171]. In particular, crystallite geometries are fundamental to investigate the electronic states involved with charge separation [172]. Also, an accurate investigation of PCBM's luminescent properties, may lead to an unprecedented insight into the ordering and relative importance of the relevant excited states, and eventually of the overall electronic structure of this material, also a prerequisite for establishing accurate computational models.

Here we report the PL of PCBM both in the amorphous and crystalline phase. In particular, we investigate the solvent-free PCBM single-crystals as reported in [169] (see Fig. 6.1). The evolution of the emission for the single-crystal discloses a progressively detailed and better-resolved structure as the temperature is lowered down to 4 K.

6.2 Experimental details

PCBM (Sigma Aldrich purity >99%) was dissolved into chlorobenzene at a concentration of 20 mg·mL^{-1}. The solution was kept under stirring overnight at room temperature. Solvent-free PCBM single-crystals (see Fig. 6.1a) were prepared as previously reported [169]: a droplet of PCBM solution was deposited over a fused silica substrate and the solvent evaporated in air at room temperature. To remove any residual solvent molecules, the sample was dried under vacuum ($\sim 10^{-2}$ mbar) overnight.

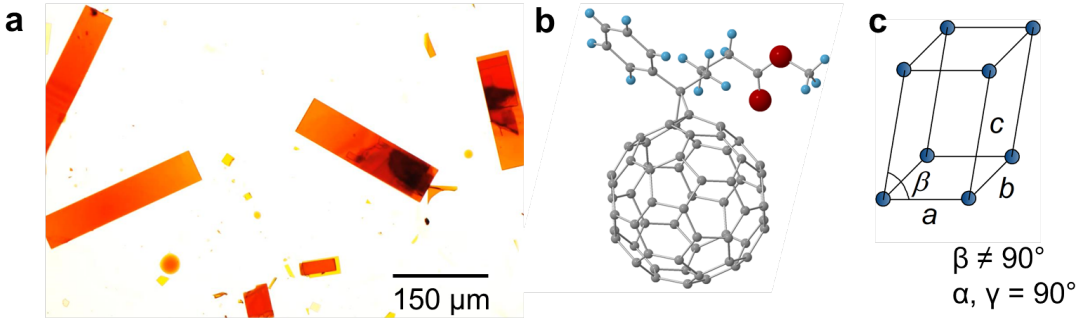

Figure 6.1: **a**, Optical micrograph of PCBM single-crystals. **b**, Chemical structure of the PCBM showing the orientation of side chain in the crystal structure. Carbon atoms are reported in grey, oxygen atoms in red and hydrogen atoms in blue. **c**, Schematic representation of the monoclinic lattice reported for solvent-free PCBM single-crystals.

We also prepared an amorphous film (∼100 nm) spin-coating the PCBM solution in chlorobenzene onto a fused silica substrate at 800 rpm. Furthermore we prepared a polycrystalline film (∼800 nm) drop-casting a droplet (100 μL) of PCBM solution over a fused silica substrate and let the solvent to evaporate in air at a constant temperature of 303 K. The powder XRD data are reported in the SI (Fig. 6.2). X-ray diffraction measurements were performed with a Rigaku SmartLab diffractometer (Rigaku, Tokyo, Japan), by using a Kα wavelength emitted by a Cu anode (0.154 nm). The measurements were carried out using a grazing incidence configuration (incidence angle = 0.5°) to reduce the background scattering from the substrate. We thank G. Paternò (UCL) for helping us with these measurements.

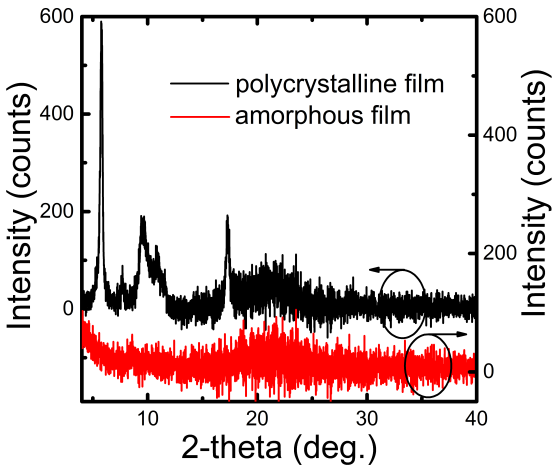

Figure 6.2: X-ray diffraction patterns for the polycrystalline (black) and amorphous (red) films. We thank G. Paternò (UCL) for the measurements. Reprinted with permission from [185]. Copyright 2015 American Chemical Society.

Variable temperature fluorescence was recorded using a Renishaw Raman System 1000 equipped with a He-Ne laser light source (λ_{ex} = 632.8 nm) and a CCD detector. To prevent the sample degradation we used low laser power at the crystal surface (∼0.1 mW). The Raman spectrometer was configured with a Leica optical microscope equipped with a Nikon SLWD M Plan 40x/0.40 objective. The spot size at the sample surface was ∼1-2 μm. Fluorescence spectra in the 4-300 K range were taken placing the sample in a Helium-cooled cryostat (MicrostatHe2, Oxford Instrument. Kindly borrowed from Dr. Guy Matmon).

Raman spectra were collected with a Renishaw InVia Raman microscope illuminating the samples with an argon ion laser (488 nm and 514 nm) and a 785 nm laser through a Leica N Plan 50x/0.75 objective. The laser power at the sample surface is 0.1 mW. The instrument was kindly offered on loan by the EPSRC Engineering Instrument Pool.

Fluorescence lifetime imaging microscope (FLIM) images of 256x256 pixels were obtained using a Leica TCS SP2 inverted scanning confocal microscope coupled with a Becker and Hickl TCSPC card SPC830. A pulsed diode laser at 467 nm (PLP-10 470, Hamamatsu) with a pulse duration of 90 ps and a repetition rate of 20 MHz was used as the excitation source. The emission was collected through a 680-720 nm filter onto a cooled PMC 100-01 detector (Becker and Hickl, based on a Hamamatsu H5772P-01 photomultiplier). We thank L. Hirvonen and K. Suhling (King's College London) for helping us with these measurements.

6.3 Steady-state and time-resolved PL

We compare the PL spectra at room temperature of PCBM amorphous films and the single-crystals in Fig. 6.3a. The single-crystal shows an emission band with two main components at 1.70 eV and 1.57 eV with a shoulder at 1.75 eV. The PL of the amorphous film is broader and slightly red-shifted with emission peaks at 1.67 eV and 1.55 eV with a shoulder at 1.72 eV. The apparent red-shift of the amorphous phase is somewhat unexpected compared to other systems [173] and may be due to scattering effects due to the presence of small crystallites in a relative low concentration (e.g. not detected by

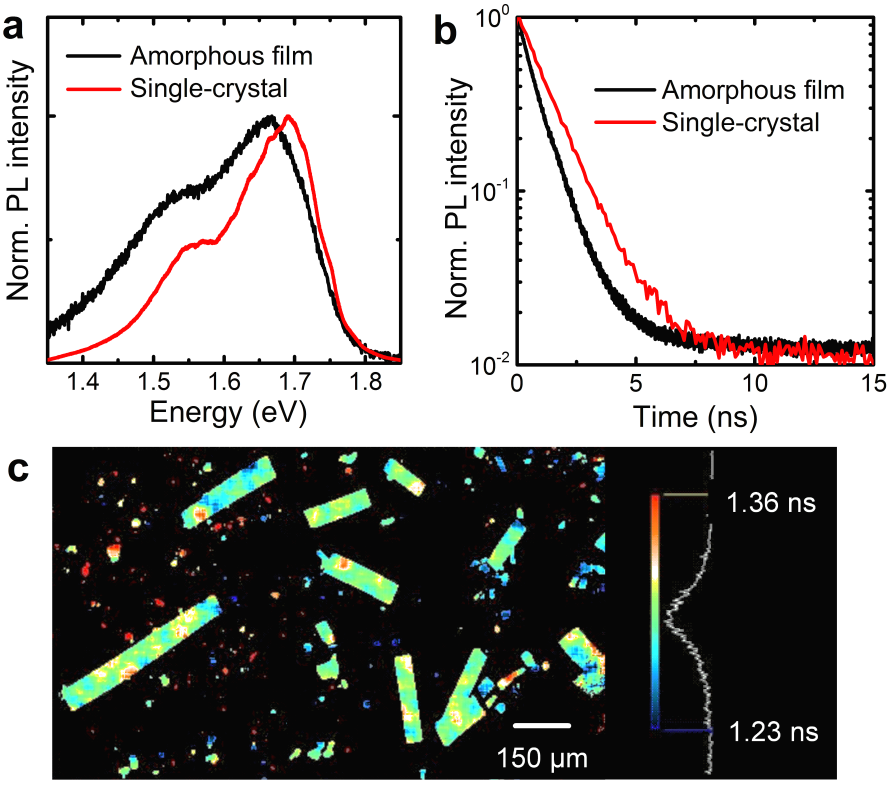

Figure 6.3: **a**, Steady-state photoluminescence spectra of amorphous film (black line) and single-crystals (red line). **b**, PL time decay for amorphous film (black line) and single-crystal (red line, averaged value over 19x19 pixels) taken at 1.75 eV (710 nm), following excitation at 2.64 eV (470 nm). **c**, Fluorescence lifetime image of single-crystals showing minor heterogeneities in lifetime values over the crystal surface (440x256 pixels). The colour bar indicates the distribution of the lifetime between 1.23 ns (blue) and 1.36 ns (red). We thank L. Hirvonen for the FLIM measurements.

the XRD).

In addition, we observe a pronounced difference between the two samples in PL time decay (Fig. 6.3b). The single-crystal is characterized by a mono-exponential decay with a time constant of 1.3 ns. Instead, the amorphous film shows a bi-exponential decay with time constants of 0.4 ns and 1.0 ns, with relative weights of 25% and 75% respectively, that is consistent with previously reported values [159]. The mono-exponential lifetime for the single-crystal suggests a high-quality crystal structure whereas the bi-exponential decay for the amorphous film corroborates further the hypothesis of a more disordered system (i.e. presence of crystallites).

We also analyse the spatial distribution of the PL decay rate for the single-crystals with a fluorescence lifetime imaging microscope (FLIM) and reported the data in Fig. 6.3c. The FLIM image shows minor (less than 0.05 ns) and random heterogeneities in lifetime values over the crystal surface.

6.4 Low-temperature photoluminescence

In Fig. 6.4a we report the fluorescence spectra of PCBM single-crystals as a function of temperature in the 4-300 K range. As the temperature is decreased, the PL emission undergoes an evolution with many more well-resolved transition lines than expected from the room temperature spectra. We only observe a minor temperature dependence of the relative intensities of such peaks. The only exceptions are observed for the peaks at 1.76 and 1.79 eV, whose intensity visibly decreases as the temperature is lowered (e.g. with respect to the peak at 1.73 eV). The peak at 1.79 eV completely vanishes for $T < 100$ K.

While most PCBM crystals emit as in Fig. 6.4a, in some cases we observed spectrally-shifted, and less well-resolved emission, although still highly-structured and with a similar temperature dependence. We report an example in Fig. 6.4b, and compare the 4 K spectra of the crystals of Fig. 6.4a-b in Fig. 6.5a. Here we note that a rigid shift in energy of about $\sim$35 meV of one of the spectra with respect to the another. Nevertheless, the distribution of the vibrational peaks is similar, suggesting that emission occurs from

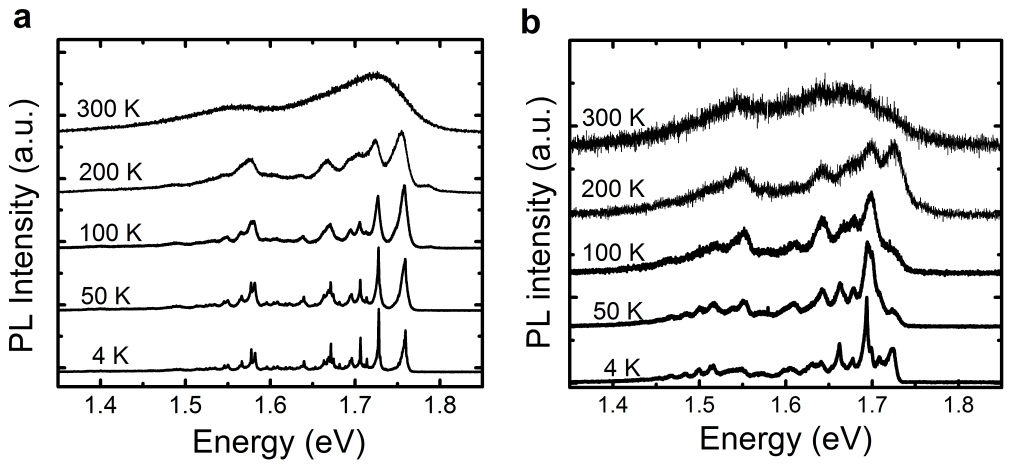

Figure 6.4: Normalized PL of the single-crystal as a function of the temperature (T=4-300 K) collecting emission from different single-crystals, **a** and **b** respectively. A highly-structured emission is noted at low temperature for both samples. Reprinted with permission from [185]. Copyright 2015 American Chemical Society.

similar types of excited states with different origins. We also observe small differences in relative peak intensities between the two spectra.

There are many potential explanations both for the red-shift and for the other subtle changes in the spectra. For example, these could be due to a morphological crystal defect which affects the state-mixing and hence spectral shape. Alternatively, it could be a chemically degraded PCBM – for example, it is well known that fullerenes can dimerize in the solid state upon exposition to UV and visible light [174] however we can rule out this possibility by means of the Raman spectra reported in Fig. 6.5b. Here, we see that the "pentagonal pinch" mode ($A_g(2)$) for the C_{60} cage peaks at 1464 cm^{-1} as reported for pristine (not dimerized) PCBM [175]. Therefore, we assign the red-shifted spectrum to an emission from a deep trap. Indeed, similar behaviour has been reported in C_{60} single crystals [176,177] with traps that were found to be red-shifted by 100 meV relative to bulk C_{60}.

The PL spectrum at 4 K shows very well-resolved emission lines with a minimum FWHM of 1.3 meV (i.e. 1.73 eV transition for crystal reported in Fig. 6.4a). Such a

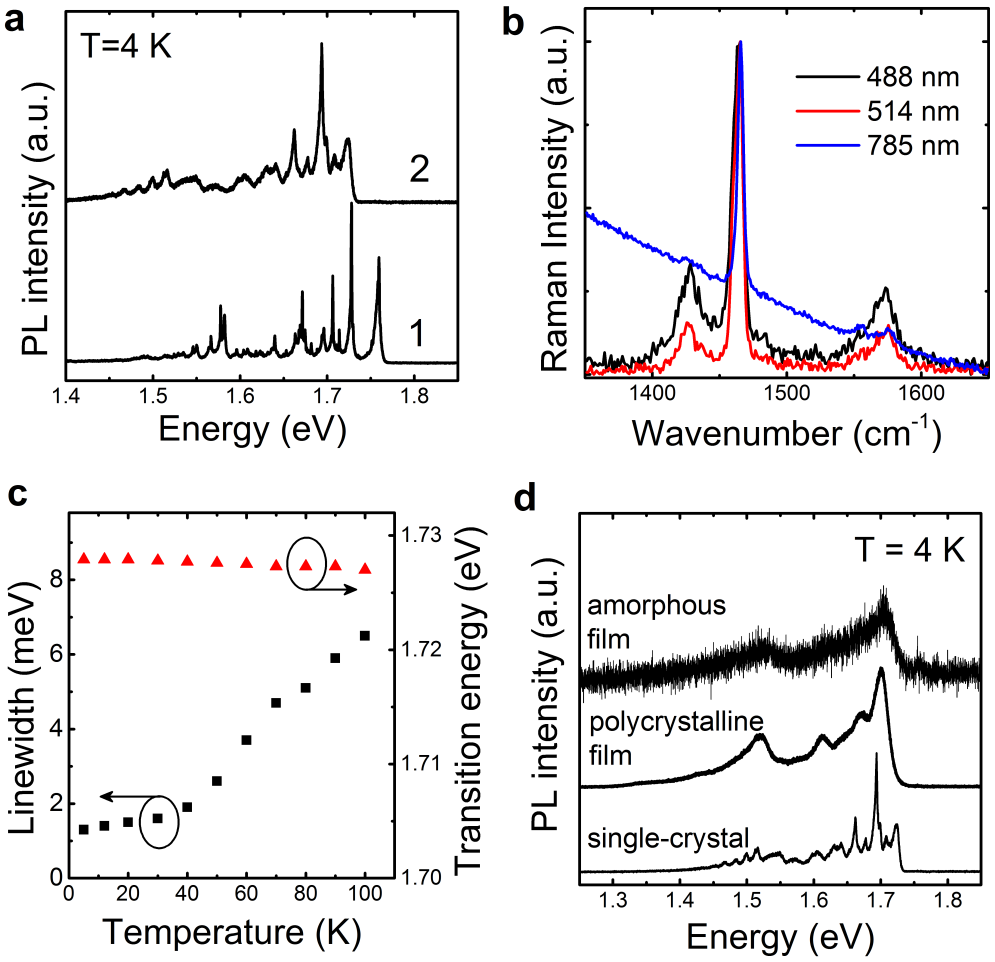

Figure 6.5: **a**, Normalized low-temperature fluorescence of two different single crystals: the rigid shift of about 35 meV of spectrum 2 with the respect to spectrum 1 is related to the presence of a trap. **b**, Normalized Raman spectra of PCBM single-crystals at different wavelengths (laser power at the sample surface of ∼0.1 mW). The strongest peak (pentagonal-pinch mode $A_g(2)$ of C_{60}) is at 1464 cm^{-1} for the 488 nm curve (black) and 1465 cm^{-1} for the 514 nm and 785 nm curves (red and blue respectively). **c**, Energy of the second well-resolved transition (at about 1.73 eV) for spectrum 1 and its linewidth FWHM dependence on the temperature. Above 100 K the broadening of the peaks prevents an accurate quantification of the linewidth. **d**, Low-temperature fluorescence of PCBM as amorphous film, polycrystalline film and single-crystal. A progressively better resolved PL structure is seen when increasing the crystallinity of the sample.Reprinted with permission from [185]. Copyright 2015 American Chemical Society.

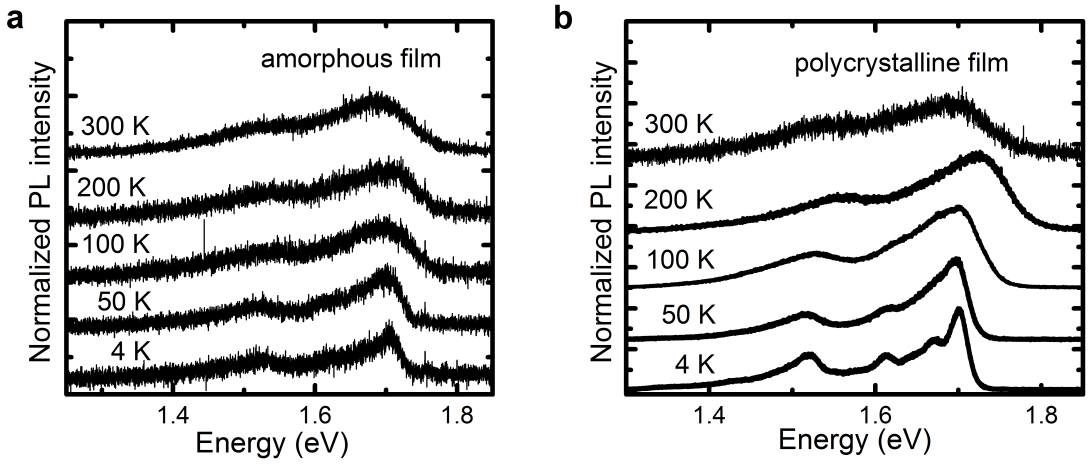

Figure 6.6: Fluorescence spectra as a function of temperature for the amorphous (**a**) and polycrystalline (**b**) films. Reprinted with permission from [185]. Copyright 2015 American Chemical Society.

narrow linewidth suggests a high-quality of the single-crystals. We report the temperature evolution (in the range 5 to 100 K) of both linewidth and spectral position of the peak at 1.73 eV. Interestingly, while there is only a marginal spectral shift of this peak (< 0.5 meV), the linewidth shows different behavior depending on temperature. Namely, the linewidth is nearly constant for $T < 40$ K, but increases more prominently and with a nearly linear dependence on temperature, for $T > 40$ K. We assign such a strong temperature dependence to a mostly homogeneous mechanism.

To obtain further insights into the effect of structural disorder on the PL spectra, we also consider the low-temperature PL spectra of the crystals and of amorphous and polycrystalline films (Fig. 6.5d) and compare them with those at room temperature (Fig. 6.6).

As expected, we observe only minor differences between the low-temperature (4 K) and room temperature PL spectra of the amorphous film. In particular only a minor sharpening of the emission peaks is noted when lowering the temperature. The polycrystalline film shows an increased number of better-resolved peaks at 4 K, compared to the room temperature spectrum, and with respect to the amorphous film, even though

a relatively broad band is still visible. We also note that the peak structure only starts to appear below 50 K.

We emphasize that, even if less structured than the single-crystal spectrum, the 4 K spectra of amorphous and polycrystalline samples also feature a progressive, albeit moderate, sharpening of the linewidths, highlighting the fact that the structural inhomogeneity does not translate into a preponderant energetic disorder in PCBM (i.e. preventing the observation of any linewidth reduction).

6.5 The case of C_{60} and the analogies with PCBM

A similar trend in the PL spectrum as a function of the temperature for amorphous, polycrystalline and single-crystal structures has been reported for the C_{60} fullerene [176]. In particular, the many transitions seen for the C_{60} single-crystal has been interpreted as Herzberg-Teller (HT) induced emission [178, 179]. Indeed, transitions for C_{60} from the three lowest quasi-degenerate excited states (of T_{1g}, T_{2g} and G_g symmetry) to the ground state (A_g) are symmetry forbidden. Thus, emission from such states happens through vibronic coupling with a higher electronic state of u-symmetry that has symmetry-allowed transitions to the ground state. This process is often referred to as intensity borrowing HT mechanism. Basically, two electronic excited states are coupled via a (totally symmetric) vibration which induces a borrowing of the oscillator strength from the higher electronic state (with *ungerade* symmetry) to the vibronic level of the lower excited state (with *gerade* symmetry) [180]. Radiative transitions to the ground state arise from the vibronically induced HT false origins of each HT-coupled vibration, each convoluted with its own Franck-Condon (FC) progression. Furthermore, the T_{1g}, T_{2g} and G_g excited states have degenerate components that undergo a geometrical distortion that removes the degeneracy and thus lowers the symmetry. This effect is known as the Jahn-Teller (JT) effect and transitions arising from vibronic coupling to non-totally symmetric JT modes are seen in the low temperature spectra of C_{60} [178]. The selection rules for the transitions are related to the truncated icosahedron shape of the C_{60} molecule that belongs to the I_h point group [181].

Sassara et al. reported a thorough study of the electronic states and transitions for C_{60} including assignments of vibronic transitions based on a comparison of simulated and experimental spectra measured in inert Ar and Ne matrices at 4K [178]. The simulated vibronic envelopes of each state were constructed from HT, FC and JT couplings obtained from quantum chemical calculations. This showed that emission occurred from a state of mixed T_{1g}, T_{2g} and G_g character. The fractional character (weight of each states vibronic envelope in the spectrum) was found to vary with the environment; the (T_{1g}, T_{2g} and G_g) weights in the emissive state were found to be 36%, 56% and 7% in Ne and 50%, 25% and 25% in Ar.

Upon derivatization of C_{60} to form PCBM the I_h symmetry is lost due to the side chains. The side chain also affects the crystal packing. In fact, solvent-free PCBM single-crystals belong to the monoclinic crystal system [169, 170] whereas C_{60} single crystal has a cubic lattice [182]. The functionalization of the C_{60} core and the associated loss of symmetry results in a perturbation of the π-system and removes the degeneracy of the low-lying excited states present in C_{60}. However, despite the lower molecular symmetry and differencing crystal symmetry, we note many similarities between the low-temperature PL spectra of PCBM and C_{60} single crystals. Given these similarities we tried to apply the Sassara's model to PCBM.

6.6 Simulated photoluminescence spectrum

Quantum-chemical simulations based on Sassara'a model were performed by M. Wykes (IMDEA, Spain) and D. Beljonne (University of Mons) and reported in Fig. 6.7. We are able to describe such an evolution quantitatively by using a combined approach in which Herzberg-Teller-induced fluorescence is modified by the concomitant presence of Jahn-Teller and Franck-Condon effects.

Unfortunately, the modeling approach applied to C_{60}, namely calculating the vibronic envelopes of each pure diabatic excited state (T_{1g}, T_{2g} and G_g) cannot be readily applied to PCBM. In PCBM, the lower symmetry imposes a mixing of states, preventing study of the underlying higher-symmetry diabatic states. The (multiply degenerate) T_{1g}, T_{2g}

and G_g states of C_{60} are replaced with 10 quasi-degenerate states of mixed character in PCBM, too close in energy to allow for reliable prediction of state ordering and mixing by quantum chemical methods that can be applied to systems of such size. However, given the remarkable similarity of PCBM spectra with those of C_{60} we wonder whether the Sassara's model of C_{60} PL might, with some slight empirical adjustments, also allow for interpretation of the PCBM single-crystal PL spectra. This makes sense if one considers the pendant group in PCBM as a perturbation to the C_{60} electronic structure. Quantum chemical calculations support this hypothesis, showing that the electron density for the HOMO and LUMO of the PCBM is mostly located on the C_{60} core with only little density residing on the side chain [183, 184].

Sassara's model is thus hand-tuned in several incremental steps. The detailed procedure is reported in reference [185], here we provide a general outline. Firstly, the electronic origin is set to 14200 cm^{-1} to coincide with the first peak in PCBM PL spectrum (we refer to the 4 K spectrum in Fig. 6.4a). This is close to the value of 14629 cm^{-1} observed in C_{60} single-crystals [186] yet significantly red shifted relative to the electronic origins of C_{60} in Ar and Ne matrices at 15487 and 15627 cm^{-1}, respectively [178]. Also, the model of Sassara *et al.* does not include the 0-0 transition for C_{60} (nor FC progressions built upon it). However, the lower molecular symmetry in PCBM means that the 0-0 is not strictly symmetry-forbidden in PCBM. An electronic origin approximately 2.5 times more intense than the most intense HT false origin is thus added to the vibronic envelope of each state with FC and JT progressions built on top. Following this, the impact of variation in the weights of the T_{1g}, T_{2g} and G_g states is explored. It is then noted that none of the peaks of the T_{1g}, T_{2g} and G_g vibronic envelopes (placed on an origin of 14200 cm^{-1}) have a peak at 13770 cm^{-1}. However, the vibronic envelope of the H_g state, for which the vibronic coupling parameters are also listed in reference [178], do feature a transition with non-negligible intensity at that energy once placed at an origin of 14200 cm^{-1}. Furthermore, it is noted that the vibronic envelope of the H_g state is quite similar to that of the G_g state and could also account for the band in the PCBM spectrum at 13500 cm^{-1} not present in either the T_{1g} or T_{2g} vibronic envelopes. This

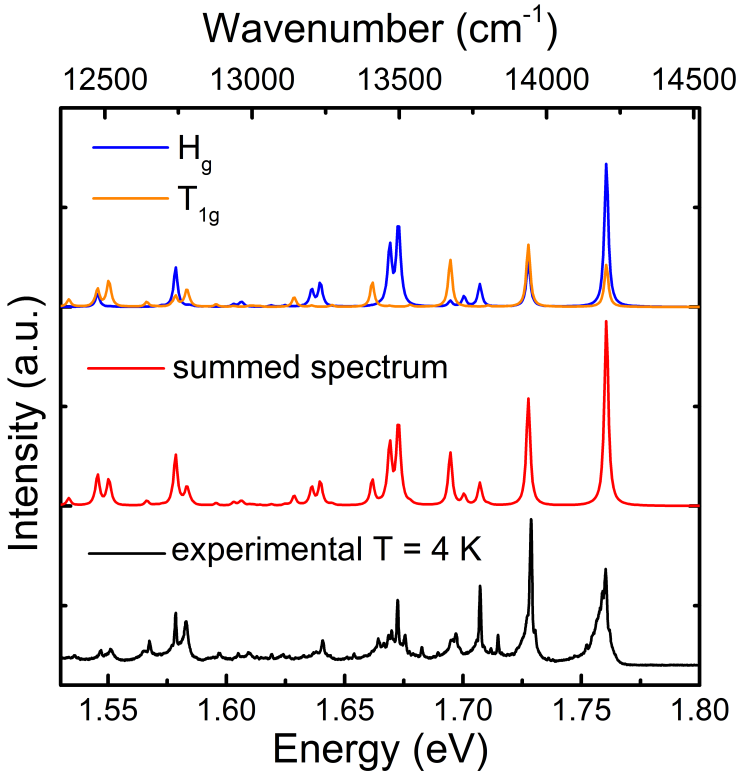

Figure 6.7: Herzberg-Teller, Franck-Condon and Jahn-Teller computed transition lines for the H_g (blue) and T_{1g} (yellow) states. The summed spectrum (red) results from a linear combination of 0.5 H_g and 0.5 T_{1g} and is compared with the experimental data (black). We thank M. Wykes for providing the simulated spectra. Reprinted with permission from [185]. Copyright 2015 American Chemical Society.

difference in the mixing of states compared to C_{60} is not surprisingly, as discussed above, and it has been shown to be highly dependent on the environment.

Finally, the simulated spectrum is computed invoking the mixing of the T_{1g} and H_g states, with a relative weight of 1:1 respectively, disregarding any contributions from the T_{2g} state. The resulting spectrum is shown in Fig. 6.7 and reproduces quite well the experimental PCBM single crystal spectrum also plotted in Fig. 6.7.

6.7 Conclusions

We report the PL spectrum of PCBM single-crystals at 4 K that shows several and well-resolved transition lines. Thanks to the fact that solvent-free crystals became recently available, we were able to investigate the PL emission in greater detail than what have been reported so far. Indeed, as we have discussed, with the amorphous and polycrystalline PCBM we would not have been allowed to get such an insight into its photophysical properties.

Upon functionalization of the C_{60} cage, PCBM lost the overall molecular symmetry however the electronic density is still mostly located on the C_{60} moiety. Therefore, interestingly but perhaps not surprisingly, we found that the PL spectrum of PCBM is similar to that of C_{60} for which optical transitions are affected by selection rules dictated by symmetry. This parallelism has also been strengthened by quantum-chemical calculations that have successfully adapted the model used for the simulation of the C_{60} emission spectrum to PCBM including HT and JT effects.

7 Conclusions and outlook

This thesis has provided an outlook on aspects of general interest in the organic optoelectronic field. By means of photophysical investigations, we described and characterized various organic semiconductors addressing some of the challenges currently open in this field.

In light of the interest in NIR emission, we proposed two ways for obtaining emission at long wavelength. Firstly, a new design of promising materials for optoelectronics involving the substitution of sulphur with selenium. Secondly, the engineering of low band gaps through a methodical choice of the relative positions of the frontier levels of two organic semiconductors. We also considered the use of phosphorescent emitters owing to their potential for high efficiency OLEDs.

Finally, we dedicated our attention to a detailed investigation of the photoluminescence emission of PCBM, owing to the recently reported growth of single-crystals without solvent inclusions, in the attempt to provide precious information on the ordering and relative importance of the relevant excited states.

7.1 Achieving near-infrared emission

In chapter 3 we have presented the first example of incorporation of a class of benzotriazoloselenadiazole-based NIR emitting chromophores. One important issue arising from the comparison between thiadiazole and selenadiazole was whether the substitution of sulphur with selenium can be considered a competing strategy to push emission further in the NIR. Indeed we showed that selenium substitution is more effective, as it preserves both PL and EL efficiencies to a higher value than by exploiting higher sulphur

chromophore loadings, while achieving a more important red-shift. In addition, comparison with previously published branched-side-chain copolymers suggested materials design criteria by showing that charge trapping on the low gap DAD segments is the dominant source of resistance in these devices.

In chapter 4, we suggested that HATNA/polyfluorene heterojunctions have a strong tendency to form exciplex as reported for polyfluorene-based heterojunctions. Also, exciplexes can be regarded as an alternative route to systematically and finely tune the emission wavelength. This strategy can be readily implemented in LEDs and, in particular, we demonstrated that pure NIR EL can be easily obtained with no emission from the single components at any operational voltage.

We are conscious that power efficiencies for OLEDs are currently low for emitters in the NIR and seem to decrease when increasing the emission wavelength. This issues the challenge whether such efficiency drop-off is an intrinsic phenomenon or could be overcome with a better material and device design.

7.2 Phosphorescent co-polymers

The incorporation of a phosphorescent emitter, a platinum(II) complexed porphyrin, directly into the backbone of a polyfluorene polymer overcomes the porphyrin aggregation and phase separation as presented in chapter 5. The polyfluorene moiety also actively concurs to the emission through energy transfer to the porphyrin which we suggested it is enhanced compared to the analogous blend of porphyrin and polyfluorene. Indeed, we showed that the co-polymers emit predominantly in the red/NIR region arising from the porphyrin moiety for porphyrin loading as low as 2%.

In contrast with previous studies where the Pt(II)-porphyrin was incorporated into the polyfluorene in the β-pyrrolic position, we explored the impact of a meso incorporation. Even though a direct comparison with previously reported copolymers is not straightforward (because of a more complex LED architecture), we observed that the incorporation in the meso position does not lead to major improvements both on the optical properties and the device side.

7.3 Fluorescence of PCBM single-crystals

We ended by reporting the photoluminescence emission of PCBM in chapter 6. Despite the overall symmetry of PCBM is low, the optical transitions are strongly affected by the highly symmetric C_{60} core. Therefore, selection rules apply to PCBM transitions leading to symmetry-forbidden S_1-S_0 transitions. We were able to account for such a structured emission by means of quantum-chemical calculations and a model incorporating both Herzberg-Teller induced emission and Frank-Condon and Jahn-Teller effects.

The PL spectra of PCBM single-crystals become very structured as the temperature is lowered, with extremely well-resolved emission lines (minimum linewidth $\sim$1.3 meV at 4 K). Interestingly we observed that the linewidth shows a strong temperature dependence, consistent with a mostly homogeneous mechanism.

The PL spectrum is very well reproducible and, given that the state mixing is highly dependent on the environment, we were able to identify the presence of traps (i.e. crystal defects) that red shift the PL of bulk PCBM of $\sim$35 meV. The homogeneous distribution over the crystal surface and mono-exponential decay of the lifetime values suggested the high-quality of the crystals.

We claimed that solvent-free crystals are a unique tool to get an insight into PCBM optical properties without the solvent dependence. It would be nevertheless interesting to investigate how the presence of solvent affects such properties given that it has a major impact on the crystal structure.

Bibliography

[1] W. Hu, F. Bai, X. Gong, X.i Zhan, H. Fu, and T. Bjornholm. *Organic optoelectronics*. John Wiley & Sons, 2012.

[2] C. Brabec, U. Scherf, and V. Dyakonov. *Organic photovoltaics: materials, device physics, and manufacturing technologies*. John Wiley & Sons, 2014.

[3] Visit for instance www.oled info.com.

[4] K. Müllen and U. Scherf. *Organic light emitting devices*. Wiley Online Library, 2006.

[5] G. Lanzani. *The photophysics behind photovoltaics and photonics*. John Wiley & Sons, 2012.

[6] C. K. Chiang, C. R. Fincher, Y. W. Park, A. J. Heeger, H. Shirakawa, E. J. Louis, S. C. Gau, and A. G. MacDiarmid. Electrical conductivity in doped polyacetylene. *Physical Review Letters*, 39(17):1098–1101, 1977.

[7] M. Pope, H. P. Kallmann, and P. Magnante. Electroluminescence in organic crystals. *The Journal of Chemical Physics*, 38(8):2042–2043, 1963.

[8] J. H. Burroughes, D. D. C. Bradley, A. R. Brown, R. N. Marks, K. Mackay, R. H. Friend, P. L. Burns, and A. B. Holmes. Light-emitting diodes based on conjugated polymers. *Nature*, 347(6293):539–541, 1990.

[9] C. W. Tang and S. A. VanSlyke. Organic electroluminescent diodes. *Applied Physics Letters*, 51(12):913–915, 1987.

[10] M. T. Bernius, M. Inbasekaran, and W. Wu. Progress with light-emitting polymers. *Advanced Materials*, 12(23):1737–1750, 2000.

[11] C. W Tang. Two-layer organic photovoltaic cell. *Applied Physics Letters*, 48:183, 1986.

[12] C. J. Brabec, N. S. Sariciftci, and J. C. Hummelen. Plastic solar cells. *Advanced Functional Materials*, 11(1):15–26, 2001.

[13] S. Günes, H. Neugebauer, and N. S. Sariciftci. Conjugated polymer-based organic solar cells. *Chemical Reviews*, 107(4):1324–1338, 2007.

[14] G. Li, R. Zhu, and Y. Yang. Polymer solar cells. *Nature Photonics*, 6(3):153–161, 2012.

[15] H. Koezuka, A. Tsumura, and T. Ando. Field-effect transistor with polythiophene thin film. *Synthetic Metals*, 18(1):699–704, 1987.

[16] G. Horowitz. Organic field-effect transistors. *Advanced Materials*, 10(5):365–377, 1998.

[17] M. Muccini. A bright future for organic field-effect transistors. *Nature Materials*, 5(8):605–613, 2006.

[18] T. Sekitani and T. Someya. Stretchable, large-area organic electronics. *Advanced Materials*, 22(20):2228–46, 2010.

[19] R. R. Søndergaard, M. Hösel, and F. Krebs. Roll-to-roll fabrication of large area functional organic materials. *Journal of Polymer Science Part B: Polymer Physics*, 51(1):16–34, 2013.

[20] www.solaronix.com.

[21] V. Coropceanu, J. Cornil, D. A. da Silva Filho, Y. Olivier, R. Silbey, and J. L. Brédas. Charge transport in organic semiconductors. *Chemical Reviews*, 107(4):926–952, 2007.

[22] J. Brédas, D. Beljonne, V. Coropceanu, and J. Cornil. Charge-transfer and energy-transfer processes in π-conjugated oligomers and polymers: a molecular picture. *Chemical Reviews*, 104(11):4971–5004, 2004.

[23] J. Cornil, D. Beljonne, J. P. Calbert, and J. L. Brédas. Interchain interactions in organic π-conjugated materials: impact on electronic structure, optical response, and charge transport. *Advanced Materials*, 13(14):1053–1067, 2001.

[24] B. J. Schwartz. Conjugated polymers as molecular materials: How chain conformation and film morphology influence energy transfer and interchain interactions. *Annual Review of Physical Chemistry*, 54(1):141–172, 2003.

[25] R. H. Friend, R. W. Gymer, A. B. Holmes, J. H. Burroughes, R. N. Marks, C. Taliani, D. D. C. Bradley, D. A. Dos Santos, J. L. Brdas, M. Logdlund, and W. R. Salaneck. Electroluminescence in conjugated polymers. *Nature*, 397(6715):121–128, 1999.

[26] G. Grem, G. Leditzky, B. Ullrich, and G. Leising. Realization of a blue-light-emitting device using poly (p-phenylene). *Advanced Materials*, 4(1):36–37, 1992.

[27] A. Kraft, A. Grimsdale, and A. Holmes. Electroluminescent conjugated polymers seeing polymers in a new light. *Angewandte Chemie International Edition*, 37:402–428, 1998.

[28] U. Scherf and E. List. Semiconducting polyfluorenestowards reliable structure–property relationships. *Advanced Materials*, 14(7):477–487, 2002.

[29] J. Morin, M. Leclerc, D. Ades, and A. Siove. Polycarbazoles: 25 years of progress. *Macromolecular Rapid Communications*, 26(10):761–778, 2005.

[30] H. Bronstein, Z. Chen, R. Ashraf, W. Zhang, J. Du, J. Durrant, P. Shakya Tuladhar, K. Song, S. Watkins, and Y. Geerts. Thieno [3, 2-b] thiophene-diketopyrrolopyrrole-containing polymers for high-performance organic field-effect

transistors and organic photovoltaic devices. *Journal of the American Chemical Society*, 133(10):3272–3275, 2011.

[31] T. Parker, D. Patel, K. Moudgil, S. Barlow, C. Risko, J. Brdas, J. R. Reynolds, and S. R. Marder. Heteroannulated acceptors based on benzothiadiazole. *Materials Horizons*, 2(1):22–36, 2015.

[32] S. Lamansky, P. Djurovich, D. Murphy, F. Abdel-Razzaq, H. Lee, C. Adachi, P. Burrows, S. Forrest, and M. Thompson. Highly phosphorescent bis-cyclometalated iridium complexes: synthesis, photophysical characterization, and use in organic light emitting diodes. *Journal of the American Chemical Society*, 123(18):4304–4312, 2001.

[33] M. A. Baldo, D. F. O'brien, Y. You, A. Shoustikov, S. Sibley, M. E. Thompson, and S. R. Forrest. Highly efficient phosphorescent emission from organic electroluminescent devices. *Nature*, 395(6698):151–154, 1998.

[34] H. Hoppe and N. Sariciftci. Morphology of polymer/fullerene bulk heterojunction solar cells. *Journal of Materials Chemistry*, 16(1):45–61, 2006.

[35] S. Schols. *Device architecture and materials for organic light-emitting devices*. Springer, 2011.

[36] W. Barford. *Electronic and optical properties of conjugated polymers*. Oxford University Press, 2005.

[37] W. Salaneck, R. Friend, and J. Brédas. Electronic structure of conjugated polymers: Consequences of electron–lattice coupling. *Physics Reports*, 319(6):231–251, 1999.

[38] R. H. Friend, D. D. C. Bradley, and P. D. Townsend. Photo-excitation in conjugated polymers. *Journal of Physics D: Applied Physics*, 20(11):1367, 1987.

[39] A. Troisi. Charge transport in high mobility molecular semiconductors: classical models and new theories. *Chemical Society Reviews*, 40(5):2347–2358, 2011.

[40] Z. Shuai, H. Geng, W. Xu, Y. Liao, and J. André. From charge transport parameters to charge mobility in organic semiconductors through multiscale simulation. *Chemical Society Reviews*, 43(8):2662–2679, 2014.

[41] P. Blom and M. Vissenberg. Charge transport in poly (p-phenylene vinylene) light-emitting diodes. *Materials Science and Engineering: R: Reports*, 27(3):53–94, 2000.

[42] A. C. Morteani, A. S. Dhoot, J. S. Kim, C. Silva, N. C. Greenham, C. Murphy, E. Moons, S. Cin, J. H. Burroughes, and R. H. Friend. Barrier-free electron-hole capture in polymer blend heterojunction light-emitting diodes. *Advanced Materials*, 15(20):1708–+, 2003.

[43] J. L. Brédas, J. Cornil, and A. J. Heeger. The exciton binding energy in luminescent conjugated polymers. *Advanced Materials*, 8(5):447–452, 1996.

[44] S. F. Alvarado, P. F. Seidler, D. G. Lidzey, and D. D. C. Bradley. Direct determination of the exciton binding energy of conjugated polymers using a scanning tunneling microscope. *Physical Review Letters*, 81(5):1082, 1998.

[45] M.A. Baldo, D.F. Obrien, M.E. Thompson, and S.R. Forrest. Excitonic singlet-triplet ratio in a semiconducting organic thin film. *Physical Review B*, 60(20):14422, 1999.

[46] C. Deibel, T. Strobel, and V. Dyakonov. Role of the charge transfer state in organic donor–acceptor solar cells. *Advanced Materials*, 22(37):4097–4111, 2010.

[47] C. Piliego and M. A. Loi. Charge transfer state in highly efficient polymerfullerene bulk heterojunction solar cells. *Journal of Materials Chemistry*, 22(10):4141–4150, 2012.

[48] J. R. Lakowicz. *Principles of fluorescence spectroscopy*. Springer, 2009.

[49] N.J. Turro, V. Ramamurthy, and J. C. Scaiano. *Principles of molecular photochemistry: an introduction*, book section Radiative Transitions between Electronic States, pages 169–264. University science books, 2009.

[50] U. Rauscher, L. Schutz, A. Greiner, and H. Bassler. Site-selective spectroscopy of matrix-isolated conjugated polymers. *Journal of Physics: Condensed Matter*, 1(48):9751, 1989.

[51] F. Grozema, L. Siebbeles, G. Gelinck, and J. Warman. The opto-electronic properties of isolated phenylenevinylene molecular wires. In *Molecular Wires and Electronics*, pages 135–164. Springer, 2005.

[52] M. Pope and C. E. Swenberg. Electronic processes in organic crystals and polymers, 1999. *Applied Physics Letters*, 80:2401, 2002.

[53] V. Barone, J. Bloino, and M. Biczysko. Vibrationally-resolved electronic spectra in Gaussian 09. 2009.

[54] F. Negri, G. Orlandi, and F. Zerbetto. Interpretation of the vibrational structure of the emission and absorption spectra of C60. *The Journal of Chemical Physics*, 97(9):6496–6503, 1992.

[55] J. Sprafke, D. Kondratuk, M. Wykes, A. Thompson, M. Hoffmann, R. Drevinskas, W. Chen, C. Keong Yong, J. Karnbratt, and J. Bullock. Belt-shaped π-systems: relating geometry to electronic structure in a six-porphyrin nanoring. *Journal of the American Chemical Society*, 133(43):17262–17273, 2011.

[56] B. Minaev, G. Baryshnikov, and H. Agren. Principles of phosphorescent organic light emitting devices. *Physical Chemistry Chemical Physics*, 16(5):1719–58, 2014.

[57] E. Collini and G. Scholes. Coherent intrachain energy migration in a conjugated polymer at room temperature. *Science*, 323(5912):369–373, 2009.

[58] G. Scholes and G. Rumbles. Excitons in nanoscale systems. *Nature Materials*, 5(9):683–696, 2006.

[59] M. Gordon. *The exciplex*. Academic Press, 1975.

[60] J. S. Kim, M. Granstrom, R. H. Friend, N. Johansson, W. R. Salaneck, R. Daik, W. J. Feast, and F. Cacialli. Indium-tin oxide treatments for single- and double-layer polymeric light-emitting diodes: The relation between the anode physical, chemical, and morphological properties and the device performance. *Journal of Applied Physics*, 84(12):6859–6870, 1998.

[61] T. M. Brown, J. S. Kim, R. H. Friend, F. Cacialli, R. Daik, and W. J. Feast. Built-in field electroabsorption spectroscopy of polymer light-emitting diodes incorporating a doped poly(3,4-ethylene dioxythiophene) hole injection layer. *Applied Physics Letters*, 75(12):1679–1681, 1999.

[62] T. M. Brown and F. Cacialli. Contact optimization in polymer light-emitting diodes. *Journal Polymer Science Polymer Physics*, 41(21):2649–2664, 2003.

[63] F. Cacialli. Organic semiconductors for the new millennium. *Philosophical Transactions of the Royal Society of London. Series A: Mathematical, Physical and Engineering Sciences*, 358(1765):173–192, 2000.

[64] P. S. Davids, I. H. Campbell, and D. L. Smith. Device model for single carrier organic diodes. *Journal of Applied Physics*, 82(12):6319–6325, 1997.

[65] G. A. H. Wetzelaer, M. Kuik, H. T. Nicolai, and P. W. M. Blom. Trap-assisted and langevin-type recombination in organic light-emitting diodes. *Physical Review B*, 83(16):165204, 2011.

[66] Lakowicz. J. R. *Principles of fluorescence spectroscopy*, book section Time-domain lifetime measurements, pages 97–155. Springer, New York, 2006.

[67] M. Wahl. *Time-Correlated Single Photon Counting*. Number Technical Note. PicoQuant GmbH, 2009.

[68] *FLS920 Series*. Number Technical Note. Edinburgh Instruments Ltd, 2011.

[69] J. C. de Mello, H. F. Wittmann, and R. H. Friend. An improved experimental determination of external photoluminescence quantum efficiency. *Advanced Materials*, 9(3):230–232, 1997. 10.1002/adma.19970090308.

[70] T. Brown, G. Lazzerini, L. Parrott, V. Bodrozic, L. Bürgi, and F. Cacialli. Time dependence and freezing-in of the electrode oxygen plasma-induced work function enhancement in polymer semiconductor heterostructures. *Organic Electronics*, 12(4):623–633, 2011.

[71] P. Varo, J. Tejada, J. Villanueva, and MJ Deen. Space-charge and injection limited current in organic diodes: A unified model. *Organic Electronics*, 15(10):2526–2535, 2014.

[72] G. Tregnago, T. T. Steckler, O. Fenwick, M. Andersson, and F. Cacialli. Thia- and selena-diazole containing polymers for near-infrared light-emitting diodes. *Journal of Material Chemistry C*, 3:2792–2797, 2015 - http://dx.doi.org/10.1039/C5TC00118H.

[73] T. Karu. *Low Power Laser Therapy*, book section Chapter 48. CRC Press, 2003.

[74] H. Suzuki. Organic light-emitting materials and devices for optical communication technology. *Journal of Photochemical Photobiology A*, 166(1-3):155–161, 2004.

[75] M. S. White, M. Kaltenbrunner, E. D. Glowacki, K. Gutnichenko, G. Kettlgruber, I. Graz, S. Aazou, C. Ulbricht, D. A. M. Egbe, M. C. Miron, Z. Major, M. C. Scharber, T. Sekitani, T. Someya, S. Bauer, and N. S. Sariciftci. Ultrathin, highly flexible and stretchable PLEDs. *Nature Photonics*, 7(10):811–816, 2013.

[76] X. Du, J. Qi, Z. Zhang, D. Ma, and Z. Y. Wang. Efficient non-doped near infrared organic light-emitting devices based on fluorophores with aggregation-induced emission enhancement. *Chemical Materials*, 24(11), 2012.

[77] Y. X. Yang, R. T. Farley, T. T. Steckler, S. H. Eom, J. R. Reynolds, K. S. Schanze,

and J. G. Xue. Efficient near-infrared organic light-emitting devices based on low-gap fluorescent oligomers. *Journal of Applied Physics*, 106(4):044509, 2009.

[78] Y. Sun, C. Borek, K. Hanson, P. I. Djurovich, M. E. Thompson, J. Brooks, J. J. Brown, and S. R. Forrest. Photophysics of Pt-porphyrin electrophosphorescent devices emitting in the near infrared. *Applied Physics Letters*, 90(21):213503, 2007.

[79] T. V. Duncan, K. Susumu, L. E. Sinks, and M. J. Therien. Exceptional near-infrared fluorescence quantum yields and excited-state absorptivity of highly conjugated porphyrin arrays. *Journal of American Chemical Society*, 128(28):9000–1.

[80] E. L. Williams, J. Li, and G. E. Jabbour. Organic light-emitting diodes having exclusive near-infrared electrophosphorescence. *Applied Physics Letters*, 89(8), 2006.

[81] G. Tzamalis, V. Lemaur, F. Karlsson, P. O. Holtz, M. Andersson, X. Crispin, J. Cornil, and M. Berggren. Fluorescence light emission at 1 eV from a conjugated polymer. *Chemical Physics Letters*, 489(1-3):92–95, 2010. 10.1016/j.cplett.2010.02.049.

[82] E. Perzon, F. Zhang, M. Andersson, W. Mammo, O. Ingans, and M. R Andersson. A conjugated polymer for near infrared optoelectronic applications. *Advanced Materials*, 19(20):3308–3311, 2007. 10.1002/adma.200700557.

[83] Z. K. Tan, R. S. Moghaddam, M. L. Lai, P. Docampo, R. Higler, F. Deschler, M. Price, A. Sadhanala, L. M. Pazos, D. Credgington, F. Hanusch, T. Bein, H. J. Snaith, and R. H. Friend. Bright light-emitting diodes based on organometal halide perovskite. *Nature Nanotechnology*, 9(9):687–92, 2014.

[84] P. Li, O. Fenwick, S. Yilmaz, D. Breusov, D. J. Caruana, S. Allard, U. Scherf, and F. Cacialli. Dual functions of a novel low-gap polymer for near infra-red photovoltaics and light-emitting diodes. *Chemical Communications*, 47(31):8820–8822, 2011.

[85] C. Borek, K. Hanson, P. I. Djurovich, M. E. Thompson, K. Aznavour, R. Bau, Y. Sun, S. R. Forrest, J. Brooks, L. Michalski, and J. Brown. Highly efficient, near-infrared electrophosphorescence from a Pt-metalloporphyrin complex. *Angewandte Chemie International Edition*, 46(7):1109–12, 2007.

[86] R. J. Curry and W. P. Gillin. 1.54 μm electroluminescence from erbium (III) tris(8-hydroxyquinoline) (ErQ)-based organic light-emitting diodes. *Applied Physics Letters*, 75(10):1380–1382, 1999.

[87] O. Fenwick, J. K. Sprafke, J. Binas, D. V. Kondratuk, F. Di Stasio, H. L. Anderson, and F. Cacialli. Linear and cyclic porphyrin hexamers as near-infrared emitters in organic light-emitting diodes. *Nano Letters*, 11(6):2451–2456, 2011.

[88] G Tregnago, C Fléchon, S Choudhary, C Gozalvez, A Mateo-Alonso, and F Cacialli. Virtually pure near-infrared electroluminescence from exciplexes at polyfluorene/hexaazatrinaphthylene interfaces. *Applied Physics Letters*, 105(14):143304, 2014.

[89] B. C. Thompson, L. G. Madrigal, M. R. Pinto, T-S. Kang, K. S. Schanze, and J. R. Reynolds. Donor-acceptor copolymers for red- and near-infrared-emitting polymer light-emitting diodes. *Journal of Polymer Science Part A Polymer Chemistry*, 43(7):1417–1431, 2005. 10.1002/pola.20578.

[90] T. T. Steckler, O. Fenwick, T. Lockwood, M. R. Andersson, and F. Cacialli. Near-infrared polymer light-emitting diodes based on low-energy gap oligomers copolymerized into a high-gap polymer host. *Macromolecule Rapid Communications*, 34(12):990–6, 2013.

[91] T. L. Tam, H. Li, Y. M. Lam, S. G. Mhaisalkar, and A. C. Grimsdale. Synthesis and characterization of [1,2,5]chalcogenazolo[3,4-f]benzo[1,2,3]triazole and [1,2,3]triazolo[3,4-g]quinoxaline derivatives. *Organic Letters*, 13(17):4612–5, 2011.

[92] D. G. Patel, F. Feng, Y. Y. Ohnishi, K. A. Abboud, S. Hirata, K. S. Schanze, and J. R. Reynolds. It takes more than an imine: the role of the central atom

on the electron-accepting ability of benzotriazole and benzothiadiazole oligomers. *Journal of American Chemical Society*, 134(5):2599–612, 2012.

[93] T. T. Steckler, M. J. Lee, Z. Chen, O. Fenwick, M. R. Andersson, F. Cacialli, and H. Sirringhaus. Multifunctional materials for OFETs, LEFETs and NIR PLEDs. *Journal of Materials Chemistry C*, 2(26):5133–5141, 2014.

[94] M. X. Chen, E. Perzon, M. R. Andersson, S. Marcinkevicius, S. K. M. Jonsson, M. Fahlman, and M. Berggren. 1 micron wavelength photo- and electroluminescence from a conjugated polymer. *Applied Physics Letters*, 84(18):3570–3572, 2004.

[95] Q. Zhang, Y. Divayana, J. Xiao, Z. Y. Wang, E. R. T. Tiekink, H. M. Doung, H. Zhang, F. Boey, X. W. Sun, and F. Wudl. Synthesis, characterization, and bipolar transporting behavior of a new twisted polycyclic aromatic hydrocarbon: 1',4'-diphenyl-naphtho-(2'.3':1.2)-pyrene-6'-nitro-7'-methyl carboxylate. *Chemistry - An European Journal*, 16(25):7422–7426, 2010.

[96] R. Q. Yang, R. Y. Tian, Q. Hou, W. Yang, and Y. Cao. Synthesis and optical and electroluminescent properties of novel conjugated copolymers derived from fluorene and benzoselenadiazole. *Macromolecules*, 36(20):7453–7460, 2003.

[97] I. H. Jung, H. Kim, M. J. Park, B. Kim, J. H. Park, E. Jeong, H. Y. Woo, S. Yoo, and H. K. Shim. Synthesis and characterization of cyclopentadithiophene-based low bandgap copolymers containing electron-deficient benzoselenadiazole derivatives for photovoltaic devices. *Journal of Polymer Science Part A Polymer Chemistry*, 48(6):1423–1432, 2010.

[98] J. H. Hou, T. L. Chen, S. Q. Zhang, H. Y. Chen, and Y. Yang. Poly [4,4-bis(2-ethylhexyl)cyclopenta [2,1-b;3,4-b'] dithiophene-2,6-diyl-alt-2,1,3-benzoselenadiazole-4,7-diyl], a new low band gap polymer in polymer solar cells. *Journal of Physical Chemistry C*, 113(4):1601–1605, 2009.

[99] L. Yang, J. K. Feng, and A. M. Ren. Theoretical study on electronic structure and optical properties of novel donor-acceptor conjugated copolymers derived from benzothiadiazole and benzoselenadiazole. *Journal of Molecular Structure Theochemistry*, 816(1-3):161–170, 2007.

[100] C. M. MacNeill, R. C. Coffin, D. L. Carroll, and N. H. Levi-Polyachenko. Low band gap donor-acceptor conjugated polymer nanoparticles and their NIR-mediated thermal ablation of cancer cells. *Macromolecule Bioscience*, 13(1):28–34, 2013.

[101] G. Qian, Z. Zhong, M. Luo, D. Yu, Z. Zhang, Z. Y. Wang, and D. G. Ma. Simple and efficient NIR organic chromophores for light emitting diodes with single electroluminescent emission above 1000 nm. *Advanced Materials*, 21(1):111–116, 2009.

[102] O. Fenwick, S. Fusco, T. N. Baig, F. Di Stasio, T. T. Steckler, P. Henriksson, C. Flechon, M. R. Andersson, and F. Cacialli. Efficient red electroluminescence from diketopyrrolopyrrole copolymerised with a polyfluorene. *Applied Physics Letters Materials*, 1(3):7, 2013.

[103] X. Gong, J. Ostrowski, D.l Moses, G. Bazan, and A. Heeger. Electrophosphorescence from a polymer guest–host system with an iridium complex as guest: Förster energy transfer and charge trapping. *Advanced Functional Materials*, 13(6):439–444, 2003.

[104] V. Cleave, G. Yahioglu, P. Le Barny, D. Hwang, A. Holmes, R. Friend, and N. Tessler. Transfer processes in semiconducting polymer–porphyrin blends. *Advanced Materials*, 13(1):44–47, 2001.

[105] X. Jiang, R. Register, K. Killeen, M. Thompson, F. Pschenitzka, and J. Sturm. Statistical copolymers with side-chain hole and electron transport groups for single-layer electroluminescent device applications. *Chemistry of Materials*, 12(9):2542–2549, 2000.

[106] Please note that the decays reported in Fig. 2b have not been deconvolved to remove the instrumental response.

[107] S. Gelinas, O. Pare-Labrosse, C. N. Brosseau, S. Albert-Seifried, C. R. McNeill, K. R. Kirov, I. A. Howard, R. Leonelli, R. H. Friend, and C. Silva. The binding energy of charge-transfer excitons localized at polymeric semiconductor heterojunctions. *Journal of Physical Chemistry C*, 115(14):7114–7119, 2011.

[108] R. H. Friend, M. Phillips, A. Rao, M. W. B. Wilson, Z. Li, and C. R. McNeill. Excitons and charges at organic semiconductor heterojunctions. *Faraday Discussions*, 155:339–348, 2012.

[109] J. Kalinowski, M. Cocchi, D. Virgili, V. Fattori, and J. A. G. Williams. Mixing of excimer and exciplex emission: A new way to improve white light emitting organic electrophosphorescent diodes. *Advanced Materials*, 19(22):4000–4005, 2007.

[110] W. Hung, G. Fang, S. Lin, S. Cheng, K. Wong, T. Kuo, and P. Chou. The first tandem, all-exciplex-based WOLED. *Scientific Reports*, 4, 2014.

[111] K. Tvingstedt, K. Vandewal, A. Gadisa, F. J. Zhang, J. Manca, and O. Inganas. Electroluminescence from charge transfer states in polymer solar cells. *Journal of American Chemical Society*, 131(33):11819–11824, 2009.

[112] Y. S. Huang, S. Westenhoff, I. Avilov, P. Sreearunothai, J.M. Hodgkiss, C. Deleener, R. H. Friend, and D. Beljonne. Electronic structures of interfacial states formed at polymeric semiconductor heterojunctions. *Nature Materials*, 7(6):483–489, 2008.

[113] J. Clark, R. Archer, T. Redding, C. Foden, J. Tant, Y. Geerts, R. H. Friend, and C. Silva. Charge recombination in distributed heterostructures of semiconductor discotic and polymeric materials. *Journal of Applied Physics*, 103(12), 2008.

[114] M. Lehmann, G. Kestemont, R. Gmez Aspe, C. Buess-Herman, M. H. J. Koch, M. G. Debije, J. Piris, M. P. de Haas, J. M. Warman, and M. D. Watson. High

charge carrier mobility in π deficient discotic mesogens: Design and structureproperty relationship. *Chemistry - An European Journal*, 11(11):3349–3362, 2005.

[115] S. Choudhary, C. Gozalvez, A. Higelin, I. Krossing, M. Melle-Franco, and A. Mateo-Alonso. Hexaazatrinaphthylenes with different twists. *Chemistry-A European Journal*, 20(6):1525–1528, 2014.

[116] Jr. Pascal, R. A. Twisted acenes. *Chemical Reviews*, 106(12):4809–4819, 2006.

[117] M. Gsaenger, J. H. Oh, M. Koenemann, H. W. Hoeffken, A-M. Krause, Z. Bao, and F. Wuerthner. A crystal-engineered hydrogen-bonded octachloroperylene diimide with a twisted core: An n-channel organic semiconductor. *Angewandte Chemie International Edition*, 49(4):740–743, 2010.

[118] J. Xiao, H. M. Duong, Y. Liu, W. Shi, L. Ji, G. Li, S. Li, X-W. Liu, J. Ma, F. Wudl, and Q. Zhang. Synthesis and structure characterization of a stable nonatwistacene. *Angewandte Chemie International Edition*, 51(25):6094–6098, 2012.

[119] S. More, S. Choudhary, A. Higelin, I. Krossing, M. Melle-Franco, and A. Mateo-Alonso. Twisted pyrene-fused azaacenes. *Chemical Communications*, 50(16):1976–1979, 2014.

[120] A. Mateo-Alonso. Pyrene-fused pyrazaacenes: from small molecules to nanoribbons. *Chemical Society Reviews*, 2014.

[121] A. Pradhan, P. Dechambenoit, H. Bock, and F. Durola. Highly twisted arenes by scholl cyclizations with unexpected regioselectivity. *Angewandte Chemie International Edition*, 50(52):12582–12585, 2011.

[122] Q. F. Xu, H. M. Duong, F. Wudl, and Y. Yang. Efficient single-layer "twistacene"-doped polymer white light-emitting diodes. *Applied Physics Letters*, 85(16):3357–3359, 2004.

[123] J. Xiao, Y. Divayana, Q. Zhang, H. M. Doung, H. Zhang, F. Boey, X. W. Sun, and F. Wudl. Synthesis, structure, and optoelectronic properties of a new

twistacene 1,2,3,4,6,13-hexaphenyl-7: 8,11: 12-bisbenzo-pentacene. *Journal of Materials Chemistry*, 20(37):8167–8170, 2010.

[124] Z. Liu, J. Xiao, Q. Fu, H. Feng, X. Zhang, T. Ren, S. Wang, D. G. Ma, X. Wang, and H. Chen. Synthesis and physical properties of the conjugated dendrons bearing twisted acenes used in solution processing of organic light-emitting diodes. *ACS Applied Materials Interfaces*, 5(21):11136–11141, 2013.

[125] G. Qian and Z. Y. Wang. Near-infrared organic compounds and emerging applications. *Chemistry - An Asian Journal*, 5(5):1006–1029, 2010.

[126] A. Gadisa, E. Perzon, M. R. Andersson, and O. Ingans. Red and near infrared polarized light emissions from polyfluorene copolymer based light emitting diodes. *Applied Physics Letters*, 90(11):113510, 2007.

[127] R. Yang, R. Tian, J. Yan, Y. Zhang, J. Yang, Q. Hou, W. Yang, C. Zhang, and Y. Cao. Deep-red electroluminescent polymers: synthesis and characterization of new low-band-gap conjugated copolymers for light-emitting diodes and photovoltaic devices. *Macromolecules*, 38(2):244–253, 2005.

[128] J. S. Kim, R. H. Friend, and F. Cacialli. Improved operational stability of polyfluorene-based organic light-emitting diodes with plasma-treated indium-tin-oxide anodes. *Applied Physics Letters*, 74(21):3084–3086, 1999.

[129] J. J. Michels, M. J. O'Connell, P. N. Taylor, J. S. Wilson, F. Cacialli, and H. L. Anderson. Synthesis of conjugated polyrotaxanes. *Chemistry - A European Journal*, 9(24):6167–6176, 2003.

[130] S. Brovelli, F. Meinardi, G. Winroth, O. Fenwick, G. Sforazzini, M. J. Frampton, L. Zalewski, J. A. Levitt, F. Marinello, P. Schiavuta, K. Suhling, H. L. Anderson, and F. Cacialli. White electroluminescence by supramolecular control of energy transfer in blends of organic-soluble encapsulated polyfluorenes. *Advanced Functional Materials*, 20(2):272–280, 2010.

[131] G. Latini, G. Winroth, S. Brovelli, S. O. McDonnell, H. L. Anderson, J. M. Mativetsky, P. Samor, and F. Cacialli. Enhanced luminescence properties of highly threaded conjugated polyelectrolytes with potassium counter-ions upon blending with poly (ethylene oxide). *Journal of Applied Physics*, 107(12):124509, 2010.

[132] W. J. Feast, F. Cacialli, A. T. H. Koch, R. Daik, C. Lartigau, R. H. Friend, D. Beljonne, and J. L. Bredas. Control of luminescence in conjugated polymers through control of chain microstructure. *Journal of Materials Chemistry*, 17(9):907–912, 2007.

[133] We can estimate the stabilization energy by subtracting the exciplex emission energy to the energy gap between the lowest unoccupied molecular orbital (LUMO) of the acceptor, e.g. in relation to binding energies of 0.07 eV previously estimated for the polyfluorenes the highest occupied molecular orbital (HOMO) of the donor, to yield B=0.230.16 eV. This value is comparatively high, and which complicate comparison with those results) HATNA*-TFB heterojunctions mentioned above, even though we notice the relatively large error bars (not reported in the cited previous works.

[134] F. Cacialli, B. S. Chuah, J. S. Kim, D. A. dos Santos, R. H. Friend, S. C. Moratti, A. B. Holmes, and J. L. Bredas. A green emitting, alkoxy disubstituted poly(p-phenylene vinylene) for electroluminescent devices. *Synthetic Metals*, 102(1-3):924–925, 1999.

[135] R.E. Martin, F. Geneste, R. Riehn, B.S. Chuah, F. Cacialli, R.H. Friend, and A.B. Holmes. Efficient blue-green light emitting poly(1,4-phenylene vinylene) copolymers. *Chemical Communications*, 4:291–292, 2000.

[136] R.E. Martin, F. Geneste, B.S. Chuah, C. Fischmeister, Y.G. Ma, A.B. Holmes, R. Riehn, F. Cacialli, and R.H. Friend. Versatile synthesis of various conjugated aromatic homo- and copolymers. *Synthetic Metals*, 122(1):1–5, 2001.

[137] J. S. Wilson, N. Chawdhury, M. R. A. Al-Mandhary, M. Younus, M. S. Khan, P. R.

Raithby, A. Kohler, and R. H. Friend. The energy gap law for triplet states in pt-containing conjugated polymers and monomers. *Journal of American Chemical Society*, 123(38):9412–9417, 2001.

[138] M. Sun, X. Jiang, W. Liu, T. Zhu, F. M. Huang, and Y. Cao. Selenophene and fluorene based narrow band gap copolymers with energy gap of 1.41 eV for near infrared polymer light emitting diodes. *Synthetic Metals*, 162(15):1406–1410, 2012.

[139] M. A. Baldo, M. E. Thompson, and S. R. Forrest. High-efficiency fluorescent organic light-emitting devices using a phosphorescent sensitizer. *Nature*, 403(6771):750–753, 2000.

[140] M. Sudhakar, P. I. Djurovich, T. E. Hogen-Esch, and M. E. Thompson. Phosphorescence quenching by conjugated polymers. *Journal of American Chemical Society*, 125(26):7796–7, 2003.

[141] P. A. Lane, L. C. Palilis, D. F. O'Brien, C. Giebeler, A. J. Cadby, D. G. Lidzey, A. J. Campbell, W. Blau, and D. D. C. Bradley. Origin of electrophosphorescence from a doped polymer light emitting diode. *Physical Review B*, 63(23), 2001.

[142] X. Chen, J. L. Liao, Y. Liang, M. O. Ahmed, H. E. Tseng, and S. A. Chen. High-efficiency red-light emission from polyfluorenes grafted with cyclometalated iridium complexes and charge transport moiety. *Journal of American Chemical Society*, 125(3):636–7, 2003.

[143] A. J. Sandee, C. K. Williams, N. R. Evans, J. E. Davies, C. E. Boothby, A. Kohler, R. H. Friend, and A. B. Holmes. Solution-processible conjugated electrophosphorescent polymers. *Journal of American Chemical Society*, 126(22):7041–8, 2004.

[144] R. C. Kwong, S. Sibley, T. Dubovoy, M. Baldo, S. R. Forrest, and M. E. Thompson. Efficient, saturated red organic light emitting devices based on phosphorescent platinum(II) porphyrins. *Chemistry of Materials*, 11(12):3709–3713, 1999.

[145] J. Morgado, F. Cacialli, R. H. Friend, R. Iqbal, G. Yahioglu, L. R. Milgrom, S. C. Moratti, and A. B. Holmes. Tuning the red emission of a soluble poly(p-phenylene vinylene) upon grafting of porphyrin side groups. *Chemical Physics Letters*, 325(5-6):552–558, 2000.

[146] R. Iqbal, S. C. Moratti, A. B. Holmes, G. Yahioglu, L. R. Milgrom, F. Cacialli, J. Morgado, and R. H. Friend. Synthesis of porphyrin-PPV copolymers for application in LEDs. *Journal of Materials Science-Materials in Electronics*, 11(2):97–103, 2000.

[147] J. Morgado, F. Cacialli, R. Iqbal, S. C. Moratti, A. B. Holmes, G. Yahioglu, L. R. Milgrom, and R. H. Friend. Forster energy transfer and control of the luminescence in blends of an orange-emitting poly(p-phenylenevinylene) and a red-emitting tetraphenylporphyrin. *Journal of Materials Chemistry*, 11(2):278–283, 2001.

[148] Q. Hou, Y. Zhang, F. Y. Li, J. B. Peng, and Y. Cao. Red electrophosphorescence of conjugated organoplatinum(II) polymers prepared via direct metalation of poly(fluorene-co-tetraphenylporphyrin) copolymers. *Organometallics*, 24(19):4509–4518, 2005.

[149] H. Xiang, L. Zhou, Y. Feng, J. Cheng, D. Wu, and X. Zhou. Tunable fluorescent/phosphorescent platinum(II) porphyrin-fluorene copolymers for ratiometric dual emissive oxygen sensing. *Inorganic Chemistry*, 51(9):5208–12, 2012.

[150] W. L. Zhuang, Y. Zhang, Q. Hou, L. Wang, and Y. Cao. High-efficiency, electrophosphorescent polymers with porphyrin-platinum complexes in the conjugated backbone: Synthesis and device performance. *Journal of Polymer Science Part a-Polymer Chemistry*, 44(13):4174–4186, 2006.

[151] D. Freeman*, G. Tregnago*, S. Araguas Rodriguez, F. Cacialli, H. Bronstein, and *Co-first authorship.* Deep-red electrophosphorescence from a platinum(II)-

porphyrin complex copolymerized with polyfluorene for efficient energy transfer – PF-MPP(Pt). *Submitted*, 2014.

[152] L. M. Mink, M. L. Neitzel, L. M. Bellomy, R. E. Falvo, R. K. Boggess, B. T. Trainum, and P. Yeaman. Platinum(II) and platinum(IV) porphyrin complexes: Synthesis, characterization, and electrochemistry. *Polyhedron*, 16(16):2809–2817, 1997.

[153] K. Becker, J. M. Lupton, J. Feldmann, B. S. Nehls, F. Galbrecht, D. Q. Gao, and U. Scherf. On-chain fluorenone defect emission from single polyfluorene molecules in the absence of intermolecular interactions. *Advanced Functional Materials*, 16(3):364–370, 2006.

[154] M. Sims, D. Bradley, M. Ariu, M. Koeberg, A. Asimakis, M. Grell, and D. Lidzey. Understanding the origin of the 535 nm emission band in oxidized poly (9, 9-dioctylfluorene): The essential role of inter-chain/inter-segment interactions. *Advanced Functional Materials*, 14(8):765–781, 2004.

[155] G. Ponterini, N. Serpone, M. A. Bergkamp, and T. L. Netzel. Comparison of radiationless decay processes in osmium and platinum porphyrins. *Journal of the American Chemical Society*, 105(14):4639–4645, 1983.

[156] D. Guldi and N. Martin. *Photovoltaic applications*, volume 4, book section 12, pages 387–435. Springer, 2002.

[157] J. C. Hummelen, B. W. Knight, F. Lepeq, F. Wudl, J. Yao, and C. L. Wilkins. Preparation and characterization of fulleroid and methanofullerene derivatives. *Journal of Organic Chemistry*, 60(3):532–538, 1995.

[158] Z. C. He, C. M. Zhong, S. J. Su, M. Xu, H. B. Wu, and Y. Cao. Enhanced power-conversion efficiency in polymer solar cells using an inverted device structure. *Nature Photonics*, 6(9):591–595, 2012.

[159] M. A. Loi, S. Toffanin, M. Muccini, M. Forster, U. Scherf, and M. Scharber. Charge transfer excitons in bulk heterojunctions of a polyfluorene copolymer and a fullerene derivative. *Advanced Functional Materials*, 17(13):2111–2116, 2007.

[160] S. Cook, H. Ohkita, Y. Kim, J. J. Benson-Smith, D. D. C. Bradley, and J. R. Durrant. A photophysical study of PCBM thin films. *Chemical Physics Letters*, 445(4-6):276–280, 2007.

[161] R. Noriega, J. Rivnay, K. Vandewal, F. Koch, N. Stingelin, P. Smith, M. Toney, and A. Salleo. A general relationship between disorder, aggregation and charge transport in conjugated polymers. *Nature Materials*, 12(11):1038–44, 2013.

[162] K. Vandewal, S. Himmelberger, and A. Salleo. Structural factors that affect the performance of organic bulk heterojunction solar cells. *Macromolecules*, 46(16):6379–6387, 2013.

[163] Y. Kim, J. Nelson, T. Zhang, S. Cook, J. Durrant, H. Kim, J. Park, M. Shin, S. Nam, M. Heeney, I. McCulloch, C. Ha, and D. Bradley. Distorted asymmetric cubic nanostructure of soluble fullerene crystals in efficient polymer:fullerene solar cells. *ACS Nano*, 3(9):2557–2562, 2009. .

[164] S. Gelinas, A. Rao, A. Kumar, S. Smith, A. Chin, J. Clark, T. van der Poll, G. Bazan, and R. Friend. Ultrafast long-range charge separation in organic semiconductor photovoltaic diodes. *Science*, 343(6170):512–516, 2014.

[165] S. Smith and A. Chin. Ultrafast charge separation and nongeminate electron-hole recombination in organic photovoltaics. *Physical Chemistry Chemical Physics*, 2014.

[166] M. T. Rispens, A. Meetsma, R. Rittberger, C. J. Brabec, N. S. Sariciftci, and J. C. Hummelen. Influence of the solvent on the crystal structure of PCBM and the efficiency of MDMO-PPV : PCBM 'plastic' solar cells. *Chemical Communications*, (17):2116–2118, 2003.

[167] R. Dabirian, X. Feng, L. Ortolani, A. Liscio, V. Morandi, K. Muellen, P. Samori, and V. Palermo. Micron-sized 6,6 -phenyl C61 butyric acid methyl ester crystals grown by dip coating in solvent vapour atmosphere: interfaces for organic photovoltaics. *Physical Chemistry Chemical Physics*, 12(17):4473–4480, 2010.

[168] Y. Yang, C. Liu, S. Gao, Y. Li, X. Wang, Y. Wang, T. Minari, Y. Xu, P. Wang, Y. Zhao, K. Tsukagoshi, and Y. Shi. Large 6,6 -phenyl C-61 butyric acid methyl (PCBM) hexagonal crystals grown by solvent-vapor annealing. *Materials Chemistry and Physics*, 145(3):327–333, 2014.

[169] G. Paterno, A. Warren, J. Spencer, G. Evans, V. Sakai, J. Blumberger, and F. Cacialli. Micro-focused x-ray diffraction characterization of high-quality [6, 6]-PhenylC61 butyric acid methyl ester single crystals without solvent impurities. *Journal of Materials Chemistry C*, 2013.

[170] M. Casalegno, S. Zanardi, F. Frigerio, R. Po, C. Carbonera, G. Marra, T. Nicolini, G. Raos, and S. Meille. Solvent-free phenyl-C61-butyric acid methyl ester (PCBM) from clathrates: insights for organic photovoltaics from crystal structures and molecular dynamics. *Chemical Communications*, 49(40):4525–4527, 2013.

[171] A. Clulow, A. Armin, K. Lee, A. Pandey, C. Tao, M. Velusamy, M. James, A. Nelson, P. Burn, I. Gentle, and P. Meredith. Determination of fullerene scattering length density: A critical parameter for understanding the fullerene distribution in bulk heterojunction organic photovoltaic devices. *Langmuir*, 30(5):1410–1415, 2014.

[172] M. Savoie, A. Rao, A. Bakulin, S. Gelinas, B. Movaghar, R. Friend, T. Marks, and M. Ratner. Unequal partnership: Asymmetric roles of polymeric donor and fullerene acceptor in generating free charge. *Journal of the American Chemical Society*, 136(7):2876–2884, 2014.

[173] S.T. Tan, B.J. Chen, X.W. Sun, W.J. Fan, H.S. Kwok, X.H. Zhang, and S.J. Chua.

Blueshift of optical band gap in ZnO thin films grown by metal-organic chemical-vapor deposition. *Journal of Applied Physics*, 98(1):013505–013505, 2005.

[174] A. Dzwilewski, T. Wagberg, and L. Edman. Photo-induced and resist-free imprint patterning of fullerene materials for use in functional electronics. *Journal of the American Chemical Society*, 131(11):4006–4011, 2009.

[175] S. Falke, P. Eravuchira, A. Materny, and C. Lienau. Raman spectroscopic identification of fullerene inclusions in polymer/fullerene blends. *Journal of Raman Spectroscopy*, 42(10):1897–1900, 2011.

[176] W. Guss, J. Feldmann, E. O. Gobel, C. Taliani, H. Mohn, W. Muller, P. Haussler, and H. U. Termeer. Fluorescence from x-traps in C60 single-crystals. *Physical Review Letters*, 72(16):2644–2647, 1994.

[177] D. J. Vandenheuvel, G. J. B. Vandenberg, E. J. J. Groenen, J. Schmidt, I. Holleman, and G. Meijer. Lowest excited singlet-state of C60 - A vibronic analysis of the fluorescence. *Journal of Physical Chemistry*, 99(30):11644–11649, 1995.

[178] A. Sassara, G. Zerza, M. Chergui, F. Negri, and G. Orlandi. The visible emission and absorption spectrum of C-60. *Journal of Chemical Physics*, 107(21):8731–8741, 1997.

[179] G. Orlandi and F. Negri. Electronic states and transitions in C-60 and C-70 fullerenes. *Photochemical Photobiological Sciences*, 1(5):289–308, 2002.

[180] J. L. Brédas. *Conjugated Oligomers, Polymers, and Dendrimers: From Polyacetylene to DNA: Proceedings of the Fourth International Francqui Symposium, 21-23 October 1998, Brussels*, volume 4. De Boeck Supérieur, 1999.

[181] J. Cioslowski. *Electronic structure calculations of fullerenes and their derivatives.* 1995.

[182] W. I. F. David, R. M. Ibberson, J. C. Matthewman, K. Prassides, T. J. S. Dennis,

J. P. Hare, H. W. Kroto, R. Taylor, and D. R. M. Walton. Crystal-structure and bonding of ordered C60. *Nature*, 353(6340):147–149, 1991.

[183] Z. Zhang, P. Han, X. Liu, J. Zhao, H. Jia, F. Zeng, and B. Xu. First principle calculations of the electronic properties of the fullerene derivative as an electron acceptor in organic solar cells. *Journal of Physical Chemistry C*, 112(48):19158–19161, 2008.

[184] H. Wang, Y. He, and H. Li, Y.and Su. Photophysical and electronic properties of five PCBM-like C-60 derivatives: Spectral and quantum chemical view. *Journal of Physical Chemistry A*, 116(1):255–262, 2012.

[185] G. Tregnago, M. Wykes, G. Paternó, D. Beljonne, and F. Cacialli. Low-temperature photoluminescence spectroscopy of solvent-free PCBM single-crystals. *To be submitted.*

[186] D. J. Vandenheuvel, I. Y. Chan, E. J. J. Groenen, M. Matsushita, J. Schmidt, and G. Meijer. On the fluorescence of crystalline C-60 at 1.2 K. *Chemical Physics Letters*, 233(3):284–290, 1995.